Chapter 2: Plasma confinement and transport

Chapter 2: Plasma confinement and transport

ITER Physics Expert Groups on Confinement and
Transport and Confinement Modelling and Database*

ITER Physics Basis Editors[†]

ITER EDA, Naka Joint Work Site, Mukouyama,
Naka-machi, Naka-gun, Ibaraki-ken, Japan

Abstract. Physics knowledge in plasma confinement and transport relevant to design of a reactor-scale tokamak is reviewed and methodologies for projecting confinement properties to ITER are provided. Theoretical approaches to describing a turbulent plasma transport in a tokamak are outlined and phenomenology of major energy confinement regimes observed in tokamaks, including those with edge and internal transport barriers, is described. The chapter is focused on the energy confinement in the high confinement regime (H-mode) with the edge localized MHD modes, the basic operational regime of ITER. Three approaches are being pursued: (i) derivation of empirical global scaling laws; (ii) non-dimensionally similar studies; and (iii) one dimensional transport modelling codes, with the first approach recommended as the most robust at the present time. Special attention is paid to analysis of uncertainties in confinement predictions. Empirical scaling relations for projecting the L-mode to H-mode power threshold based on regression analysis of an extensive database are discussed. Particle and toroidal momentum confinement and their relation to energy confinement are reviewed.

* ITER Physics Expert Group on Confinement and Transport: M. Wakatani (Kyoto U., chair), V.S. Mukhovatov (ITER JCT, co-chair), K.H. Burrell (General Atomics), J.W. Connor (UKAEA, Culham), J.G. Cordey (JET), Yu.V. Esipchuk (Kurchatov Inst.), X. Garbet (CEA, Cadarache), S.V. Lebedev (Ioffe Inst.), M. Mori (JAERI), K. Toi (NIFS), S.M. Wolfe (MIT). ITER Physics Expert Group on Confinement Modelling and Database: J.G. Cordey (JET, chair), D. Boucher (ITER JCT, co-chair), A.N. Chudnovskii (Kurchatov Inst.), J.W. Connor (UKAEA, Culham), J.C. DeBoo (General Atomics), W.A. Houlberg (ORNL), S.M. Kaye (PPPL), Y. Miura (JAERI), Y. Ogawa (U. of Tokyo), M.V. Osipenko (Kurchatov Inst.), F. Ryter (IPP Garching). *Additional contributing authors:* G. Bateman (Lehigh U.), G. Bracco (ENEA, Frascati), D.J. Campbell (NET Garching), T.N. Carlstrom (General Atomics), Yu.N. Dnestrovski (Kurchatov Inst.), T. Fujita (JAERI), A. Fukuyama (Okayama U.), P. Gohil (General Atomics), M.J. Greenwald (MIT), T. Hoang (CEA, Cadarache), G.M.D. Hogeweij (FOM Inst.), A.E. Hubbard (MIT), O.J.W.F. Kardaun (IPP, Garching), J.E. Kinsey (Lehigh U.), J.A. Konings (General Atomics), M. Marinucci (ENEA, Frascati), Y.R. Martin (CRPP/EPFL, Lausanne), D.R. Mikkelsen (PPPL), J. Ongena (EERM-KMS), T.H. Osborne (General Atomics), F.W. Perkins (ITER JCT), A.R. Polevoi (Kurchatov Inst.), M.N. Rosenbluth (ITER JCT), D.P. Schissel (General Atomics), J.A. Snipes (MIT), P.M. Stubberfield (JET), E.J. Synakowski (PPPL), A. Taroni (JET), K. Thomsen (JET), M.F. Turner (UKAE, Culham), N.A. Uckan (ORNL), M. Valovic (UKAE, Culham), G. Vlad (ENEA, Frascati), R.E. Waltz (General Atomics), J. Weiland (Chalmers U.), H. Zohm (Stuttgart U.).

† ITER Physics Basis Editors: F.W. Perkins (ITER JCT), D.E. Post (ITER JCT), N.A. Uckan (ORNL), M. Azumi (JAERI), D.J. Campbell (NET), N. Ivanov (RRC-Kurchatov), N.R. Sauthoff (PPPL), M. Wakatani (Kyoto Univ.). *Additional contributing editors:* W.M. Nevins (LLNL), M. Shimada (JAERI), J. Van Dam (Univ. Texas).

Contents

1. Introduction

The most developed concept for realizing continuous energy (electricity) production from fusion reactions is the tokamak, based on an axisymmetric toroidal plasma. In recent years there has been considerable development of databases and accumulation of knowledge of the behaviour of tokamak plasmas around the world, and these make it possible to design an experimental fusion reactor for energy production. However, a degree of uncertainty still exists in predicting the confinement properties and plasma performance in such a device.

A precise theory of the classical collisional transport losses has been developed. Since this does not completely explain the transport processes across magnetic surfaces (as discussed in Section 2), additional processes driven by plasma turbulence are required to be taken into account. Significant theoretical efforts are being devoted to understanding the cross-field transport in tokamaks due to the turbulence, and a few models are broadly consistent with present experiments. On the other hand, since tokamaks with a range of sizes, operating parameters and heating powers have been constructed, empirical scaling laws derived from these are useful for predicting plasma performance in any new device. Furthermore, the empirical scalings serve as a benchmark for theoretical models. One expects that predictions with such scaling laws will be improved if one imposes dimensional constraints on the form of these laws in the scaling studies. It is also recognized that transport codes solving radial transport equations numerically are also useful for obtaining quantitative predictions. As a result, three approaches are being pursued at the moment for providing predictions for confinement, these are: (a) derivation of empirical global scaling laws; (b) non-dimensionally similar studies; and (c) one dimensional transport modelling codes.

The main strengths of the empirical energy confinement scaling method (described in Section 6) are its simplicity and the fact that all of the physical processes are contained within the data. Its main weakness is that the modelling of the energy confinement time τ_E by a simple log-linear form, or even by more sophisticated forms, can only, at best, be a very approximate description of the physical processes taking place, since no knowledge of the heating, temperature or density profiles, or atomic physics for that matter, is built into the analysis. The log-linear form itself is equivalent to assuming that a single turbulence mechanism with one scale size is responsible for the transport. This seems unlikely to be the case for the ELMy H-mode, the operational mode foreseen for ITER, where the core region may

be dominated by short wavelength turbulence of the gyroBohm type, and the behaviour in the edge region is possibly determined by MHD events such as the edge localized modes (ELMs). These two processes will scale differently with the main scaling parameter ρ^*, the normalized Larmor radius ($\equiv \rho_i/a$).

There is also the possibility that there are hidden parameters that are not being taken into account in the analysis. One parameter that may affect the confinement in some situations, but which is not presently being taken into account, is the edge neutral pressure; another possible important parameter is the Mach number of the toroidal rotation M ($\equiv V_\phi/c_s$). Both these parameters are currently being added to the database, but their effect on the ITER predictions is, as yet, unclear. The degradation of confinement associated with proximity to operational limits, such as the Greenwald density limit, β limit and H-mode power threshold, is still an area of active studies and is not yet well quantified by the available database.

One can assess the statistical uncertainty in the ITER energy confinement time τ_{ITER} using the techniques that are described in Section 6.4. The 95% interval estimate for the prediction of τ_{ITER} from the ELMy H-mode log-linear scaling Eq. (26) is $\tau_{ITER} = 4.4$–6.8 s. With this narrow uncertainty interval, ITER would definitely ignite, although operation at higher current or higher density might be required to preserve ignition at the lower end of this interval. A larger interval, $\tau_{ITER} = 3.5$–8.0 s, has been derived by taking various non-log-linear forms and other considerations into account. At the lower end of this range the minimum Q ($\equiv$ thermonuclear power/input power) would be above 6.

The dimensionless physics parameter scaling technique (described in Section 7) overcomes one of the shortcomings of the energy confinement scaling approach, namely the influence of the plasma profiles on the confinement. In fact, in the simple case of a single dominant turbulence mechanism, one can obtain directly, by a simple projection, from those of current experiments, the temperature and density profiles in ITER, provided the source profiles of heat and particles are the same. A further key advantage of this approach is that the MHD stability properties (i.e. the ELM and sawtooth behaviour, discussed in Section 5) would be the same in ITER as those of the similarity discharge in the present device.

The technique does not entirely overcome one of the major possible shortcomings of the log-linear energy confinement scaling approach, that is the exis-

tence of different types of turbulence dominating the edge and core regions. In this situation, a more complex projection of the profiles of a current device to ITER would be required.

Another concern with this technique is whether all of the key dimensionless parameters have been identified. Several theoretical papers have proposed that the turbulence in a tokamak can be quenched by shear in the toroidal flow. This implies that the Mach number M is an important dimensionless parameter. This is certainly not being kept constant in the ρ^* scaling experiments completed so far, which use neutral beam injection heating. Clearly, experiments in which the Mach number is varied around the values anticipated for ITER, while other dimensionless parameters (i.e. ρ^*, β and ν^*) are kept fixed, are required. (Toroidal momentum confinement is discussed in Section 10.)

The range of uncertainty of the ITER prediction using this technique is quite large for extrapolation from a single machine (see Table 8). This uncertainty comes about from the narrow range in ρ^* available on a given machine (typically a factor of 2) compared to the distance in ρ^* (a factor of 5.5 in JET) by which one has to extrapolate to ITER. To reduce this uncertainty, a database with joint ρ^* scans from different devices will be required.

Work on the full one dimensional modelling approach is progressing well and there are currently several one dimensional models, of both the purely theoretical and the semi-empirical type, which are reasonably successful in reproducing the temperature profiles in the core (Section 8.4). The edge region $0.9 < r/a < 1$ is still a problem, since, at the present time, there is no tested model for this region. Coupled with the strong sensitivity of some of the 'stiffer' one dimensional models to the edge conditions, this makes the prediction of the performance of ITER using this technique rather difficult, as is shown in Section 8.5. An additional uncertainty is the differing manners in which the models treat stabilization of the turbulence by $\boldsymbol{E} \times \boldsymbol{B}$ velocity shear.

The three techniques do at least have overlapping confidence intervals, and efforts need to be directed in the next few years at reducing the confidence interval of each technique.

There is a further uncertainty associated with the use of the ELMy H-mode as the operating regime, in that there is a power threshold that has to be exceeded before the ELMy H-mode is achieved. This is discussed in detail in Section 4; the presently projected power in ITER would appear to be sufficient

to exceed the threshold, provided the transition to the H-mode is achieved at a low density.

Besides the ELMy H-mode, several other improved confinement modes have already been realized, as discussed in Section 3. One of the most promising ones is the negative, or reversed, shear configuration, which involves an internal transport barrier. It can be used to realize a continuous operation of the tokamak, since there is a significant fraction of bootstrap current with a self-consistent profile. The RI-mode also has attractive features such as a high confinement at very high density, approaching or exceeding the Greenwald density limit, with the major portion of plasma energy radiated from plasma periphery.

Furthermore, in order to achieve continuous operation, particle control is essential, in addition to heat exhaust. Thus, for DT burning plasmas, helium ash exhaust is an important requirement; the helium density as well as the impurity ion density must be kept sufficiently low in order to minimize the dilution of fuel ions. To solve these problems, the particle transport properties in fusion plasmas must be characterized; this is discussed in Section 9. In particular, the sawtooth seems crucial for controlling the helium ash and impurities in the central region and ELMs at the plasma edge; these are discussed in Section 5.

Finally, it should be noted that there are several interesting, but unresolved, challenges to our understanding of transport, such as profile resilience, the isotope effect, non-local effects, fast time-scale phenomena, etc. A better understanding of these processes could contribute to improving the prediction of the fusion performance of reactor grade plasmas.

2. Mechanisms of transport in a tokamak

There is a precisely formulated theoretical model for the transport of plasma particles and energy across the magnetic surfaces due to Coulomb collisions in a stable, quiescent toroidal confinement system. This process, which takes account of the particle orbits in an axisymmetric inhomogenous toroidal magnetic field [1] and leads to higher levels of collisional transport than in a cylindrical plasma (which is called classical transport), is known as neoclassical transport [2–5], and will always be present in a tokamak. The classical diffusion coefficient can be estimated by $D_c \approx \nu_{ei}\rho_e^2$ for plasma particles, and the ion thermal diffusivity by $\chi_i \approx \nu_{ii}\rho_i^2$, which

is greater than both D_c and the electron thermal diffusivity $\chi_e \approx \nu_{ee}\rho_e^2$ by a factor of $(m_i/m_e)^{1/2}$. Here, ν is a $90°$ collision frequency and ρ is a Larmor radius, $\rho = V_{th}/\Omega$, which is proportional to the ratio of a thermal speed V_{th} to a cyclotron frequency $\Omega = eB/mc$, where $B = |\boldsymbol{B}|$ is the magnetic field strength and m is the particle mass. The neoclassical transport levels exceed the classical ones by geometrical factors: $q^2\varepsilon^{-3/2}$ in the low collision frequency 'banana' regime ($\nu^* < 1.0$) and q^2 in the collisional fluid limit, as a result of the toroidal geometry. Here, $\varepsilon = r/R$ is the inverse aspect ratio, with r and R being the minor and major radii of the magnetic surface, and $q \approx rB_T/RB_p$ is the safety factor, where B_T and B_p are the toroidal and poloidal magnetic field components, respectively. The collisionality parameter is $\nu^* \equiv \nu_{eff}/\omega_b$, where $\nu_{eff} \equiv \nu_{ei}/\varepsilon$ is the effective collision frequency for particle detrapping, and $\omega_b \approx \varepsilon^{1/2}V_{th}/(Rq)$ is the trapped particle averaged bounce frequency.

In spite of its larger value, neoclassical transport cannot normally explain the observed perpendicular transport in a tokamak. For the usual low confinement regime (L-regime) in auxiliary heated tokamaks, the neoclassical transport theory predicts confinement times longer than those experimentally measured by up to two orders of magnitude for the electrons and one order of magnitude for the ions. Plasma turbulence is probably a dominating effect in causing plasma cross-field transport. However, for some improved confinement regimes and in localized regions of the plasma, transport can be reduced to the neoclassical level [6–8].

The objective of the transport calculations is the determination of the magnitudes and radial profiles of the plasma parameters (such as density, temperature, etc.). To do so, it is useful to formulate the transport problem in a macroscopic way [9]. On transport time-scales, a fluid representation is generally used. Axisymmetry is assumed and plasma observables are averaged on a flux surface over the poloidal angle. In this way, a set of one dimensional fluid like equations can be derived to represent the evolution of the density, momentum and energy for each plasma species:

$$\frac{\partial n_a}{\partial t} = -\frac{1}{r}\frac{\partial}{\partial r}(r\Gamma_a) + S_a \tag{1}$$

$$m_a n_a \frac{\partial V_{ia}}{\partial t} = -\frac{1}{r}\frac{\partial}{\partial r}(r\Phi_{ia}) + M_{ia} \tag{2}$$

$$\tfrac{3}{2}n_a\frac{\partial T_a}{\partial t} = -\frac{1}{r}\frac{\partial}{\partial r}[r(Q_a + \tfrac{5}{2}\Gamma_a T_a)] + P_a \tag{3}$$

and the poloidal magnetic field, B_p, diffusion equation:

$$\frac{\partial B_p}{\partial t} = \frac{\partial}{\partial r}\left(\frac{\eta}{\mu_0 r}\frac{\partial(rB_p)}{\partial r}\right) - \frac{\partial}{\partial r}(\eta J_b). \qquad (4)$$

Here, the subindex a indicates the particle species, the subindex i indicates the components of the velocity vectors, Γ_a, Φ_a and Q_a are the particle, momentum and energy fluxes, and S_a, M_a and P_a are the source, sink and transfer terms for particles, momentum, and energy. The radius r is a generalized minor radius that labels each magnetic surface.

In the magnetic field diffusion equation, Eq. (4), η is the parallel resistivity and J_b is the bootstrap current predicted by neoclassical theory. To understand the origin of this neoclassical effect, we observe that the circulating electrons carry the parallel current in response to the toroidal electric field and other current drive inputs. This parallel current response is determined by the balance between the collisional friction of circulating electrons with ions and the viscous drag on their poloidal flow produced by collisions with the trapped electrons. The predicted parallel resistivity, η, agrees well with experimental results. Another element of the parallel transport, the bootstrap current [10],

$$J_b \approx \frac{\sqrt{\varepsilon}}{B_p}\frac{dp}{dr}$$

has also been shown to be in good agreement with theoretical predictions [11, 12]. Therefore, the theoretical picture of neoclassical parallel transport is consistent with experiment.

The fluxes contain all the dynamic information on the transport processes. While neoclassical theory gives an explicit expression for them, there is not a general form for turbulent transport. In practice, these fluxes have been parametrized by analogy with the structure given by neoclassical theory. For instance, the simplest assumption of diffusive fluxes would give

$$\Gamma_a = -D_a \frac{\partial n_a}{\partial r} \qquad (5)$$

$$\Phi_{ia} = -\chi_{ia}\frac{\partial V_{ia}}{\partial r} \qquad (6)$$

$$Q_a = -\chi_a \frac{\partial T_a}{\partial r}. \qquad (7)$$

In practice, each of the fluxes depends on all the thermodynamic forces (profile gradients) and a full matrix of fluxes must be considered, including non-diffusive and non-diagonal terms. For advanced tokamak scenarios, it is important to include the radial electric field [13] in the transport model, since the gradient of the radial electric field is predicted to reduce transport coefficients [14], and the coupling of its evolution to the set of equations given above. The calculation of the plasma profiles using Eqns (1)–(4) requires the knowledge of these diffusivities and also the appropriate boundary conditions, particularly as the predictions of some 'stiff' transport models involving marginally stable profiles can be sensitive to these [15]. The boundary conditions will be discussed at the end of this Section and in Section 4.2. The determination of the diffusivities has long been the goal of transport studies. There are many existing reviews on this topic [16–23] and, here, we give only a very simplified overview. In understanding the transport coefficients, there are three possible ways of making progress: (1) theoretical; (2) numerical simulation; and (3) experimental. We discuss these approaches in the remainder of this section.

We have seen that the transport theory based on particle collisions can incorporate the geometry of the tokamak magnetic system, but neoclassical theory still assumes that the plasma is in equilibrium and is axisymmetric. Real tokamak plasmas always show the presence of a broad spectrum of fluctuations, e.g. in plasma density, temperature, and electromagnetic fields [17, 24]; thus, real tokamak plasmas are turbulent and intrinsically three dimensional. The turbulent fluctuations give rise to transport across the equilibrium magnetic surfaces and it is necessary to incorporate their effect in a comprehensive transport theory. From the theoretical point of view, most of the instabilities that we think are responsible for the observed plasma turbulence have a very small component of the wavenumber vector parallel to the magnetic field, compared to the perpendicular component. That is, most of the turbulent eddies are quasi-perpendicular to the toroidal magnetic field. Therefore, we can expect that turbulence dominates perpendicular transport, but the influence of the plasma turbulence on the parallel transport is rather small, as experiment confirms.

Hydrodynamic turbulence is an unresolved complex physical problem [25]. Plasma turbulence is even more complex. Since we can describe plasmas as a combination of several fluids (an electron fluid plus ion fluids), we can imagine plasma turbulence as the result of these multiple turbulent fluids coupled through electromagnetic, friction, and energy exchange effects. It is not surprising, therefore, that there is not yet a theory or even a comprehensive approach to this problem.

Plasma turbulence differs in many ways from fluid turbulence, starting from the structure of sources and sinks. Plasma turbulence is driven by the free energy sources of the many plasma micro-instabilities, essentially the gradients of the density and temperature [26–29]. Thus, in the core of the plasma there are micro-instabilities driven by the ion temperature gradient (ITG); these are the electrostatic ITG drift modes and trapped ion modes. These modes are often characterized by a value $\eta_i = d(\ln T_i)/d(\ln n)$, and referred to as '$\eta_i$ modes'. Others are driven by the electron temperature gradient: electrostatic trapped electron and shorter wavelength electromagnetic η_e drift modes, and micro-tearing modes. There are also fluid like instabilities driven by pressure gradients: the current diffusive ballooning [30] and neoclassical tearing modes [31–33]. At a collisional plasma edge, there is a range of fluid instabilities driven by gradients in pressure, resistivity and current. In Table 1, we give a summary view of plasma instabilities that are possible underlying mechanisms for plasma turbulence in tokamaks. In the edge region, it is possible that atomic physics processes can play a part, so that in addition to those instabilities shown in Table 1, another candidate at the plasma edge is the ionization instability [34–36], even if the validity of the linear theories has been questioned [37]. The plasma drives couple directly, through these instabilities, to a broad range of turbulence scale lengths. Therefore, in general, one cannot separate between the driving and inertial ranges, as is done in hydrodynamic turbulence. The dissipative terms do not have the simple form of a collisional viscosity. The complicated magnetic geometry of a tokamak adds even more difficulties to this problem. In spite of this, research on tokamak plasma turbulence has proceeded at several levels: (1) renormalization of simple sets of equations modelling the turbulence; (2) scale invariance and dimensional analysis techniques; and (3) numerical solution of turbulence models.

The renormalization approach starts from perturbation theory. When summing the perturbation series, the characteristic time-scale associated with the non-linear processes, τ_c, must be determined in a self-consistent manner [38, 39]. If it is approximated by the linear time-scale (inverse of the linear growth rate, γ, of the appropriate plasma instability), conservation laws are violated. The renormalization approach introduces a recursive determination of the non-linear time-scale (in a way similar to the determination of the electron mass in quantum electrodynamics). The most common closure scheme is the direct interaction approximation. The adequacy of this closure scheme has been tested with numerical calculations within the accuracy achievable with present numerical resolution. The determination of the basic turbulence scale length, Δ_T (mixing length like length-scale) [40], and the decorrelation time, τ_c, allows the construction of an effective turbulent diffusivity, $D_T \approx \Delta_T^2 \tau_c$. In practice, to apply renormalization techniques, the problem must be reduced to a one, or at most two, equation model. Otherwise it is practically impossible to solve the problem analytically, or even numerically. Analytical approaches are also limited because the approximations needed to solve the equations restrict the applicability of the solutions to a small range of plasma parameters, while experiments cover, in general, a broad parameter range. However, these techniques are essential for making progress in understanding. In some simple models [41–43], it has been shown that Δ_T is proportional to the inverse perpendicular wavenumber, $k_\perp$, and the following form for the turbulence diffusivity can be adopted $D_T \approx \Lambda \gamma / k_\perp^2$, where Λ is a weak function (logarithmic or just a constant) of the plasma parameters [44, 45]. This formulation of the turbulent diffusivities has been adopted in an ad hoc fashion in some of the transport models.

The scale invariance approach [46, 47] is an alternative approach for the determination of the transport coefficients. It is based on the idea of intermediate asymptotics [48], and, in some simple models, it has been shown to be equivalent to the renormalization group technique [49]. In this approach, one identifies all the independent transformations under which the dynamical equations are invariant. It has been applied to several types of turbulence dynamics and it can be a powerful tool in identifying the main dependences of the diffusivities. The minimal form of the scale invariance approach is the dimensional analysis that will be discussed in the context of the empirical determination of the transport coefficients. Another analytical approach invokes marginal stability criteria, e.g. [50–52]. Yet another approach is the study of the saturation of turbulence spectra by non-linear plasma dynamics [53–55].

The numerical solution of the primitive equations allows us to cover a broader parameter range than by the analytical approaches. It is a promising method when computer capabilities allow calculations with sufficient resolution. The numerical calculations can be carried out at different levels as follows.

Table 1. Main instabilities that contribute to the anomalous transport losses in tokamaks [29] (η_j = density scale length/temperature scale length for species j).

Group	Instability	Source of free energy	Subspecies	Properties
Ion Instabilities	η_i modes	∇T_i	Slab modes Toroidal modes Trapped ion modes	$\omega \leq \omega_{*i}$ $\eta_i > \eta_{ic}$ $L_{T_i}/R < (L_{T_i}/R)_{crit}$
Electron instabilities	Electron Drift Waves	∇n_e	Slab modes Toroidal modes	$\omega \approx \omega_{*e}$
	Dissipative trapped electron modes	∇T_e		$\varepsilon\omega < \nu_e \leq \varepsilon^{3/2} V_{the}/qR$ $\varepsilon_n q < k_\perp \rho_s \leq \nu_e L_n / \varepsilon c_s$
	Collisionless trapped electron modes	∇T_e		$\nu_e < \varepsilon\omega \leq \varepsilon^{3/2} V_{the}/qR$ $\varepsilon_n q < k_\perp \rho_s \leq 1$
	η_e modes	∇T_e	Slab modes Toroidal modes	$\omega_{pe}/c < k_\perp < \rho_e^{-1}$ $k_\parallel V_{the}, \omega_{be} < \omega < \omega_{*e}$
	EM drift waves	∇n_e		$\omega \approx \omega_{*e}, k_\perp \rho_s \leq 1$
Fluid like instabilities	Resistive ballooning modes	∇P	Fast modes Slow modes	$\omega \approx \omega_{*e}$ $k_\parallel V_{the} < \omega$
	Current diffusive ballooning modes	∇P		$k_\parallel V_{the} < \omega$

Here ω, $k_\parallel$ and $k_\perp$ are the frequency and parallel and perpendicular wavenumbers of the instability, respectively; ω_{*j} is the diamagnetic frequency of species j, ω_{pe} the electron plasma frequency, ρ_s the ion Larmor radius at the electron temperature, c_s the sound speed, L_T the temperature scale length of species j, ε_n the ratio of density scale length L_n to major radius R and $\eta_j = L_n/L_{T_j}$.

(1) *Particle calculations.* In this case, the motion of individual particles in the plasma is followed in time. This approach requires considerable computational resources. A great deal of progress has been made by using the gyrokinetic approach. In this approach, the particle motion is averaged over the fastest time-scale, Ω^{-1}, the inverse cyclotron frequency.

(2) *Fluid calculations.* Moments of the distribution function for each plasma species are followed in time as fluid quantities. A closure scheme is needed to limit the number of moments. When the closure scheme incorporates Landau damping, the approach is called gyrofluid [56]. These are absent from reactive fluid models [57].

Considerable progress has been made in recent years through gyrokinetic [58, 59] and gyrofluid [60] calculations, and it has been shown that these calculations can be used for the determination of the scaling of Δ_T and τ_c with plasma parameters [15]. At present, there is not good agreement between these two numerical models; active work is under-

way to understand and resolve the reasons for the differences.

The turbulent transport picture seems to fit some of the qualitative features of perpendicular transport in a tokamak. To provide a sound basis for this mechanism, research effort has been concentrated on identifying the connection between the observed plasma fluctuations and transport. In doing so, it is convenient to distinguish between two plasma regions: the core and the edge. At the plasma edge, the fluctuations are, in general, large (of the order of the equilibrium quantities). They are dominantly electrostatic, unless the plasma pressure approaches the ideal magnetohydrodynamic (MHD) stability limit, and, because of the low plasma temperature, detailed measurements can be made with probes. From these measurements, it has been inferred that the edge particle loss can be explained by fluctuation induced transport [24].

Core fluctuation levels are low (a few per cent of the equilibrium values of density, etc.) [17, 24]; their measurement by non-intrusive techniques is complicated. Several of these techniques are used:

for instance, beam emission spectroscopy [61], reflectometry [62–64], and correlation measurements of electron cyclotron emission (ECE) signals [65, 66]. The first two measure density fluctuation levels and the third electron temperature fluctuations; therefore, we have no knowledge of the turbulence driven fluxes. The heavy ion beam probe [67] can determine both density and potential fluctuations, and, therefore, the particle flux. However, its use has been limited. The fluctuation measurements indicate that the spectrum is peaked at long wavelengths and radial correlations lengths are of the order of a centimetre or less. In some experiments, fluctuation levels seem to correlate well with global, and even local, transport [68], but without determination of the fluxes, no unambiguous correlation with transport can be established. The turbulence characteristics are consistent with calculations of ITG driven turbulence, but comparisons have only been carried out for a limited number of discharges. Plasma core turbulence may have a significant magnetic component. Although there are measurements of the magnetic field fluctuations at a fixed wavelength [69], there is not yet a direct measurement of this component for a broad range of wavenumbers, and its role in transport is controversial [70]. Recently, other fluctuation measurement techniques have become available that enable us to measure ion temperature and parallel velocity fluctuations [68]. Hopefully, these measurements will help in clarifying the plasma turbulence drive and will shed some light on turbulence induced energy transport.

The turbulence driven transport theory has also been effective in the interpretation of improved confinement regimes. For instance, there is much theoretical and experimental evidence that $\boldsymbol{E} \times \boldsymbol{B}$ velocity shear (i.e. radially varying profile of the $\boldsymbol{E} \times \boldsymbol{B}$ plasma flow) can reduce turbulent transport, as will be discussed in Sections 3.3 and 4.1. The theories seem consistent with the observation of a causal correlation between the buildup of the sheared radial electric field and the suppression of turbulence [71]. Some of the limitations of the transport based on turbulence are discussed at the end of this section and in Section 8.

Since fully convincing transport predictions cannot yet be made from first principles, it is necessary to use empirical approaches to predictive transport. Even in this case, the transport coefficients cannot be arbitrarily chosen. There are dimensional constraints that follow from invariance principles [72,73], discussed more fully in Section 7. These constraints

reduce the number of experiments to be performed in order to determine these coefficients. To establish these constraints, we need to identify the relevant invariance principle and dimensionless parameters. This can only be done within some given theoretical framework. The broader the framework, the less constrained are the transport coefficients. On strict theoretical grounds, even assuming transport is due to quasi-neutral plasma physics processes, the number of dimensionless parameters for a confined plasma is large, up to 19 have been identified [74]. They include plasma physics parameters such as β, the ratio of the plasma kinetic pressure to the magnetic pressure, the collisionality, $\nu^* \equiv \nu_{eff}/\omega_b$, and the normalized ion Larmor radius, $\rho^* \equiv \rho_i/a$. There are also parameters describing the magnetic field geometry, such as the safety factor q, aspect ratio $A \equiv R/a$, the ellipticity κ, and triangularity δ of the plasma cross-section, and parameters representing the plasma composition: T_e/T_i, m_e/m_i, Z_{eff}, etc. For a local diffusion coefficient, we have to include the parameters related to plasma profiles, such as the ratios of scale lengths, L_T/R, L_n/R, etc. From dimensional arguments, and assuming a power law dependence on ρ^*, the diffusivities can be expressed in the following form:

$$D = c_s \rho_s (\rho^*)^\alpha F(\nu^*, \beta, q, A, \kappa, \delta, L_T/R,$$
$$L_n/R, \ldots, m_e/m_i, T_e/T_i) \quad (8)$$

where $c_s \equiv \sqrt{T_e/m_i}$ is the sound speed, $\rho_s = \sqrt{2m_iT_e}/eB$ is the ion Larmor radius evaluated at the electron temperature, and F is a function of the dimensionless parameters that is to be determined. The main change in plasma parameters in going from present experiments to the fusion reactor is in the value of ρ^*. Therefore, determining the transport scalings with ρ^* is critical. Two limits that are often discussed in transport studies are defined by Eq. (8). When $\alpha = 1$, the scaling law is called gyroBohm. This is the expected scaling from most local turbulence theories for which the turbulent scale length Δ_T is proportional to ρ_i. For $\alpha = 0$, the scaling is called Bohm, when the turbulence scale length involves the macroscopic size of the plasma. Of course the confinement time can be determined by boundary conditions on the transport equations, as well as the thermal diffusivities themselves; this could introduce a different dependence on ρ^* [75] as discussed in Section 4.2.

A series of experiments have been performed to resolve the scaling of D with different dimensionless parameters, in particular with ρ^*. They will be dis-

cussed in Section 7. In a given device, tokamak discharges that have the same dimensionless parameters apart from ρ^* must be produced. The level of control required for these experiments makes them very difficult. In present devices, only a limited range of variation in ρ^* can be achieved (less than a factor of two). A larger range of variation in ρ^* can be obtained by using different devices, but in this case the experiments are even more difficult. At present, and for the low confinement L-mode, some experimental results for the energy confinement time, τ_E, are consistent with, or close to, Bohm type scaling [74, 76, 77], while others are between Bohm and gyroBohm [78]. In the high confinement mode (H-mode), the diffusivities seem to be consistent with gyroBohm scaling. However, the problem is more complicated than stated because the electron diffusivity may be different from the ion diffusivity. The separation between both transport channels requires more diagnostics and makes the analysis of the experimental results more difficult. Only a few experiments separating electron and ion channels have been performed; they will be discussed later in this section. Scalings of D with β and ν^* have also been carried out.

The basis of this empirical approach to the determination of the transport coefficients needs to be established. The non-dimensional parameter scalings are based on plasma physics. However, plasma experiments are affected by edge conditions, plasma wall interactions, etc. If these boundary conditions modify confinement in an essential manner, the non-dimensionally similar discharges would not be enough to determine the scaling of the transport coefficients. To test the basis of this approach, discharges with the same dimensionless parameters must be set up in devices of different sizes to test if they are equivalent. Experiments comparing similar discharges from DIII-D and JET have given positive results [79].

The basic picture and scalings for plasma transport presented here are challenged by some experimental observations. These observations underline the fact that we are far from having resolved all the scientific issues in plasma transport. Examples of these open questions are as follows.

1. Bohm scaling and local fluctuations

Since the basic scale length of the microinstabilities is ρ_i, a simple random walk argument leads to transport coefficients that are characterized by a gyroBohm scaling. However, this seems to disagree with the experimental observation in L-

mode plasma confinement. To explain a departure of the core turbulence from a gyroBohm scaling, two kinds of models have been proposed so far. First, many instabilities are sensitive to the toroidal geometry. This geometrical effect introduces a coupling between poloidal components. In a homogeneous system, this results in eigenmodes that extend over the size of the device, similar to phonons in a crystal. In the linear regime, this leads to the concept of 'global' eigenmodes that exhibit non-gyroBohm radial lengths and growth rates [80–83]. However, it is expected that these correlations over large distances are destroyed in a fully developed turbulence, which should, therefore, exhibit a gyroBohm scaling. This may not be true close to the turbulence threshold when the turbulence level is low. Indeed, a simplified numerical simulation shows long lived global modes in this case. More precisely, the correlation lengths scale as ρ_i, but the correlation time does not follow the gyroBohm prediction [84]. The second kind of model relies on the concept of self-organized criticality [85], for which the paradigm is the sandpile. Such a system exhibits large scale events (avalanches), which dominate the transport scaling in spite of their scarcity [86,87]. This leads to a non-gyroBohm behaviour. A velocity shear results in a recovery of a gyroBohm scaling through a decorrelation process of the large scale events [88]. The correlation lengths scale as a gyroradius in this model. Moreover, the gradients are below the critical value for moderate fluxes. Most of these models predict the scaling of the correlation lengths and times. Therefore, the experimental determination of the scaling of correlation functions should clarify this issue.

2. Isotope effect on plasma confinement

In Eq. (8), if we only consider the scaling of D with the ion atomic mass, we obtain $D \propto A_i^{\alpha/2} F(A_i)$ ($\alpha = 0$ for Bohm models, $\alpha = 1$ for gyroBohm). Unless there is a strong dependence of F on the ion mass, this result does not agree with experiment. One observes in almost all tokamaks that plasma properties depend on the plasma gas [89], and, contrary to what is expected from the simple scaling, confinement has a positive dependence on A_i. Although there are some preliminary indications supporting a positive dependence of confinement on A_i from gyrokinetic calculations and theories based on nonlinear ion Landau damping [53], there is not yet a satisfactory theoretical explanation of this effect. For ELMy H-mode, ELMs could cause an isotope effect

to appear through boundary conditions. Phenomenological observations will be described in Section 3.

3. Fast time-scales and non-local effects

When a transient local perturbation in plasma density n or temperature T is applied to a tokamak, one might expect its effect to propagate across the magnetic surfaces on a time-scale that is related to the diffusion coefficients characterizing steady state particle and energy balance. In fact, observations of heat pulses generated by, for instance, sawtooth collapses or localized auxiliary heating such as ECRH, show that these signals propagate as if the diffusion coefficient exceeded that determined from steady studies by a factor typically in the range of 1–5 [90]. This could be understood if the diffusion coefficients are themselves functions of n and T and their radial gradients, i.e. the transport fluxes are non-linear functions of the driving gradients. In fact, many theories of turbulent transport have this feature. L-mode transient transport experiments on ASDEX-Upgrade [91] indicate that for small, ECH generated electron temperature transients, the response is adequately described by such diffusivities.

However, a number of dramatic observations involving transient behaviour pose serious challenges to our understanding of the processes underlying transport in tokamaks. Three examples are:

(i) the fast propagation of the cold pulse [92] associated with the injection of pellets into a tokamak;

(ii) the almost instantaneous effect of the low-to-high (L–H) confinement transition at the plasma edge on the transport coefficients in the plasma core as observed in JET [93, 94]; and

(iii) the heating of the plasma centre within a few milliseconds of injecting impurities at the plasma edge in TEXT [95] and TFTR [96].

These transient effects can propagate radially with velocities $\sim 10^2 \, \mathrm{m \cdot s^{-1}}$, two orders of magnitude faster than results from a normal diffusive process. Evidence that the magnetic configuration remains as nested toroidal surfaces is needed to support these transient tests of thermal diffusivities.

An entirely satisfactory mechanism to explain these surprising results is not yet available. However, several conjectures have been proposed. The ones based on long correlation lengths of either fluctuations or the transport events given above for Bohm scaling can be applied here. The rational surface at $q = 1$ appears to play a role in the fast propagation of the cold pulse [97]. This might suggest that some MHD activity is triggered by the cooling there and, possibly through toroidal coupling, affects the radial transport. Another model involves the non-linear growth and interaction of neoclassical magnetic islands on different rational surfaces. This produces regions of stochastic magnetic field when the islands overlap spatially. The resulting rapid plasma transport allows fast communication across the plasma radius [98]. A further proposal is stimulated by the empirical observation that tokamak plasmas have a tendency to take up certain preferred radial profiles, termed profile consistency or resilience. This model assumes that turbulent processes associated with MHD instabilities cause the profiles to relax to these special ones on a fast time-scale. Theoretical arguments have been advanced for these preferred profiles and the idea has been incorporated in the so-called 'canonical temperature profile' transport model, which can also describe the inward heat pinches sometimes observed in tokamaks [99,100]. Similar fast propagation may be anticipated from stiff transport models such as those that drive profiles to marginal stability [15].

3. Experimental description of confinement and transport

3.1. Introduction

Early tokamaks were heated ohmically, but it became clear that ohmic heating to ignition was not efficient, so the confinement properties of tokamaks with auxiliary heating by energetic neutral beams or radio frequency waves have been thoroughly investigated. Nevertheless, there will be phases in which ITER will be without additional power and the confinement properties of ohmically heated devices can shed light on our understanding of confinement in general. Thus, in Section 3.2, we first characterize confinement in ohmically heated tokamaks. The application of auxiliary power, while producing higher energy content in the tokamak, is associated with a degradation in energy confinement time relative to that in the ohmic phase; this so-called L-mode is also discussed in Section 3.2. As a consequence, an ignited tokamak operating in L-mode would have to be unacceptably large. Fortunately, it was discovered that when sufficient auxiliary power was applied, a transition to an improved confinement mode, the H-

mode, occurred. This mode, which involves the formation of an edge transport barrier, forms the basis for the design of ITER, and its confinement properties are described in Sections 3.3 and 6.2. A number of other improved confinement modes have since been discovered. In Section 3.4, improved confinement modes associated with internal transport barriers, including those involving negative, or low, magnetic shear in the centre of the plasma, are described, and in Section 3.5, improved confinement regimes involving edge radiation are discussed.

3.2. General results for ohmic and L-mode

An ohmic plasma is one that is resistively heated with a power given by $I_p V_{res}$, where I_p is the plasma current and V_{res} is the resistive portion of the loop voltage. The electrons are heated directly, while the ions are heated by the equipartition energy flow from the electrons. There are two principal ohmic regimes. At low density, the confinement time is found to increase linearly with density ($\chi_e \propto 1/n_e$) up to some critical value; this is the linear ohmic confinement (LOC) regime. Beyond this critical density, the confinement time remains constant with density; this is called the saturated ohmic confinement (SOC) regime. The coupling between the electrons and the ions becomes stronger in the LOC as density increases and electron temperature decreases, causing T_i to increase [22, and references therein].

In the LOC regime, the energy confinement time is also found to increase with device size and with safety factor. The confinement time in the LOC is conveniently represented by the neo-Alcator scaling [101]

$$\tau_E(\mathrm{s}) = 0.07 n_e (10^{20} \ \mathrm{m}^{-3}) q \kappa^{0.5} R(\mathrm{m})^2 a(\mathrm{m})$$

where q is the safety factor at the plasma surface, κ is the elongation of the plasma cross-section, R is the major radius and a is the minor radius. From a series of ohmic experiments on the Japanese tokamaks, JFT-2, JFT-2M, JT-60 and DIVA, the parametric dependence of the critical density for transition from LOC to SOC with gas fuelling was found to be [103]

$$n^{crit}(10^{20} \ \mathrm{m}^{-3}) = 0.65 A_i^{0.5} B_T(\mathrm{T})/qR(\mathrm{m})$$

where B_T is the toroidal magnetic field and A_i is ion mass number in AMU. The energy confinement time was found to be higher in deuterium plasmas relative to hydrogen ones, i.e. $\tau_E \propto A_i^{\alpha}$ with $\alpha = 0.5$ in small

tokamaks [22] and with $\alpha = 0.2$ in large machines such as JET [103] and TFTR [104].

Although in some devices (e.g. Alcator A [105], ISX-A [106] and T-11 [107]), the level of energy confinement at high density can be explained by the neoclassical ion thermal conduction losses, in other experiments with gas fuelling, an anomalous high ion conduction was identified as a reason for the confinement saturation. Density profile peaking resulting from pellet injection on Alcator C was associated with confinement time increases in otherwise SOC discharges up to values predicted by the LOC scaling for intermediate densities [108]. This re-establishment of LOC scaling at high density was also seen on other tokamaks with pellet injection and resulting density profile peaking. The strong influence of edge conditions on core confinement in ohmic plasmas was shown in ASDEX experiments in which a reduction in the gas feed at a certain time in the discharge led to a slow peaking of the density and current profiles, and re-establishing the linear dependence of confinement time on density [109].

While confinement times given by the LOC scaling could be extrapolated to values acceptable for reactor scenarios, it was recognized early that the ohmic regime was inefficient for achieving the necessary temperatures. As temperature increased, the resistive heating decreased, and, therefore, auxiliary heating would help to increase the plasma temperature to that level required for significant fusion power production. Auxiliary heating was performed by a variety of techniques, including neutral beams and RF (ion and electron cyclotron, lower hybrid, and ion Bernstein waves). While the temperature and stored energy increased with this auxiliary heating, the incremental increase in stored energy was less than that expected from the ohmic scalings, resulting in a degradation of global confinement. This mode of operation, with degraded energy confinement time, is called the L-, or low confinement, mode. Characteristic features of L-mode plasmas are the low temperatures and temperature gradients near the plasma periphery.

The L-mode is typified by not only a degradation in confinement from the ohmic value, but a continuous degradation of confinement with increasing auxiliary heating power. While the confinement was found to be a strong increasing function of q in ohmic discharges, for auxiliary heated discharges the confinement is not found to be a function of q, but rather scales linearly with the plasma current. Any direct dependence of confinement time on plasma

current in ohmic discharges may be masked by the explicit dependence of the ohmic heating power on the plasma current. The global confinement of auxiliary heated plasmas, unlike that of ohmic discharges, shows no explicit dependence on the toroidal magnetic field [101]. Under direct electron heating, such as ECRH on T-10 [110] or LH on Tore-Supra [111], when the electron transport losses dominate, the confinement increases linearly with density. This suggests that ($\chi_e \propto 1/n_e$) may be intrinsic to the electron transport dominated regime (or to regimes with no fast ion component). With ion heating and ion transport losses predominant (e.g. with NBI, ICRH), the global confinement depends only weakly on plasma density, although more of a dependence on plasma density is found for the thermal energy confinement time [112]. Increased plasma elongation and plasma size result in higher confinement.

The effect of the plasma isotope on confinement is ambiguous. While most experiments show some improvement of confinement on A_i, the magnitude of the effect varies from device to device and from isotope to isotope (see [113, 114] and [22, and references therein]). Comparing discharges with H and D for either the working gas or beam species, no dependence of confinement on ion mass was observed in L-mode discharges in DIII-D or Tore-Supra. A weak dependence ($A_i^{0.3}$) was observed in ASDEX, PDX, TFTR and JET. A stronger dependence ($A_i^a, \alpha \geq 0.45$) was observed in DIII, DIII-D at ECRF heating, and in JT-60U. In more recent DD/DT L-mode experiments on TFTR, the isotope effect was found to be strong for both the thermal plasma and beam component, with $W_{th} \propto A_i^{0.5-1.0}$ and $W_{beam} \sim A_i^{0.7}$ [115]. The isotope effect was found to be stronger at higher beam power. In TFTR experiments with ICRF heating, the isotope scaling in L-mode discharges was found to be $A_i^{0.35-0.5}$ [116] (see Section 6.3).

It is important to note that the L-mode confinement parametric dependences are generally consistent with the Bohm and high-β scaling constraints [112].

Perturbative experiments (i.e. current ramps) have shown that the plasma current global variable is not necessarily an appropriate parameter with which to describe the energy confinement. In these experiments [117, 118], the energy confinement time was found to change on time-scales much slower than that of the current ramp and close to that of the current profile relaxation. This led to the recognition that the current profile, not the global plasma

current, may be the controlling factor in determining the plasma energy transport, with higher confinement being associated with the more peaked current profile for this transient phase.

As with ohmic plasmas, the anomalous transport loss is governed by microturbulence whose source, however, is still not known. Measurements of density fluctuations during parametric scans show changes in fluctuation levels and radial correlation lengths consistent with the resulting change in energy confinement [119].

3.3. Regimes with edge transport barrier (H-mode) and recommended regime for ITER

The high confinement mode (H-mode) associated with a spontaneous formation of an edge transport barrier was first discovered in ASDEX [120] and, as is discussed in Section 4, has now been seen on a wide variety of magnetic confinement devices under a wide range of conditions.

As is discussed in Section 6, the general forms for the global energy confinement scaling in L-mode and H-mode are similar, although the former scaling is Bohm like, while the latter is more gyroBohm. The H-mode exhibits global energy confinement values about a factor of two better than L-mode. Part of this is due to the formation of the edge transport barrier, as is discussed further in Sections 4.1 and 4.2. Another part of this improvement is due to a reduction in local transport throughout the plasma after the L–H transition. Experiments comparing L-mode and H-mode local transport rates under as similar conditions as possible have shown reductions in the electron thermal diffusivity, ion thermal diffusivity and angular momentum diffusivity, with the reduction in the electron thermal diffusivity being especially prominent. An example of these results is shown in Fig. 1 [121].

There are several reasons why the H-mode has been chosen over the other improved confinement modes as the primary operating mode for ITER.

(1) As is discussed further in Section 4, the H-mode is robust, having been seen under a wide variety of conditions in a large number of devices. Many of the other improved confinement regimes (e.g. TFTR 'supershot' [122], TEXTOR RI-mode [123, 124], ISX Z-mode [125], ASDEX counter-injection mode [126]) have been seen in only one or a few
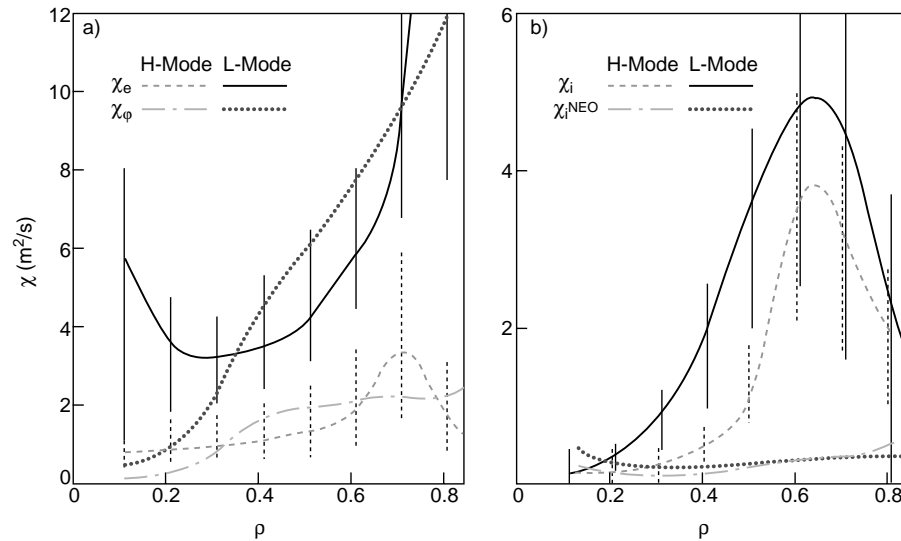
Figure 1. Comparison of electron thermal, ion thermal and angular momentum diffusivity in the limiter L-mode and divertor H-mode discharges in DIII-D. The discharges were prepared to have very similar plasma shapes and identical line averaged densities, plasma currents, toroidal fields and input powers at the time of comparison [121].

devices under a limited range of operating conditions. In addition, steady state operation in many of these modes remains to be demonstrated. The H-mode with edge localized modes (ELMy H-mode) has been run for as long as 20 s on JET [127], with the duration limited only by power supply considerations.

(2) The H-mode requires little in the way of special wall conditioning, unlike, for example, the supershot regime, although it does benefit from reduced particle recycling.

(3) The H-mode exhibits flat density profiles in the plasma core, which are consistent with reduced peaking of impurities and helium ash. The DIII-D results [128], for example, show flat helium density profiles in H-mode plasmas with $n_e(r)/n_{He}(r)$ constant.

(4) The H-mode exhibits good confinement even in high density cases where the electron and ion temperatures are equilibrated; this is consistent with the alpha particle heating and high density operation that will be needed for ITER. Several of the other improved confinement modes (high β_p mode [129], supershot and enhanced confinement modes associated with weak or negative central shear) have only been seen so far in cases where $T_i \gg T_e$.

(5) The H-mode requires no special current profile control for long pulse operation, unlike the operating modes with negative central magnetic shear. Although the negative central shear operating regime may ultimately improve the characteristics of a tokamak reactor, it is not sufficiently investigated to be considered as the main operational regime for ITER.

The physics of the L–H-mode transition, including scalings for the heating power required for the transition, are discussed in Section 4, and the effects of large scale MHD phenomena (ELMs and 'sawteeth') on the H-mode confinement are described in Section 5.

3.4. Regimes with internal transport barriers

Recently, core or internal transport barriers (ITBs) have been discovered that lead to significant enhancements in confinement and plasma performance. Transport barriers associated with weak or negative shear have been observed on all of the large tokamaks (the enhanced reverse shear (ERS) mode on TFTR [6], negative central shear (NCS) mode on DIII-D [130], optimized shear scenario [131] and PEP mode [132] on JET, and reverse shear mode on JT-60U [133]). Internal transport barriers are also observed in plasmas with monotonic q profiles.

3.4.1.   Barriers associated with reversed
        or weak magnetic shear

For most of the regimes with reversed magnetic shear, shear reversal is obtained through a combination of a rapid current ramp and auxiliary heating early in the plasma discharge. The enhanced performance of these plasmas is, at present, transient, however, and experiments are now being designed to extend this regime of operation to steady state. Recently, ELMy reversed shear H-mode discharges were sustained in DIII-D [134] and JT-60U [135] for 1.5 s, although with a relatively low figure of merit $F_{Fus} = \beta_N H/q^2 = 0.5$, where H is the enhancement factor above the L-mode confinement scaling [136] and $\beta_N = \beta/(I/aB_T)$. The highest transient value of F_{Fus} achieved so far in negative central shear discharges is about 1.2 [6], which should be compared with $F_{Fus} = 0.64$ expected in ELMy H-mode in ITER.

In TFTR ERS plasmas [6, 137–139], dramatic reductions in the ion thermal conductivity and particle diffusivity are found shortly after the onset of nearly balanced neutral beam injection. Both quantities fall to or below present day standard neoclassical predictions. Evidence for exceptional particle confinement is obtained through particle balance analysis [6,137,138], as well as tritium and helium gas puffing and lithium pellet injection [140]. The transport reductions are accompanied by local reductions in the fluctuation levels [139]. Interestingly, the electron thermal transport appears to be relatively unaffected by the reduction in fluctuations. This observation, coupled with the observed improvement in particle confinement, may have practical implications with respect to the issue of helium ash accumulation in such regimes. Pressure and density profiles in ERS plasmas are characterized by strong central peaking, with the transport barrier located at or near the location of the minimum in the q profile. Steady state operation is limited by plasma disruption, triggered either by q_{min} falling below 2, or by the high pressure gradient region slowly expanding through the radius of weak magnetic shear.

Significant reductions in transport are also observed on DIII-D in NCS plasmas with ITBs [130, 141, 142]. As in TFTR, the thermal transport reduction is observed primarily in the ion channel. Large increases in the ion temperature, electron temperature and electron density are observed inside the radial location of the ITB, with large gradients in the ion temperature and electron density developing in the region of the ITB. The ion thermal diffusivities are below standard neoclassical levels in the core for NCS plasmas with L-mode plasma edge properties. For NCS plasmas with H-mode plasma edges in DIII-D, the ion thermal diffusivities are below standard neoclassical levels for nearly the entire plasma cross-section [143], and fluctuation levels, measured by far infrared scattering, are dramatically reduced as well. L-mode edge NCS plasmas are characterized by a dramatic peaking of the density profile, much like TFTR ERS plasmas. Large reductions in the particle diffusivity are observed inside the ITB. The cores of these discharges are in the second stable regime for ballooning modes due to the weak or negative magnetic shear and high central q. However, L-mode edge NCS discharges normally disrupt when normalized β, $\beta_N = \beta/(I/aB)$, exceeds 2.0–2.5 as a result of becoming unstable to global resistive interchange modes. In general, for H-mode edge NCS plasmas, the broad density profile results in a relatively broad pressure profile that is better aligned with the weak shear and exhibits greater stability. Larger β_N values are obtained in plasmas with H-mode edges than with L-mode edges, which is consistent with ideal MHD calculations [144]. Contrary to the observations on TFTR, these plasmas are stable to the passing of q_{min} through 2.

On JT-60U, transport barriers are also observed with [133] and without shear reversal. With shear reversal, the region of small transport is again located near q_{min}. It is inferred that the electron thermal transport can also be reduced in these plasmas [145], in contrast to the conclusions drawn from TFTR and DIII-D core transport barrier formation with reversed shear. From power and particle balance analysis, it also appears that the improvement in confinement is constrained to regions of steep gradients. Radial expansion of the transport barrier after formation is observed. It has been demonstrated on JT-60U that the barrier can be sustained if RF power is substituted for neutral beam power, indicating that the physics of transport barrier sustainment does not depend on particle fuelling or density gradients per se [146]. Like TFTR ERS plasmas, but unlike DIII-D NCS plasmas, these plasmas exhibit high disruptivity near $q_{min} = 2$.

In the JET tokamak, transport barriers are also observed with reversed or weak magnetic shear [131, 147–149] through use of lower hybrid current drive, ICRH heating, or pellet fuelling. The transport barriers are characterized by strong gradients in the ion and electron temperature, electron density, and

toroidal rotation. Power balance analysis indicates that thermal conduction in both the electron and ion channels is reduced in these plasmas. The particle diffusivity is reduced, and the confinement of electrons deposited in the core is sometimes similar to that observed in DIII-D NCS, TFTR ERS, and JT-60U ERS plasmas. A characteristic of the plasma evolution is the large radial expansion of the transport barrier once the barrier is formed. Using the radial location of the minimum in the q profile obtained from equilibrium calculations, it is inferred that the barrier moves far outside q_{min}, in contrast to the observations made on other machines. It is inferred that the optimum q profile for the formation of the barrier has slightly negative or flat shear with $q > 1$ everywhere.

Candidate theory based models for transport barrier formation have been proposed that rely on the shear reversal itself [150, 151], $\boldsymbol{E} \times \boldsymbol{B}$ shear suppression [6, 130, 137–141, 152], strong Shafranov shift gradient [151, 153], or a combination of two or all three of these mechanisms.

There is experimental evidence that $\boldsymbol{E} \times \boldsymbol{B}$ shear is necessary and Shafranov shift effects and shear reversal are not sufficient to sustain enhanced confinement [154]. Transport and fluctuation levels remain low until the characteristic shearing rate of turbulence [155] is reduced through the applied torque below a threshold value. Recent observations of local core poloidal velocity excursions prior to the onset of ERS confinement point to a possible similarity in the bifurcation physics of core and edge barrier formation [156].

In DIII-D high performance NCS plasmas, there is both a temporal and spatial correlation between the reduction in transport and the reduction in electrostatic fluctuations when the $\boldsymbol{E} \times \boldsymbol{B}$ flow shear exceeds the local microinstability growth rates [121]. This large flow shear results from the strong peaking of toroidal rotation inside the region with weak or negative magnetic shear, in contrast to TFTR ERS plasmas, where the origin of $\boldsymbol{E} \times \boldsymbol{B}$ flow shear is large pressure gradients formed in part by strong central fuelling.

Although Shafranov shift gradient stabilization extrapolates well to a reactor scale device, the ρ^* scaling of the diamagnetically driven $\boldsymbol{E} \times \boldsymbol{B}$ shear stabilization does not extrapolate favourably unless an external source of rotation (for instance the neutral beam injection or ion Bernstein wave (IBW) radio frequency heating) is applied. However, further theoretical and experimental confirmation of these ideas

for transport barrier creation, dynamics and control is required before fully quantitative extrapolations from present devices can be made for ITER.

3.4.2. Other improved core confinement regimes without edge radiation

To this class belong the supershot regime in TFTR, the VH-mode in DIII-D, the high-l_i (internal inductance) regime in TFTR and Tore-Supra, the high β_p mode of JT-60U, improved L-modes in JFT-2M, the LHEP (lower hybrid enhanced performance) mode of Tore-Supra, and the PEP (pellet enhanced performance) mode obtained in several machines.

The supershot regime in TFTR [122] is characterized by extremely peaked density and pressure profiles, along with high $T_i \gg T_e$ ($T_i(0) = 45 \, \text{keV}$, $T_e(0) = 14 \, \text{keV}$) and confinement enhancements of up to 3 over L-mode. The supershot regime shows a strong isotope scaling of confinement; in DD versus DT plasmas, τ_E was found to scale as $A_i^{0.85}$ [115]. The single most important controlling parameter for supershot generation is minimizing the particle influx from the wall.

VH-mode operation on DIII-D represents an enhanced confinement regime that is not linked with reversed or weak magnetic shear [157]. Magnetic braking experiments, i.e. experiments where a reduction of the toroidal rotation by an externally applied resonant magnetic field is brought about, suggest that toroidal flow shear is important for enhanced core confinement in these cases [158].

The high-l_i and LHEP regimes on Tore-Supra [159] are both characterized by an enhancement factor for the electron energy content of up to 1.7 over the Tore-Supra L-mode scaling. LHEP discharges up to 2 min in duration have been obtained in Tore-Supra with the lower hybrid current drive [160]. The formation of transport barriers and a reduction of electron thermal diffusivity coefficients to near neoclassical values have been observed in the plasma core, where the magnetic shear is weak or negative.

DT plasmas with increased plasma inductance have been produced in TFTR [161] by expanding the plasma minor radius during the current rise in the startup phase. These plasmas show an enhanced stability due to an increase in the maximum possible β_N, proportional to l_i, and stay in the L-mode, unlike the high-l_i discharges obtained by a current ramp down. The l_i values up to 2, corresponding to β_N values of up to 3, and pressure peaking factors from 3 to 6.2 have been observed.

In JT-60U, improved L-mode confinement has been observed in deuterium high-β_p discharges at low density with centrally peaked beam deposition [162]. Boronization is essential to get a low density target plasma and sawtooth activity, and locked modes are suppressed by careful control of the internal inductance and the toroidal rotation. It is obtained at values for the cylindrical equivalent safety factor q^* between 4 and 11, and is characterized by

(i) confinement improvement over the L-mode by a factor of about 3, increasing linearly with $\varepsilon\beta_p$ up to about 0.5;

(ii) bootstrap current fractions of about 60%;

(iii) high central temperatures ($T_i(0) > 40\,\text{keV}$, $T_e(0) > 10\,\text{keV}$, $T_i(0)/T_e(0) \sim 4\text{--}5$); and

(iv) high fusion neutron rates.

It is further characterized by a highly peaked T_i and n_e profile, a broad T_e profile, and a relatively broad current density profile, with $l_i < 1.2$, where the weak shear develops in response to the generation of bootstrap current [163]. The existence of an ITB is deduced from the shape of the ion temperature and toroidal rotation profile [164]. This regime is terminated by β collapse due to ideal low-n kink ballooning modes. The β collapse can be avoided through the beneficial effects of an H-mode pedestal and pressure profile broadening [165], and through increased plasma triangularity [166]. As contrasted with reverse shear operation on JT-60U, nearly steady state operation of these plasmas has been demonstrated [8].

In JFT-2M, the improved L-mode is transiently obtained just after an H–L transition [167]. The other improved L-mode is transiently obtained with counter neutral beam injection associated with a peaking of the electron density.

A transient increase in confinement has been found in L-mode discharges in several machines using pellet injection in ohmic and additionally heated discharges (PEP mode) [168–170]. A strong peaking of the electron density and temperature profiles is observed, together with reduced core ($r/a < 0.5$) transport and a reduction in χ_{eff}. Enhancement factors versus L-mode scaling of up to 1.6 have been observed, deteriorating with increasing heating powers.

Improved L-mode without additional impurity radiation occurs in ASDEX-Upgrade when the H-mode power threshold is high. The high H-mode threshold can be obtained by (i) directing the ion ∇B drift [171] away from the X-point, (ii) by H^0 injection, or a combination of both. Power degradation is weaker than that of the usual L-mode scaling and confinement approaches that of the H-mode with increasing heating powers, as shown in Fig. 2, independent of how the high threshold was obtained. An isotopic dependence of confinement has been observed proportional to $A_i^{0.5}$.
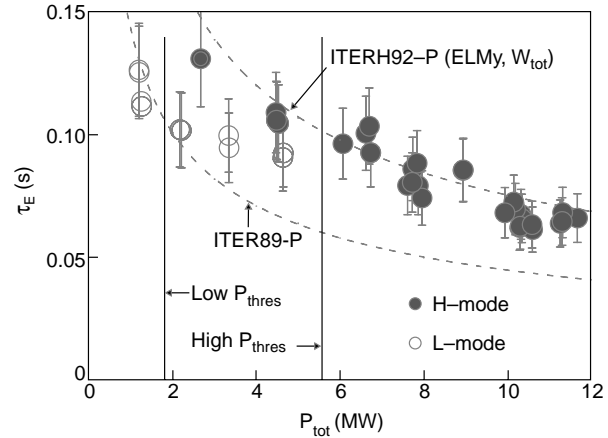

Figure 2. Confinement time versus total heating power in ASDEX-Upgrade: pure deuterium plasmas, both ion ∇B drift directions, $I_p = 1$ MA, $B_T = \pm 2.5$ T.

3.5. Enhanced confinement with edge radiation

Included in this class are the RI-mode of TEXTOR-94 [172–174], the improved L-mode regime of ASDEX-Upgrade [175] and the IL-mode [176] and RI-mode like regimes of DIII-D [177–179]. All these modes are characterized by strong radiation in the edge caused by edge impurity seeding.

The RI-mode on TEXTOR-94 has been obtained in deuterium discharges heated by neutral beam deuterium co-injection (NBI-co) alone or in combination with ICRH and/or counter injection. The RI-mode can be obtained with Ne, Ar, Si and Si + Ne seeding, and has been observed (i) with $P_{NBI-co}/P_{tot} \geq 25\%$; (ii) at sufficiently large densities such that the Greenwald number $\bar{n}_e/n_{GR} \geq 70\%$ (where $n_{GR} = I_p/(\pi a^2)$ with units 10^{20} m^{-3}, MA, m); and (iii) with impurity seeding such that the radiated power fraction, $\gamma = P_{rad}/P_{tot}$, exceeds about 50%.

The RI-mode combines simultaneously many attractive features that are promising for application to a future fusion reactor:

(i) high confinement as good as ELM free H-mode;

(ii) high plasma β, up to $\beta_N = 2.1$ with simultaneous values for product $\beta_N \times H_{89P}$ up to 4.5;

(iii) high density, presently observed from 0.75 up to 1.2 times the Greenwald density;

(iv) confinement increasing linearly with density given by $\tau_{RI} = (\bar{n}_e/n_{GR})\tau_{ITERH93-P}$, both for Ne and Ar seeding, as illustrated in Fig. 3 (here $\tau_{ITERH93-P}$ is the energy confinement time predicted by ITERH93-P scaling for ELM free H-mode [180]);

(v) long and quasi-stationary pulses up to 160 times the energy confinement time, which is very close to the ratio of the burn time to the confinement time foreseen for ITER, or about the skin resistive time without impurity accumulation (versus time) in the centre of the discharge;

(vi) no difficulty with operation at low q_a (checked presently down to $q_a = 2.7$) leading to values for the figure of merit for ignition margin up to $H_{89P}/q_a = 0.8$;

(vii) promising heat removal capabilities by edge radiation with a radiated power fraction up to 0.95;

(viii) no ELMs, no power threshold observed so far; and

(ix) concentration of the seeded impurity sufficiently low such that the neutron yield is not decreasing with respect to discharges without neon seeding.

Injecting pellets into RI-mode shots can lead to a further quasi-stationary increase in confinement [181]. At the highest currents explored up to now ($I_p = 520$ kA), where the highest densities can be reached, central Z_{eff} values around 2 are observed.

The extrapolation of this regime to a future fusion reactor has to be assessed experimentally in order to gain more knowledge on the influence of larger machine size and different plasma parameters on the transport of the energy and particles (D, T and impurities). First encouraging results with Ne and Ar seeding in deuterium discharges have been obtained recently on TFTR [182], Tore-Supra and DIII-D [183, 184].

ASDEX-Upgrade has obtained improved confinement in L-mode discharges by Ne impurity seeding, studied in D^+ or H^+ plasmas heated with D^0 and
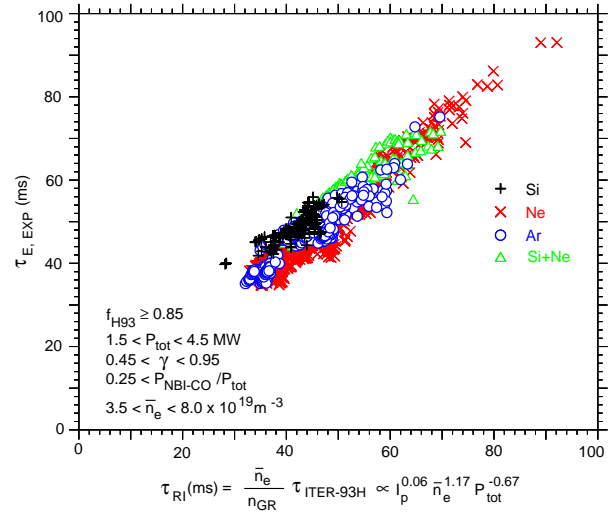

Figure 3. Comparison between the experimentally observed confinement times and the predictions of the RI-mode scaling law $\tau_{RI} = (\bar{n}_e/n_{GR})\tau_{ITERH93-P} \propto I^{0.06}n_e^{1.17}P_{tot}^{-0.67}$ for Ne, Ar, Si and Si+Ne seeded RI-mode discharges in TEXTOR-94.

H^0 NBI respectively, at power levels between 1 and 10 MW and q_{95} between 3 and 4. The confinement increases with radiated power and, at high radiation powers, reaches 80% of that of the H-mode [175].

The IL-mode of DIII-D has been obtained with Ne seeding in both single null and double null configurations after an H–L transition. Confinement of the IL-mode is between 1.4 and 1.8 times L-mode. Both electron and ion thermal transport is reduced, with a doubling of the central electron temperature. The IL-mode can make a transition to the H-mode, and a confinement has been observed in this subsequent H-mode phase by a factor of 3 higher than that in L-mode.

Recently, enhanced confinement with impurity seeding has been observed in DIII-D in both ELMing H- and L-mode deuterium plasmas in diverted and limited configurations. Both Ne and Ar have been used as radiating impurity and all plasmas were heated with NB co-injection. A variety of confinement modes have been observed ranging from L-mode to H-mode and even VH-mode. The results obtained so far in the parameter range $1.2 < I_p < 1.4$ MA, $1.5 < B_t < 2.05$ T, $3 < q_a < 4.5$, $4.5 < P_{add} < 13.4$ MW, $\bar{n}_e/n_{GR} \leq 1$, can be summarized as follows.

(i) In inner limiter plasmas the elongation was $\kappa = 1.4$–1.6; maximum values obtained for the Greenwald number and the radiated power fraction are $\bar{n}_e/n_{GR} \approx 80\%$ and $\gamma = P_{rad}/P_{tot} \approx 80\%$. At the

highest densities, values of the energy confinement time between those characteristic for ELMing and ELM free H-mode were observed with moderately peaked density profiles.

(ii) In a divertor configuration, the H-mode plasmas with $\bar{n}_e/n_{GR} \approx$ 70–80%, radiation fractions $P_{rad}/P_{tot} \approx$ 95% and a confinement characterized by $f_{L89} \geq 1.6$, equivalent to $f_{H93} \geq 1$ (i.e. better than ELM free H-mode confinement) was observed. A promising scenario leading to quasi-stationary conditions is the so-called 'puff and pump' scenario with impurity seeding [179]. Under those conditions, phases have been obtained with a duration of about 3.5 s or $30 \times \tau_E$, β_N values up to 2.3 and $\beta_N \times f_{L89}$ product up to 4.5.

(iii) In addition, the VH-mode was observed in upper single null plasmas at high target densities and radiation levels. A value of $\beta_N \times f_{L89} = 6$ has been obtained for up to 1.6 s, and for nearly the entire period β_N stayed at the stability limit ($\approx 4 \times l_i$). In transient phases, confinement improved to values $f_{L89} = 4$ equivalent to $f_{H93} = 2$, at densities up to $\bar{n}_e/n_{GR} \approx$ 60% and radiation fractions $P_{rad}/P_{tot} \approx$ 50%. In these high performance discharges, it was difficult to increase the radiation further by impurity seeding, possibly due to the very high gradient of the density profile at the edge, leading to radiating mantles with a limited radial extent.

Like the TEXTOR RI-mode, these regimes need further studies before extrapolation to ITER can be made.

4. L–H and H–L transition physics

The H-mode of confinement is one of the most robust and reactor compatible of the improved tokamak confinement regimes, combining good energy confinement [185] with high beta [186] and, in the presence of ELMs, with acceptable particle transport rates for the control of density, impurity and helium exhaust [128, 187]. In addition to its practical importance, the attempt to explain the turbulence reduction and confinement improvement that occur in H-mode have led to fundamental insights into plasma physics.

The H-mode, first discovered in ASDEX [120], has been obtained in all divertor tokamaks that have operated since 1982, in limiter discharges in several tokamaks [188–192], in a current free stellarator [193–195], in a heliotron/torsatron [196, 197], and in a linear tandem mirror machine [198]. H-mode

has also been produced with a wide variety of techniques: heating with neutral beam injection; electron cyclotron heating [193–195, 199, 200]; ion cyclotron heating [188, 201]; lower hybrid heating [202]; and Ohmic heating [203–206]. Furthermore, H-mode has also been produced by biasing the plasma using an external electrode [207, 208] or by biasing the limiter [198].

There is a set of common features that are seen in all devices that obtain H-mode. The first to be identified was the formation of a transport barrier at the plasma edge [209] where the density and temperature gradients steepen after the transition. The formation of this barrier is associated with a drop in the D_α radiation all around the plasma, indicating a significant decrease in the particle outflux. In addition, later work showed that the density fluctuation amplitude decreases in the region where the transport barrier forms [210–212]. A reduction in the amplitude of magnetic fluctuations has also been observed [213, 214]. Finally, at the same time as the formation of the transport barrier and the reduction in fluctuations, a steep gradient region develops in the radial electric field E_r at the plasma edge [215–219]. These features have been seen in all tokamak discharges where diagnostics capabilities allow [220, 221] and have also been seen in the stellarator and mirror results [195, 198].

4.1. Physical processes of transition

Because the H-mode confinement improvement appears in many configurations and has been produced by many means, an understanding of the confinement improvement requires some universal mechanism. The leading hypothesis to date involves the reduction of turbulent transport by sheared $\boldsymbol{E} \times \boldsymbol{B}$ flow [14, 222, 223]. The fundamental idea is that the sheared flow tears apart the turbulent eddies in the plasma, reducing their radial extent and, hence, reducing the transport that they cause. Both a nonzero first radial derivative [14, 222, 223] or second radial derivative [224, 225] of the $\boldsymbol{E} \times \boldsymbol{B}$ flow can reduce transport. Because the shear in the $\boldsymbol{E} \times \boldsymbol{B}$ flow can have the same effect on a wide variety of turbulence, this mechanism has the universality needed to explain the transport decrease in a wide range of conditions. This same sort of shear decorrelation by $\boldsymbol{E} \times \boldsymbol{B}$ flows has also been seen in the edge of ohmically heated limiter discharges in TEXT [226]. It has further been seen on the open field lines beyond the separatrix in diverted plasmas [227] when a sheared

electric field is created with divertor bias.

Decorrelation of turbulence by sheared flows is a mechanism that also functions in ordinary fluids [228, 229]. However, because the sheared flow is also a source of free energy, which can drive Kelvin–Helmholtz instabilities, situations in which net reduction of turbulence occurs are infrequent. In magnetized plasmas, the stabilization of Kelvin–Helmholtz instabilities by shear in the magnetic field allows the flow shear decorrelation to produce a net turbulent transport reduction [14]. Accordingly, this explanation of the H-mode confinement improvement has led to a fundamental contribution to the understanding of the physics of fluids.

A full understanding of the L–H transition requires an understanding of the physics that controls the radial profile and magnitude of E_r that is governed by the radial force balance equation for ions

$$E_r + V_p B_T - V_T B_p = -(Z_i n_i e)^{-1} dp_i/dr. \qquad (9)$$

There has been a large theoretical effort devoted to this issue, which has led to the formulation of equations to describe E_r near the plasma boundary in toroidal geometry with neoclassical and anomalous effects included [230–233]. The experimental assessment of theory is very difficult due to the fact that many of the quantities of interest cannot be measured with the existing diagnostic capability. The ideas that are being actively pursued can be divided into four categories as follows.

(1) *Ion orbit loss* [222, 223, 234, 235]. Ions are preferentially lost from the plasma edge because ions in the loss cone intersect material surfaces. Thus, the plasma is charged up negatively. Alternatively, one can see this as causing a torque generating poloidal flow in competition with the damping due to neoclassical parallel viscosity and charge exchange processes [236, 237].

(2) *Stringer spin up* [238–240]. A large poloidally asymmetric sink or source of particles overcomes the natural damping of poloidal rotation and allows a large poloidal rotation to develop. The relationship between poloidal rotation and E_r has not been specified in this model.

(3) *Pressure gradient drive* [241–243]. A toroidal equilibrium naturally develops a negative radial electric field to balance the ion pressure gradient. Thus, the large and negative E_r is, effectively, a consequence of good confinement.

(4) *Anomalous viscosity* [221, 222, 230, 244, 245] *or turbulent Reynolds stress* [199, 233, 246–251]. Transport of momentum can modify the average flow profile of the plasma. The relation between plasma velocity and E_r has been specified for these models.

Although we have a model of turbulence stabilization and confinement improvement due to $\boldsymbol{E} \times \boldsymbol{B}$ shear stabilization, we still need to validate a model that can predict the E_r value under given conditions. Considerable experimental effort is being devoted to this area, but quantitative tests of the various models require, in many cases, development of novel diagnostics. In addition, since there is no fundamental understanding of energy and particle transport in the plasma edge, even if we had such a model for E_r, we could not predict the edge plasma conditions in ITER with sufficient certainty to utilize it. Furthermore, some models [236, 237, 248] are dependent on, or modified by, the presence of neutrals, which can be affected by details of the magnetic configuration. Accordingly, as is discussed in Section 2.4.3, estimation of the power threshold for ITER is being done empirically. Nevertheless, the L–H transition is an edge phenomena, and the transition conditions should be expressible in terms of edge parameters rather than global ones like heating power. Empirical relations of this type are emerging (as discussed in Section 4.3 and in Chapter 4, Sections 3.7 and 3.8) and will help to provide experimental tests of theory.

4.2. Edge pedestal

A defining feature of the H-mode is the existence of a transport barrier near the plasma boundary. Although the H-mode edge transport barrier can be quite narrow (2% of the minor radius in DIII-D), the characteristics of this layer are significant in the overall plasma performance and in divertor effects.

Stiff ITG-mode turbulent transport models [75, 243] predict that the core temperature is strongly linked to the edge temperature, suggesting that ITER may require relatively high edge temperature for ignition. This result is in qualitative agreement with data from DIII-D [252] and C-MOD [253]. On DIII-D, $H_{H93} \propto (T_e^{PED})^{0.55}(n_e^{PED})^{0.58}/B_T^{0.93}$, where H_{H93} is the energy confinement enhancement factor relative to the ITER93H-P scaling [180], and PED refers to values at the top of the H-mode pedestal (see Fig. 4 and [252]). ASDEX-Upgrade also shows a direct relation between stored energy and pedestal pressure gradient (Fig. 5) [254].
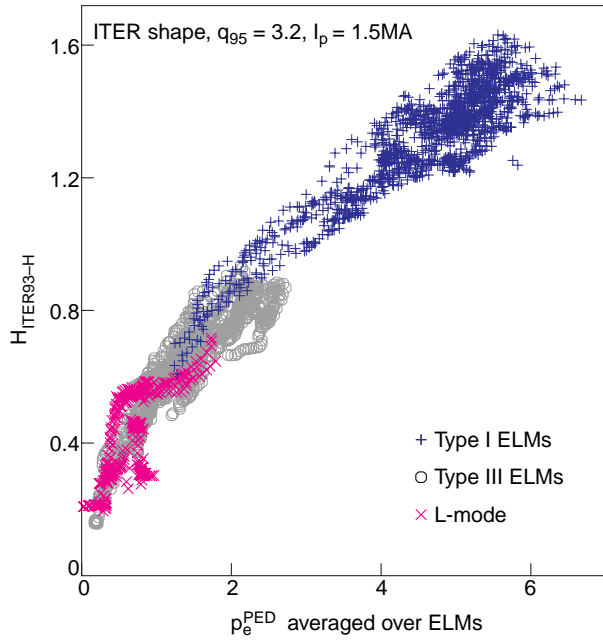
Figure 4. H-mode energy confinement enhancement factor relative to ITER93 H-mode scaling increases with increasing H-mode pedestal pressure (kPa) averaged over ELMs in DIII-D [252].
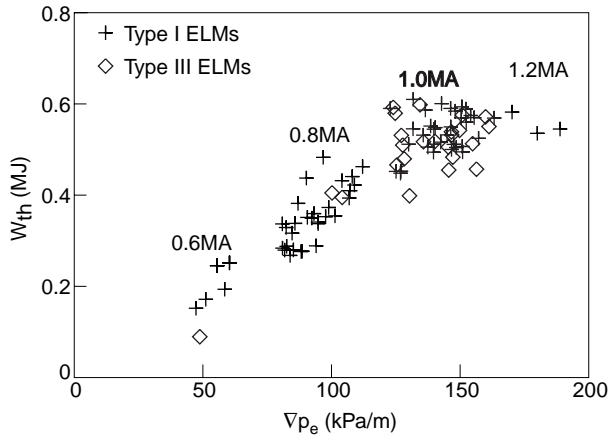

Figure 5. Relation between thermal stored energy and edge electron pressure gradient for discharges in ASDEX-Upgrade near the ideal ballooning limit at the edge [254].

The study of the H-mode pedestal parameters can be separated into the analysis of the scaling of the width of the steep pressure gradient region, which is expected to be set by turbulence suppression physics [220], and the magnitude of the edge gradient. The height and width of the H-mode transport barrier depends on the type and level of ELM activity (Chapter 3, Section 2.6, and Chapter 4, Section 3.8; see also Section 5.2 of this Chapter). The

highest values of the electron temperature at the top of the H-mode transport barrier occur just prior to the crash of a type I ELM. The maximum pressure gradient is usually consistent with ideal ballooning mode stability at the edge [255]. However, data from DIII-D shows that the edge gradient can exceed the nominal infinite-n ballooning limit [252] by factors of 2–3. Type III ELMs often, but not always, have lower pedestal pressures and lower confinement (e.g. Fig. 4).

There is considerable variation in the experimental results for the scaling of the pedestal width. Experiments on JT-60U have reported that electron and ion temperature pedestal widths δ scale as $\delta \propto \rho_{pi}$, the poloidal ion Larmor radius, in the ELM free phase [256], and that it is 2–3 times greater in the ELMy phase. Results from JET, in which the pedestal pressure is measured and it is assumed that the steep edge gradient is limited by the ideal MHD high-n ballooning limit [257], imply a scaling $\delta \propto (\rho_{pi}L)^{1/2}$, where L is a macroscopic length. Direct measurements of the width in JET [258] yield different results. In ELM free H-mode, the electron temperature barrier width δ_{Te} is nearly constant at 3–4 cm; between ELMs it is 5–6 cm. A scaling $\delta_{Te} \propto (T_e^{PED})^{-0.16}$ independent of plasma current I, is found, i.e. not correlated with ρ_{pi}. The electron density barrier width $\delta_n \sim \delta_{Te}/2$. During ELM free H-mode, the ion temperature barrier width scales as $\delta_{Ti} \propto T_i^{PED}$ with $\delta_n = \delta_{Ti}$. Recent JET experiments on the isotope scaling indicate that the pedestal height increases strongly with the isotope mass [259]. In ASDEX-Upgrade, the barrier width δ is fairly constant ($\delta \sim 2$–2.5 cm) and is independent of I, again implying it is not related to ρ_{pi} [254]. Experiments on DIII-D with parameters chosen to be similar to ITER indicate that δ can be fit with two forms, $\delta/R \propto (\rho_{pi}/R)^{2/3}$ (stronger than the other experiments) or $\delta/R \propto (\beta_p^{PED})^{1/2}$. These results can be used to estimate the edge temperature in ITER by assuming type I ELMs will occur at the same α (the normalized pressure gradient parameter for ideal MHD ballooning modes) as in DIII-D or other experiments at the ITER value of q. Scaling from DIII-D discharges with a strong scaling with ρ_{pi}, $\delta/R \propto (\rho_{pi}/R)^{2/3}$ gives $T^{PED} \propto (LB_T/n_G^3) = 1$ keV for ITER (this scaling also implies $\delta \propto (L/n_G B_T)^{1/2}$, and $p^{PED} \propto (B_T^3/n_G L)^{1/2}$). The form of the scaling more consistent with the other experiments of $\delta/R \propto (\beta_p^{PED})^{1/2}$ gives a significantly higher pedestal temperature $T^{PED} \propto (LB_T/n_G) = 5$ keV for ITER (here $\delta \propto L$, and $p^{PED} \propto B_T^2$). Similar val-

ues ($\sim$4 keV) are obtained from extrapolations from other experiments (Chapter 4, Section 3.8).

4.3. Power threshold scaling

The H-mode is reached above a certain threshold power, P_{thr}, which depends on plasma conditions and machine size, and it is essential to predict what value is needed for ITER. The threshold dependence on plasma configuration and parameters, studied in single devices during the past years [171, 260–268] can be summarized as follows. The threshold power is about 2 times lower for the single null (SN) configuration with the ion ∇B drift towards the X-point, than for the opposite direction or double null (DN) configuration; the threshold is about 2 times lower in deuterium than in hydrogen; reduction of neutral density and impurities by appropriate wall conditioning and good divertor retention is favourable for achieving low threshold powers. The studies in single devices also show a rather clear linear dependence of P_{thr} on $\bar{n}_e$ and B_T. However, the size dependence, an essential element for extrapolation, cannot be deduced from experiments made on single devices. Therefore, since 1992, the ITER H-mode threshold database has been constructed [269] and presently includes 10 divertor tokamaks [270–273]: Alcator C-Mod, ASDEX, ASDEX-Upgrade, COMPASS-D, DIII-D, JET, JFT-2M, JT-60U, PBX-M and TCV. The present version of the database contains about 150 variables, which describe the magnetic configuration, the core and the edge regions of the plasma. The latter is believed to play a major role in transition physics as shown in Section 4.1. Care was taken to include in the database data representing the lower threshold from each device and, in particular, from discharges with good wall conditions. Apart from allowing studies of the size scaling, the database provides a unique framework for systematically comparing threshold data from several tokamaks. The database confirms the earlier results from single devices, in particular the B_T dependence, but also shows differences for the density dependence. The threshold power generally shows a minimum at a density $\bar{n}_{e,min}$ in the range 0.1–0.25×10^{20} m^{-3} (sometimes even exhibiting an apparent density threshold [265]), except for Alcator C-Mod, for which $\bar{n}_{e,min} \approx 0.8 \times 10^{20}$ m^{-3}. The value of $\bar{n}_{e,min}$ is around 20–30% of the Greenwald density limit, but no clear relation could be established so far. Above $\bar{n}_{e,min}$, the power threshold increases linearly with density up to a density around 80% of the Greenwald

density limit. Above this value, the power threshold increases with a strong non-linear dependence [274].

Scaling expressions for P_{thr} are obtained from the database by performing a linear regression of the net heating power $P_l = P_{heat} - dW/dt$ versus $\bar{n}_e$, B_T and machine size and geometry using R, a, S and/or κ (major radius, minor radius, plasma surface area, elongation). The time slices are taken just before the L–H transition, for conditions providing low power threshold: deuterium plasmas, ion ∇B drift toward X-point. Previous results were presented in [269–273]. More recent analyses from the last version of the database (ITERTH DB2.3, September 1997) are given in Table 2. Results show that the root mean squared error (RMSE) is significantly reduced when the size regressors R and a (expression 2) or S (expression 3) are used, instead of R only.

Using κ as an additional regressor does not modify the results significantly. Moreover, the κ dependence is not well assessed because it is only provided by the fact that ASDEX has a circular cross-section, whereas all the other tokamaks are elongated with $1.3 \le \kappa \le 1.7$.

Further analyses show that two groups of tokamaks can be distinguished: ASDEX-Upgrade, Alcator C-Mod, DIII-D, JFT-2M, JT-60U, JET, PBX-M on one hand, ASDEX, COMPASS-D and TCV on the other hand. Making a regression with data from the first group yields expressions 4 and 5, which have a low RMSE and are represented in Figs 6 and 7. The seven tokamaks of this group agree with the fit within one standard deviation. The three tokamaks of the second group are on a line parallel to that of expression 4 but higher by 60% (Fig. 6). For COMPASS-D and TCV, the reason for this effect may be attributed to the small size of the devices in which the influence of neutrals is expected to become important. For ASDEX, it may be attributed in addition to the circular cross-section. When expression 5 is considered (Fig. 7), only COMPASS-D and TCV are above the line defined by the other seven tokamaks, whereas ASDEX agrees with this fit.

At present, there is no strong reason allowing a decisive conclusion to be drawn from Table 2 or Figs 6 and 7. The values given here represent the extrapolation uncertainties of the H-mode threshold power in ITER based on the present database. Expressions 4 and 5 of Table 2 are conservative, take into account plasma geometry as complete as can be obtained from the database, and have a good RMSE. For these reasons they might be recommended for extrapolation to future devices.

Table 2. Summary of the threshold analyses with global parameters

Eq.	Excluded tokamaks	Obs.	Num. factor	$n_{e,20}$	B_T	R	a	S	RMSE %	Low 95% MW	ITER pred. MW	Up 95% MW	Constr. eq.
(1)	none	512	0.70	0.94	0.80	2.12			30.5	67	124	230	3.04
(2)	none	512	1.79	0.78	0.76	1.14	0.78		28.3	53	95	169	2.36
(3)	none	512	0.057	0.64	0.83			0.89	28.8	49	88	157	2.15
(4)	ASDEX, TCV COMPASS-D	432	0.041	0.69	0.91			0.96	25.2	70	116	192	2.39
(5)	ASDEX, TCV COMPASS-D	432	1.38	0.77	0.92	1.30	0.76		25.1	79	132	224	2.54

The columns from left to right indicate: the expression numbering, the tokamaks not included in the regression, the number of time slices included in the analysis, the numerical factor, the exponents of density, magnetic field, major and minor radius, plasma surface area, RMSE of the regression, the lower values of the 95% confidence interval (usual definition) of the ITER prediction, the threshold power predicted for ITER, the upper 95% confidence interval, the results of the sum determined by constraint with dimensionless parameters (see later in the text). The units used are m^{-3}, T, m, m^2, MW.
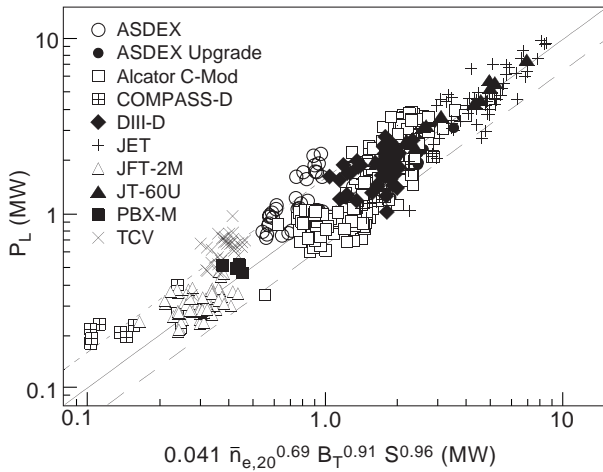

Figure 6. Comparison of experimental power thresholds with the scaling expression 4 (solid line). The dashed line is expression 4 multiplied by 0.66, and the dotted line, which fits ASDEX, COMPASS-D and TCV data, is 60% above expression 4.

Figure 7. Comparison of experimental power thresholds with the scaling expression 5, same meaning of lines as in Fig. 6.

The H-mode being determined by conditions at the plasma edge, the power flux across the edge, $P_L = P_{heat} - dW/dt - P_{rad}^{core}$, is a global parameter better suited to describe the power threshold. The radiation inside the separatrix, P_{rad}^{core}, can be subtracted only for some of the analyses because of the limited data available. This excludes devices, increases the RMSE of the regression [272,273] and is not taken into account here. Further data and work are necessary to obtained a reliable result.

To analyse the database one may also be guided by the observation that, for fixed values of the con-

trollable plasma parameters, the H-mode transition occurs at the plasma edge and that a minimum power flux across the separatrix is required. Starting from this assumption, using the usual dimensionless plasma variables, ν^*, ρ^*, β and assuming that a power law expression for the threshold power, $P_{thr} = \bar{n}_e^X B_T^Y R^Z$, satisfies the high-$\beta$ (Kadomtsev) constraint, one obtains the following relation between the exponents: $8X + 5Y - 4Z = 3$ [270,271]. This approach implies that the L–H transition is only governed by plasma physics parameters, which is not necessarily the case at the plasma edge where atomic physics might also play a role. The exponents of the variables in the scaling expres-

sions (2)–(5) in Table 2 yield values for $8X + 5Y - 4Z$ between 2.15 and 2.54, as indicated in Table 2, therefore approaching, but not quite meeting, the condition derived with dimensionless variables.

Under the assumption of a linear B_T dependence ($Y = 1$) as observed in all the tokamaks, $P_{thr} = CB_T\bar{n}_e^{0.75}R^2$ is dimensionally correct and in rough agreement with the experimental observation within the uncertainties. The uncertainties can be formulated by the quantity $(\bar{n}_e R^2)^\alpha$, where α is determined from the analysis of the database. This leads to the following expression (10), given in [271], where the reader can find a complete derivation:

$$P_{thr} = C(R/a, \kappa, q, \alpha)B_T\bar{n}_e^{0.75}R^2(\bar{n}_e R^2)^\alpha \quad (10)$$

where C is a non-dimensional coefficient. Using the database version ITERTH DB2.1 (September 1996), one finds: $-0.25 \leq a \leq 0.25$ and $C = (0.45 \pm 0.1) \times 0.6^\alpha$. The range in α is obtained by analysing the data scattering of the database while varying the density exponent X in the Kadomtsev constraint, $8X + 5Y - 4Z = 3$, and maintaining $Y = 1$, as explained in [271]. Expression (10) leads to a range for the threshold power prediction for ITER between ~ 50 MW and ~ 200 MW. The uncertainty is dominated by the R dependence, $R^{1.5}$–$R^{2.5}$. Since this work was performed, efforts have been made to reduce the scattering of the data, and are expected to somewhat reduce the uncertainties of future results.

The power threshold in ITER predicted by the database at present has a considerable uncertainty (from ~ 50 MW to ~ 200 MW) and the upper value exceeds the currently planned heating power. The high required power and the large range of the uncertainty are due mainly to the exponent on the size dependence, which is close to 2 in all the cases. It must be stressed here that, extrapolating from JET and JT-60U to ITER, the size dependence is the major contribution compared to those from $\bar{n}_e$ and B_T. For the extrapolation to ITER, one assumes that the conditions for a low threshold, as required in present tokamaks and listed above, will be fulfilled. This will, most probably, be the case: a SN configuration with favourable ion ∇B drift is foreseen in ITER, high divertor retention and low recycling wall conditions will provide low neutral density. The expressions given in Table 2 are obtained by a free fit through the standard dataset. According to present knowledge, effects causing a particularly high threshold in ITER are not expected. On the contrary, one may expect the threshold power in ITER to be kept low for the two following rea-

sons. First, if one assumes that the above conditions that provided the lowest threshold values in present tokamaks can be achieved in ITER, one may reduce the numerical factor of expressions 4 and 5 such that the corresponding line goes through the lower point boundary, as suggested by the dashed line in Figs 6 and 7. This decreases the threshold prediction for ITER by about 30%. Second, as was mentioned above, the power threshold is lower in deuterium than in hydrogen. Very recent experiments in JET with tritium indicate a $\sim 25\%$ decrease of the power threshold in DT (50%–50%) plasmas [275]. These results yield a power threshold that is inversely proportional to the effective plasma mass. This might also lower the power threshold in ITER by about 25% in DT operation. It may even be valuable to first reach the H-mode in pure tritium to take advantage of the lower threshold and then add the necessary deuterium. In several devices a power hysteresis has been observed for the H-mode threshold: about 1.5–2 times more power is required to achieve the H-mode than to sustain it. However, the hysteresis is not observed in JET [276] and it disappears when the density is increased towards the density limit, as shown in ASDEX-Upgrade [274]. The latter effect is attributed to confinement degradation observed at high density [277]. Therefore, one cannot rely on the hysteresis for ITER prediction in the present status of understanding, and further investigations are necessary on this topic.

A more precise assessment of the ITER threshold power demands further understanding and quantification of the influence of plasma geometry, edge parameters and neutrals on the threshold, as well as a reduction of the data scatter for each tokamak. Such studies are being actively pursued in several tokamaks and in the framework of the database activity. The understanding of the effect of neutrals is still controversial, in particular for the region around the X-point. For the rest of the main plasma it is clear that smaller devices and low density cases are sensitive to viscous damping of rotation by neutrals, whereas in larger devices at high density, neutrals only affect the very edge of the plasma, and possibly do not reach the region where the L–H transition happens. Significant progress has been made on threshold studies with edge data and their comparison with theory (see the Sections above). It appears in several devices that the edge electron temperature at the L–H transition consistently depends linearly on B_T, seems to increase with I_p^γ, with $0.5 \leq \gamma \leq 1$, and depends only weakly on $\bar{n}_e$. Note that these

dependences are in agreement with the global scaling presented above, even for I_p and $\bar{n}_e$, as demonstrated by the following explanation. The required edge temperature depends on heating power and edge transport. Therefore, the higher edge temperature necessary at higher I_p is provided, at least partly, by the increase of confinement with I_p (L-mode confinement). Thus, P_{thr} depends weakly on I_p at given B_T and $\bar{n}_e$. Similarly, the weak dependence of the edge temperature on density is consistent with the linear dependence of P_{thr} on $\bar{n}_e$: at higher $\bar{n}_e$, the edge density is also higher and more power is required to sustain the same edge temperature for given I_p and B_T.

However, the large scatter of the edge data presently available in the threshold database prevents one from making a meaningful prediction for ITER; this still requires additional work. It is also to be underlined that a prediction of the required edge values to achieve the L–H transition in ITER will be of practical significance only if one is also able to predict the associated heating power. For this purpose, reliable transport modelling will be necessary.

5. Impact of global instabilities on transport

A number of large scale MHD phenomena, described more fully in Chapter 3, Section 2, can have an impact on global confinement. Two of these are the periodic sawtooth instability, which can have a significant effect on the profiles of temperature, density and impurities in the central core region, and the ELMs, which periodically affect the plasma edge region. These are discussed more fully in Sections 5.1 and 5.2, respectively. A third candidate is the transport induced by low-m, n magnetic islands, where m and n are poloidal and toroidal mode numbers; such an island is located at the resonant surface r_s where $m = nq(r_s)$, q being the safety factor. Because the temperature is rapidly equilibrated along the reconnected magnetic field lines within islands, they effectively short-circuit the normal transport across nested toroidal magnetic surfaces, decreasing the effective size of the plasma. An expression for the deterioration in plasma energy δW arising from the presence of an island of width w located at a rational surface r_s in a plasma of minor radius a is [278, 279]

$$\frac{\delta W}{W} = \frac{20}{3}\left(1 - \frac{r_s^2}{a^2}\right)\left[1 - \left(1 - \frac{r_s^2}{a^2}\right)^3\right]\frac{r_s}{a}\frac{w}{a}$$

where W is a stored energy without the magnetic island. These magnetic islands can arise from tearing modes, possibly of a neoclassical origin (Chapter 3, Sections 2.2 and 2.3). They will, therefore, tend to occur near operational limits, e.g. low q, or higher β_N (the normalized β); in particular, they could lead to an onset of confinement degradation when $\beta_N > 2$. The transport effects of low-m, n modes have been observed in TFTR supershots [279].

5.1. Sawteeth

When the central value of the safety factor q falls below unity, relaxation oscillations are normally observed in the core of a tokamak plasma. These appear on a number of plasma parameters but are particularly evident in the central electron temperature $T_e(0)$ [280]. The oscillations in $T_e(0)$ exhibit a time trace with a distinctive sawtooth shape consisting of a slow rise or 'ramp' phase, during which the plasma inside $q = 1$ heats up, followed by a rapid collapse or 'crash' when the plasma energy is redistributed from the core to the region outside $q = 1$, i.e. over a region within the so-called mixing radius r_m. This then propagates as a heat pulse to the plasma periphery. The position where the perturbation in T_e changes sign is known as the inversion radius r_i. This pattern repeats with a period τ_{saw}. This mechanism has the effect of degrading the global energy confinement time τ_E as r_m/a becomes significant, typically for $q_{95} \leq 3$. Experiments on DIII-D (discussed in [281]) show that the increase of H-mode confinement with current saturates for $I_p/B_T \approx 1$ MA$\cdot$T^{-1}, corresponding to $q_{95} \sim 3$, although JET shows no appreciable degradation down to $q_{95} \sim 2.0$ [282]. Varying q_{95} in DIII-D by means of scan over elongation κ shows that it is not q_{95} that determines the confinement degradation due to sawteeth. Rather, experiments on DIII-D and JET indicate that this degradation increases with r_m/a. JT-60U has demonstrated a deterioration in confinement as the sawtooth period τ_{saw} decreases [283, 284]. Chang and Callen [278] have proposed a model for the sawtooth degradation factor f_{saw} depending on A_m, the relative area of sawtooth mixing, and $x = \tau_{saw}/\tau_E$. For a constant thermal diffusivity and central heating, this takes the form

$$f_{saw} = (1 - A_m)g(x) + 1 - g(x)$$

with

$$g(x) = (1 - e^{-x})/x.$$

Sawteeth have an effect on the plasma density and also the distribution of impurities. There is evidence that some plasma density is removed from the saw-toothing region, leading to an outwardly propagating density pulse. However, the effect is less than in the case of temperature; for example, the density profile in the core becomes somewhat less peaked, rather than flat, in the TEXT tokamak [285]. The impact on impurities is more significant. The sawtooth can both effectively purge accumulated core impurities and allow impurities diffusing inwards to rapidly penetrate the region inside $q = 1$. Reference [286] provides a source of references on the experimental evidence for this. In particular ASDEX-Upgrade, operating in the CDH (completely detached H-mode), demonstrates a density peaking, improved confinement and impurity accumulation when sawteeth are absent [287].

Because the thermonuclear power depends non-linearly on plasma pressure p ($P_{fus} \propto p^2$), the redistribution of plasma energy due to sawteeth would cause a periodic overall power loss in an ignited tokamak. If the scale-length for the central pressure is r_p so that $p = p_0(1 - r^2/r_p^2)$, the fractional loss of power at a sawtooth collapse would be $\sim \frac{1}{2}(r_i/r_p)^6$. This would typically imply a power loss of tens of MW. Thermal pulses from the sawtooth collapse could lead to undesirable transient heat loads on divertor plates when the mixing radius is large. A large sawtooth crash could excite other MHD phenomenon, e.g. ELMs or neoclassical tearing modes.

The sawtooth phenomenon is believed to be associated with an instability having an $m = n = 1$ structure, which arises when a $q = 1$ surface is present. The q profile also oscillates with a sawtooth behaviour, falling during the ramp as the central current density increases with increasing T_e, and rising sharply at the crash, typically by a few per cent. Measurements of the central q vary; typically $q_0 \sim 0.7$ is observed [288], but there are cases with $q_0 \sim 1$ reported.

Kadomtsev proposed a resistive MHD model to explain early observations of sawtooth behaviour. During the ramp phase, as $T_e(0)$ heats up and q_0 falls, a magnetic island begins to grow at the $q = 1$ surface as the result of an $m = n = 1$ instability. The resulting magnetic reconnection occurs on a crash time-scale $\tau_c \sim (\tau_R\tau_A)^{1/2}$ where τ_R is the resistive diffusion time and τ_A the Alfvén time. As a consequence, there is a redistribution of poloidal magnetic flux that terminates when $q > 1$ everywhere. Associated with this there is a similar redistribution of

energy leading to a flattening of the n and T_e profiles out to the mixing radius $r_m \sim \sqrt{2}r(q = 1)$ [289].

However, later experiments exposed a number of weaknesses in this model:

(i) it is unclear why the instability does not grow throughout the period when $q < 1$;

(ii) the event that triggers the onset of the crash and sets the period τ_{saw} of the sawteeth is a mystery;

(iii) the time-scales for the crash in larger, hotter tokamaks are much shorter than predicted by this resistive model; and

(iv) the small changes in q_0 arising from resistive diffusion are incompatible with $q_0 \sim 0.7$, suggesting that the very centre does not undergo magnetic reconnection; on the other hand, T_e is flattened throughout the core region.

All these topics are areas of active research and possible explanations have been proposed.

Nevertheless, the Kadomtsev description offers a basis for incorporating the effects of sawteeth in transport codes. The basic features of such a model for the effect of the sawtooth are as follows. When q_0 falls below unity (or some other critical value, say 0.7), a repetitive flattening of T_e and T_i (and possibly n) over a specified region $r < r_m$ is performed each sawtooth period τ_{saw}. Both r_m and τ_{saw} can be regarded as parameters to be explored, though prescriptions like $r_m \sim \sqrt{2}r(q = 1)$ and determining τ_{saw} from kinetic stabilization criteria for the $m = n = 1$ mode have been invoked [290]. More complex prescriptions have been proposed to explain why q_0 remains well below unity [291]. A model for this redistribution of impurities, based on the same ideas as in [291], has been given in [286].

The interaction of sawteeth and energetic particles, arising as fusion products and from RF heating, is another topical research area. While there is conflicting evidence from JET on whether such particles undergo the redistribution experienced by the thermal particles [292], a substantial redistribution of alpha particles has been observed on TFTR, although losses are small [293]. Transport codes for simulating burning plasmas can prescribe an instantaneous loss of alpha heating power at the sawtooth crash to represent a possible loss of alpha particles, which then recovers over an alpha particle slowing down time. On the other hand, there is experimental evidence from JET [294, 295] and TFTR [296] and

theoretical arguments [290, 297] that energetic parti-
cles can stabilize sawteeth for long periods. In such a
case, the tokamak experiences large amplitude 'mon-
ster' sawteeth [294]; these effects can also be incorpo-
rated in modelling codes [290]. The collapse of such
monster sawteeth could have serious implications for
divertor target heat loads.

Advanced tokamaks could possibly achieve
improved performance by stabilizing sawteeth by: (i)
current profile control to maintain $q > 1$; (ii) local
current profile control near $q = 1$; and (iii) energetic
particle stabilization.

5.2. Edge localized modes

The ELM is a relaxation oscillation triggered by
an MHD instability, which leads to a fast (ms)
loss of particles and energy from the plasma edge.
ELM physics has been summarized in recent reviews
[298, 299] and is discussed more fully in Chapter 3,
Section 2.6. From the ITER viewpoint, ELMs are
beneficial because they lead to impurity and helium
ash expulsion from the plasma edge, allowing cleaner
plasmas. However, as is discussed in Chapter 4, Sec-
tions 3.8, 4.2.4 and 6.4, the cost of these benefits is
the need to handle the heat pulses to the divertor
plates produced by the ELMs. Although ELMs do
reduce the global energy confinement by 10–20%, as
will be seen presently, they have a much larger effect
on the particle confinement than on the energy con-
finement. Accordingly, the use of ELMs to control
impurities and helium ash does not impose a large
energy confinement penalty.

There are two major types of ELMs of interest
to ITER. Type I ELMs exhibit a repetition fre-
quency that increases with increasing input power,
while type III ELMs have a repetition frequency that
decreases with increasing input power. In general,
type III ELMs occur when the edge electron temper-
ature is fairly low, while type I ELMs occur at higher
edge electron temperatures [298]. The exact MHD
mode associated with ELMs is, as yet, unknown. The
edge density and temperature parameter range for
the various types of ELMs is illustrated in Fig. 8 for
a case from DIII-D [252]. The type I ELMs appear
to be driven primarily by the edge pressure gra-
dient [255], while the type III ELMs depend both
on the edge density and the edge electron temper-
ature [252, 300] suggesting a role for resistivity or
edge current [264, 298]. As is seen in Fig. 8, there
appear to be two branches for the type III ELMs,
one at low density and one at low temperature. Clear

MHD precursors have been seen for the type I and
type III ELMs, although the precursors for the type I
are much more difficult to detect [301]. In small
machines (e.g. ASDEX), type III ELMs can be seen
even at input power levels adequate to drive the
plasma to the MHD beta limit. In larger machines
(ASDEX-Upgrade, DIII-D, JET), the power needed
to approach the beta limit is sufficient to heat the
edge to the point where type I ELMs occur. Based
on this observation, ELMs in ITER will probably be
type I ELMs, although it may be possible and more
desirable to operate with smaller type III ELMs,
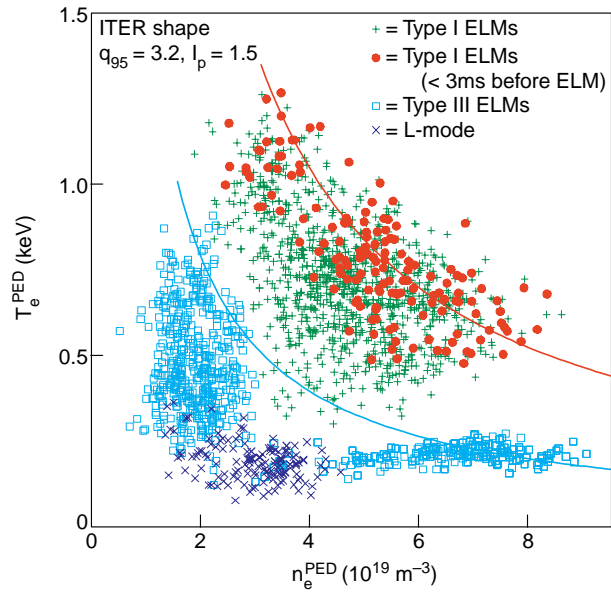which occur if the edge density is sufficiently high.

Figure 8. The edge electron density and temperature
in DIII-D discharges with different types of ELMs [252].

An examination of the global power balance in
type I ELMing H-modes in DIII-D [302] showed that
P_{ELM}, the power lost through ELMs, is less than
20% of the total input power P_T. In DIII-D, this
fraction was found to decrease with increasing P_T
so that the energy loss per ELM, δE, decreased with
P_T, while the ELM frequency ν_{ELM} was proportional
to P_T. Accordingly, P_{ELM} was roughly independent
of P_T over the power range studied [302]. However,
in later work, P_{ELM} was found to be proportional to
P_T [252]. A similar behaviour is found in ASDEX-
Upgrade [303], where δE is independent of P_T and
ν_{ELM} increases with P_T, leading to $P_{ELM}/P_T \sim 25$–
40%. The difference between the two behaviours
may be the longer duration of the ELMs in the
earlier DIII-D study. There, the plasma appears to
transiently return to L-mode after each ELM, with
the duration of the L-mode decreasing with increas-

ing P_T. Above a certain heating power, which will depend on the H-mode threshold power, the duration of the ELM is roughly constant. Thus, the statement that the energy loss per ELM is roughly constant, would be valid only above a certain heating power.

Since type I ELMs can induce a return to L-mode [304], the ITER design must assure that there is sufficient power flow through the plasma edge to allow a return to H-mode after an ELM at the parameters characteristic of the burn phase.

The energy loss due to ELMs causes a reduction of the global energy confinement time τ_E. Studies on DIII-D showed that, in type I ELMing discharges, τ_E is reduced by 10–15% [304,305], although JT-60U shows larger reductions in the presence of higher frequency 'giant ELMs' [283,306]. A more general investigation of the influence of ELMs on τ_E was done by establishing a scaling of τ_E in ELMy H-mode [305]. A comparison with a similar scaling for the ELM free H-mode shows that, for present experiments, the reduction in τ_E is indeed around 10–20%. For larger devices, especially for the ITER parameters, the two scalings agree within the statistical errors. Such a result is expected if ELMs can be considered a surface effect. However, the scaling given in [305] mixes data with type I and type III ELMs with their different power dependences of the repetition frequency. Accordingly, we need better data without this confusion to make a firmer conclusion for ITER. In any case, it appears that the confinement reduction will probably not be larger than 20%.

A different way to estimate the confinement degradation due to ELMs is to quantify the reduction due to ELMs by a factor η, defined by

$$\eta = \tau_E^{ELMy}/\tau_E^{ELM-free}.$$

The precise value of η has to be found by an analysis of the profile effects due to the ELM. Assuming a diffusive process and spatially separated source and sink profiles, which is a reasonable assumption for centrally peaked heating profiles, one can calculate [307]

$$\eta = 1 - [1 - (r_{ELM}/a)^2]P_{ELM}/P_T.$$

Accordingly, due to the localization of the ELMs, the confinement degradation is appreciably lower than the fraction of power transported across the separatrix by ELMs. Typical values from ASDEX-Upgrade are $P_{ELM}/P_T = 0.3$ and $r_{ELM}/a = 0.8$ [308], resulting in $\eta = 0.9$. This agrees reasonably well with the $\eta = 0.85$ result from DIII-D mentioned above. The

scaling of η for future machines critically depends on the scaling of r_{ELM}, which also enters into the scaling of δE and, therefore, P_{ELM}. A model for the loss of energy by ELMs based on transport due to the stochastic magnetic field caused by the ELM precursors has successfully described results from COMPASS-D [309,310] and also ASDEX-Upgrade.

The effect of the ELMs on the particle confinement time is also of major interest. A quantitative analysis of the effect of ELMs on particle confinement time has not yet been given. Experimental results on a number of machines clearly show that the density is constant in ELMy H-mode, while it increases monotonically in ELM free H-mode. In both modes of operation, the total energy content reaches a steady value. These results indicate that ELMs reduce global particle confinement time much more than they reduce τ_E. As was shown in DIII-D, the particle density control in ELMy H-mode also makes removal of helium ash from the plasma possible [128,187].

The difference in the effect of ELMs on particle and energy loss can be due to the different source profiles of energy and particles: as was pointed out in [311], an edge localized loss phenomenon is most severe for a quantity whose source profile is also edge localized, as is the case for particles. For a central source profile, which is mostly the case for plasma heating, the source is not directly affected and the effect on global confinement is less severe. This will be also true for ITER, where the alpha heating profile will be comparable to present day neutral beam heating profiles.

6. Global energy confinement scalings

6.1. Introduction

Due to the complexity of the processes determining heat and particle transport in thermonuclear plasmas, it is not yet possible to provide a first principles derivation of the dependence of energy confinement properties on plasma parameters. The description of the global energy confinement time by empirical scalings that are based on relevant datasets within specific operating regimes such as L-mode or H-mode has, therefore, become the key tool in extrapolating plasma performance to ITER. As well as predicting the performance of a next step device, such as ITER, in terms of its basic design parameters, such scalings can also be used as a normalization for plasma energy in one dimensional simulation

codes, which use various transport models that predict the plasma behaviour in ITER, or as an approximate constraint on the form of theoretical models. When expressed in terms of dimensionless plasma parameters, scaling expressions can also serve as a guide to modellers by emphasizing different types of theory based transport loss mechanisms, for example electrostatic versus electromagnetic loss mechanisms, which differ in their dependence on beta.

The present database activity originated in an international L-mode database, initiated by S. Kaye, in the early eighties, that led to the ITER89-P scaling [136] during the ITER conceptual design activity (CDA) phase. The initial multi-tokamak H-mode confinement database was assembled by an H-mode database working group in 1989, with contributions from six machines (ASDEX, DIII-D, JET, JFT-2M, PBX-M and PDX). Basic documentation and analysis of this dataset can be found in [312].

An extended version of this database [180,313,314] formed the basis of such scaling expressions as ITERH92-P(y) [305] and ITERH93-P scaling [180], describing the global thermal energy confinement time in ELMy and ELM free discharges, respectively. This database included extended plasma parameter ranges for most of the constituent devices, as well as improved estimates of the thermal energy confinement time. It also addressed several detailed issues, such as the combination of different energy measurements (from diamagnetic measurements and MHD equilibrium fits) and the correct B (or q) and κ [314] exponents.

Most recently a new working version of the database has been established ('DB3'), which includes data from additional tokamaks. Details of the new dataset are discussed in Section 6.2 and in [315]. This has necessitated the development of a new set of selection criteria, for example to include RF heated as well as NBI heated plasmas. The subset of ELMy data in the new database has been improved considerably in terms of the uncertainty in projecting to ITER, as is discussed in Section 6.3 and 6.4.

In Section 6.3, by using physical relationships that hold 'on radial average', confinement scaling expressions given in engineering variables (which are directly under the control of the experimentalist or machine designer) are transformed into expressions in dimensionless physical variables, which have a close connection to physical theories, e.g. ρ^* the normalized ion Larmor radius, β the normalized plasma pressure, and ν^* the normalized plasma collisional-

ity [72, 73]. On a logarithmic scale, this corresponds to a linear transformation of the response and regression variables. Within the class of simple power law, or log-linear, models, one then has the same scaling expressed in two different sets of variables [313, 316].

In Section 6.4 the uncertainties associated with these ITER projections are discussed and functional forms other than the simple power law form are touched upon (a more detailed discussion is given in the Appendix).

Issues concerning the impact on confinement of ITER's proximity to operational limits, such as the Greenwald density limit and β limit, are areas for future study as new data near these limits is added to the database. Although difficult to achieve, good H-mode confinement has been obtained above the Greenwald density, for example $n/n_{GW} < 1.5$ with pellet injection in DIII-D [317], indicating that there is no fundamental obstacle to operation in this density regime (see Chapter 3, Section 3; Chapter 4, Sections 3.3, 3.4 and 6.2; and Chapter 9, Section 3.4, for details).

6.2. H-mode global confinement database

The assembly of the latest version of the ITER H-mode confinement database, ITERH.DB3, was completed in September 1997. This version contains data from 12 different tokamaks: ASDEX*, ASDEX-Upgrade, COMPASS-D, JET*, TCV and TEXTOR from Europe; JFT-2M* and JT-60U from Japan; Alcator C-Mod, DIII-D*, PBX-M* and PDX* from the USA (* indicates contributors to the old database ITERH.DB2). All the ITERH.DB2 data are in the new database and a detailed description of these data can be found in [313]. The main characteristics of the new H-mode data specific to ITERH.DB3 are detailed in Table 3.

It should be noted that the number of discharges contributed by some of the new machines is very small. Whereas the data from each of the six contributing tokamaks in ITERH.DB2 included both ELM free and ELMy NBI heated H-mode data, it is apparent from Table 3 that the ELM free subset of ITERH.DB3 does not contain data from all the machines. A second new feature is that no single heating method is employed to obtain H-mode on all devices. As a result, it has been necessary to redefine the selection criteria used to delimit the standard analysis dataset of ITERH.DB2 [313] to avoid excluding some machines from the standard analysis dataset of ITERH.DB3. The new selection criteria,

Table 3. Main characteristics of the new H-mode data specific to the new ITER H-mode confinement database, ITERH.DB3

Alcator C-Mod	ICRF heated ELM free and ELMy data
ASDEX-Upgrade	ICRF and NBI heated type I ELMy data
COMPASS-D	Ohmically heated ELM free and ELMy data ECRF-heated ELMy data
DIII-D	ECRF and NBI heated ELM free and type I ELMy data
JET	ICRF and NBI heated ELM free and type I ELMy data
JT-60U	NBI heated ELMy data
TCV	Ohmically heated ELM free and ELMy data
TEXTOR	ICRF and NBI heated RI-mode data (for comparison with H-mode)

which are comparable to the previous criteria but allowing all heating schemes, are listed in Table 4.

Applying these criteria to ITERH.DB3 results in a standard ELM free H-mode dataset of 1131 observations with contributions from nine tokamaks (Alcator C-Mod, ASDEX, COMPASS-D, DIII-D, JET, JFT-2M, PBX-M, PDX and TCV), and a standard ELMy H-mode dataset of 1398 observations from 11 tokamaks (Alcator C-Mod, ASDEX, ASDEX-Upgrade, COMPASS-D, DIII-D, JET, JFT-2M, JT-60U, PBX-M, PDX and TCV).

6.3. Power law scaling expressions

The power law scaling expressions for thermal energy confinement time, τ_{th}, can be expressed either in 'engineering' variables as

$$\tau_{th}^{fit} = C I^{\alpha_I} B^{\alpha_B} P^{\alpha_P} n^{\alpha_n} M^{\alpha_M} R^{\alpha_R} \varepsilon^{\alpha_\varepsilon} \kappa^{\alpha_\kappa} \qquad (11)$$

or in 'physics' variables as

$$\tau_{th}^{fit} = C_1 \tau_B^{x_{\tau_B}} \rho_*^{x_{\rho*}} \nu_*^{x_{\nu*}} \beta^{x_\beta} M^{x_M} q^{x_q} \varepsilon^{x_\varepsilon} \kappa^{x_\kappa}. \qquad (12)$$

The 'engineering' variables are R = major radius (geometric centre), I = plasma current, B = toroidal magnetic field (at major radius R), P = loss power (corrected for charge exchange and orbit losses), n = line average density, κ = elongation, ε = inverse aspect ratio, and M = average ion mass. The 'physics' variables are the Bohm time, τ_B, normalized toroidal Larmor radius, ρ_*, normalized collisionality (with $Z_{eff} = 1$ assumed), ν_*, normalized plasma pressure, β, cylindrical safety factor, q, and are defined by

$$\tau_B = \frac{(\text{minor radius})^2}{\text{Bohm diffusion coefficient}}$$
$$= \frac{a^2 B}{T} \propto \varepsilon^2 R^2 B T^{-1} \qquad (13)$$

$$\rho^* = \frac{\text{ion gyroradius}}{\text{minor radius}}$$
$$= \left(\frac{2eT_i}{M_i}\right)^{1/2} \frac{M_i}{eBa} \propto (MT)^{1/2}/\varepsilon RB \qquad (14)$$

$$\beta = \frac{\text{plasma pressure}}{\text{magnetic pressure}}$$
$$= \frac{2\mu_0 ne(T_e + T_i)}{B^2} \propto nTB^{-2} \qquad (15)$$

$$\nu^* = \frac{\text{connection length}}{\text{trapped particle mean} - \text{free path}}$$
$$= \nu_{ii}\left(\frac{M_i}{eT_i}\right)^{1/2}\left(\frac{R}{a}\right)^{3/2} qR \propto nRT^{-2}q\varepsilon^{-3/2} \qquad (16)$$

$$q_{cyl} = \frac{RB}{\varepsilon^2 I} f(\kappa, \delta) \propto BRI^{-1}\varepsilon^2\kappa \qquad (17)$$

with T_i in eV and $f(\kappa, \delta)$ a function of the plasma shape parameters. These obviously vary across the plasma profile, but for a global analysis temperature, T can be replaced by $[(P\tau_{th})/(6\pi^2 en\varepsilon^2\kappa R^3)]$, using the power balance relation. (See Section 7 for a more detailed discussion of dimensionless parameters.)

On a logarithmic basis the power law expressions are linear and the above relations for the 'physics' variables define a linear transformation between the 'engineering' and 'physics' variables and between their exponents in the scaling expressions. In the following subsections, ordinary least square regression techniques have been used to determine the exponents in the scaling expressions. This requires that the errors on the independent (regressor) variables are negligible compared to that on the confinement time. As this is not satisfied for the 'physics' variables, the regressions must be done using the 'engineering' variables. In addition, various 'physics con-

Table 4. Selection criteria for the standard analysis dataset of ITERH.DB3

1. H-mode data only, with no restriction on heating scheme
2. All essential data available
3. Pellet discharges are excluded
4. Limits on dW/dt
5. Limits on total radiation
6. Limits on q_{95}
7. Limits on fast ion energy content
8. Limits on β
9. Hot ion H-mode data are excluded
10. 1987 JET data are excluded

strained' scalings can be tested against the data. A constrained scaling has one or more constraints imposed on the exponents in the scaling. For example, for the high-β [73], or Kadomtsev [72], constrained scaling, the constraint is $x_{\tau_B} = 1$ in physics variables (or $4\alpha_R - 8\alpha_n - \alpha_I - 3\alpha_P - 5\alpha_B = 5$ in engineering variables). The gyroBohm constrained scaling [47] has two constraints imposed, that of the high-β constraint and $x_{\rho^*} = -1$ (or $6\alpha_R - 22\alpha_n - 9\alpha_I - 12\alpha_P - 15\alpha_B = 0$). The Bohm constrained scaling also has two constraints imposed, that of the high-β constraint and $x_{\rho^*} = 0$ (or $\alpha_R - 7\alpha_n - 4\alpha_I - 7\alpha_P - 5\alpha_B = 0$). See also [316] for further details. In the above definitions, the quantities τ_B, ρ^* and β are based on toroidal quantities, but definitions based on poloidal quantities can also be formulated.

6.3.1. ELMy H-mode thermal confinement scalings

The new ELMy H-mode standard dataset as defined in Section 6.2 for ITERH.DB3 is significantly better conditioned than that of ITERH.DB2. Not only is the database mean of each of the engineering parameters closer to the ITER parameters, but the ranges in R, n, I, P and B are larger. Only three correlation coefficients are larger than 0.7 (between I and P; I and R/a; I and κ). Principal component analysis shows that the extrapolation to ITER is greater than four standard deviations in only one direction and that this is along the largest principal component. This implies that the uncertainty in the ITER prediction using log-linear scalings is reduced.

The new ELMy H-mode standard dataset provides the basis for a robust confinement prediction for ITER. Even large perturbations to the dataset, such as removing each tokamak in turn, systematically increase or decrease the confinement of each

tokamak in turn by 10%, the application of equal tokamak weightings, and the use of various forms of open/closed divertor corrections to the ASDEX and/or PDX data, do not change the prediction to a large extent. In only a few cases do the ITER predictions differ by as much as 20%. Moreover, in contrast to ITERH.DB2, the ITERH.DB3 ELMy H-mode standard dataset satisfies the high-β constraint. The addition of Alcator C-Mod data seems to be responsible for this last result. The resulting high-β constrained ELMy H-mode scaling expression for ITERH.DB3 is, in 'engineering' variables,

$$\tau_{E,th}^{ELMy} = 0.0365 I^{0.97} B^{0.08} P^{-0.63} n^{0.41}$$
$$\times M^{0.20} R^{1.93} \varepsilon^{0.23} \kappa^{0.67} \quad (18)$$

(in s, MA, T, MW, 10^{19} m^{-3}, AMU, m), which translates to the 'physics' form

$$\tau_{E,th}^{ELMy} \propto \tau_B \rho_*^{-0.83} \beta^{-0.50} \nu_*^{-0.10}$$
$$\times M^{0.97} q^{-2.52} \varepsilon^{-0.55} \kappa^{2.72}. \quad (19)$$

The RMSE for this (Eq. (18)) fit, which is shown in Fig. 9, is 15.8%. For ease of future reference, we call this scaling IPB98(y). Its confinement time prediction for ITER is 6.0 s. As described in Section 6.4, other empirical log-linear scalings have been derived that are based on subsets of the standard dataset and which use another definition of kappa to account for the relatively high confinement in the bean shaped PBX-M tokamak. One such scaling, IPB98(y,2), is mentioned in particular. It is expressed in engineering variables as

$$\tau_{E,th}^{ELMy} = 0.0562 I^{0.93} B^{0.15} P^{-0.69} n^{0.41}$$
$$\times M^{0.19} R^{1.97} \varepsilon^{0.58} \kappa_a^{0.78} \quad (20)$$

(in s, MA, T, MW, 10^{19} m^{-3}, AMU, m), and in 'physics' variables as

$$\tau_{E,th}^{ELMy} \propto \tau_B \rho_*^{-0.70} \beta^{-0.90} \nu_*^{-0.01} M^{0.96} q^{-3.0} \varepsilon^{0.73} \kappa_a^{2.3}. \quad (21)$$

The RMSE of this scaling (Eq. (20)) with respect to the ITERH.DB3 standard dataset is 15.6%, and its prediction for ITER is 4.9 s. It should be mentioned that the Kadomtsev constraint is not satisfied when Alcator C-MOD is removed from the dataset on which IPB(y,2) was based. Everything else being kept the same, this leads to, instead of Eq. (20), the IPB98(y,3) scaling in Table 5, which gives a very similar point prediction for ITER as IPB98(y,2). At present, available physical empirical evidence is felt not to be conclusive enough to justify making a preferential recommendation between the just mentioned log-linear scalings.

The scalings (18) and (20) are not very different from the ITERH.EPS97(y) scaling [315], which was based on an earlier version of the DB3 database and on using TAUC93 rather than TAUC92. (As in previous regression analyses, a correction factor TAUC92 [305] or TAUC93 [180] has been used to normalize the data from closed divertor configurations in ASDEX and PDX to data from the more ITER like configurations found in the other devices. TAUC92 and TAUC93 differ only in the method for normalizing the PDX data, see [180,305].) Eqns (18) and (19) were developed using TAUC92. However, when the TAUC93 normalization is used instead, the data also satisfy the gyroBohm constraint, and the confinement time prediction for ITER increases by less than 5%.

Although the new dataset is clearly better conditioned than the previous dataset, some of the existing problems remain and new complications have been added. For example, a limitation is that it is still not possible to establish distinct scalings for the various ELM types with the current database. It should also be noted that the different heating schemes may introduce new systematic differences between the machines through heating profile effects that are not dealt with in this global database.

6.3.2. ELM free H-mode thermal confinement scaling

The ITERH.DB3 ELM free H-mode standard dataset of 1131 observations, as defined in Section 6.2, satisfies both the high-β and the gyroBohm constraints, as was the case for ITERH.DB2. The
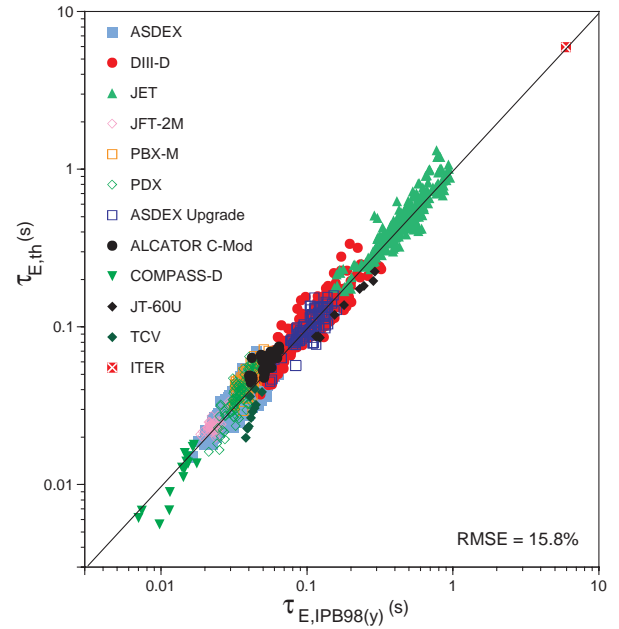

Figure 9. Comparison of H-mode thermal energy confinement time with the scaling expression in Eq. (18) for ELMy data in the ITER H-mode database version DB3.

resulting high-β constrained ELM free H-mode scaling expression for ITERH.DB3 in 'engineering' variables is

$$\tau_{E,th}^{ELM\ free} = 0.0314 I^{0.94} B^{0.27} P^{-0.68} n^{0.34}$$
$$\times M^{0.43} R^{1.98} \varepsilon^{0.10} \kappa^{0.68} \quad (22)$$

(s, MA, T, MW, 10^{19} m^{-3}, AMU, m), which translates to the 'physics' form

$$\tau_{E,th}^{ELM\ free} \propto \tau_B \rho_*^{-0.89} \beta^{-0.92} \nu_*^{-0.13}$$
$$\times M^{1.78} q^{-2.77} \varepsilon^{-1.17} \kappa^{2.90}. \quad (23)$$

The RMSE for this fit is 15.6% and the distribution of the fit is shown in Fig. 10. Equation (22) is similar to the scaling developed from ITERH.DB2, referred to as ITERH93-P [180], and the projections to ITER are almost the same.

6.3.3. L-mode thermal confinement scaling

The present L-mode database [112] consists of 2938 observations from 14 tokamaks (Alcator C-Mod, ASDEX, DIII, DIII-D, FTU, JET, JFT-2M, JT-60U, PBX-M, PDX, TEXTOR, TFTR, Tore-Supra and T-10), of which 1881 are L-mode points. The remainder relate to ohmically heated and enhanced L-mode operation. The L-mode database
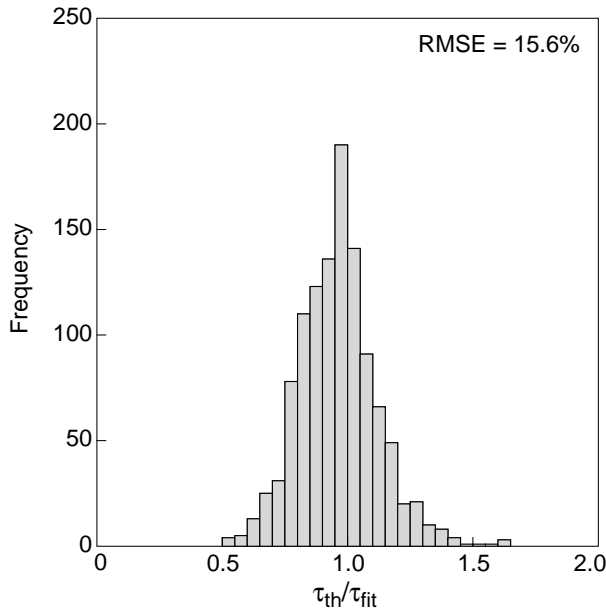
Figure 10. Distribution of H-mode thermal energy confinement time about the scaling expression in Eq. (22) for ELM free data in the ITER H-mode database version DB3.

contains sufficient fast ion information, in the case of neutral beam injection, to calculate both the thermal and the global (i.e. including fast ions) confinement times. This subsection is concerned with the results for the thermal confinement time.

In the L-mode database, 1312 observations contained enough information to determine τ_{th}. Of these, 861 were from limiter discharges and 451 were from divertor discharges. The latter came predominantly from more modest sized devices with greater shaping capability, for example DIII-D and JFT-2M. The limiter subset contained 627 observations from JET, JT-60, TFTR and Tore-Supra, while the divertor subset contained no TFTR or JET L-mode. Discharges with helium gas were excluded to avoid difficulties with the species dependence (i.e. both A and A/Z).

A standard power law regression gives the following fit to the thermal confinement data for the combined limiter and divertor data subsets

$$\tau_{E,th}^{L} = 0.023 I^{0.96} B^{0.03} P^{-0.73} n^{0.40}$$
$$\times M^{0.20} R^{1.83} \varepsilon^{-0.06} \kappa^{0.64} \quad (24)$$

(s, MA, T, MW, 10^{19} m^{-3}, AMU, m). The Kadomtsev constraint is satisfied within statistical uncertainty. Multiplication of (24) by $R^{-0.05}$ leads to the

exactly constrained 'physics' expression

$$\tau_{E,th}^{L} \propto \tau_B \rho_*^{0.15} \beta^{-1.41} \nu_*^{0.19} M^{0.67} q^{-3.74} \varepsilon^{-0.09} \kappa^{3.22}. \quad (25)$$

The RMSE is 15.8% (see Fig. 11) and the thermal energy confinement time extrapolation for ITER is 2.2 s. Virtually no overall difference between the divertor and limiter data with respect to the fit to the scaling expression has been found.

A comparison of the H-mode thermal confinement times from the ITERH.DB2 database with the L-mode scaling expression, shows that the ELM free data have an average enhancement factor (over L-mode) of 1.72, while ELMy data have an average enhancement factor of 1.48. However, as is apparent from Fig. 12, the enhancement factor varies with the size of the machine, tending to be larger in larger devices. The transformation between the engineering and plasma physical parameters naturally inflates the difference in the exponents between the L-mode and H-mode scalings [315, 320].
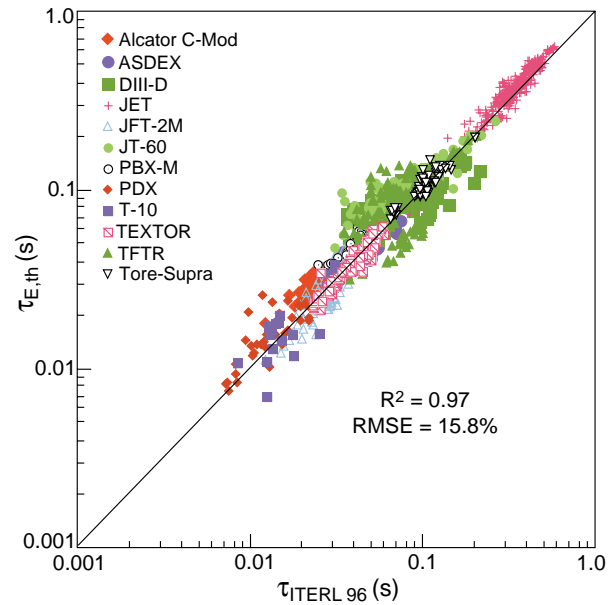
Figure 11. Comparison of L-mode thermal energy confinement time with the scaling expression in Eq. (24) in the ITER L-mode database version DB1.

6.4. Point and interval estimation for the confinement time in ITER

Statistical forecasting is sometimes viewed as a game against nature, considered as an intelligent opponent [318]. Given the possible consequences associated with losing such a game, it goes without saying that a reliable empirical prediction of the

Figure 12. Confinement enhancement factors of the ELMy discharges in the working dataset of ITERH.DB3, as a function of minor radius, a(m). The different symbols denote the various tokamaks.

confinement time of a device with the importance of ITER requires a thorough search for alternative possibilities, based on several data analyses. In this vein, in the present section we investigate, in somewhat more detail than in Section 6.3:

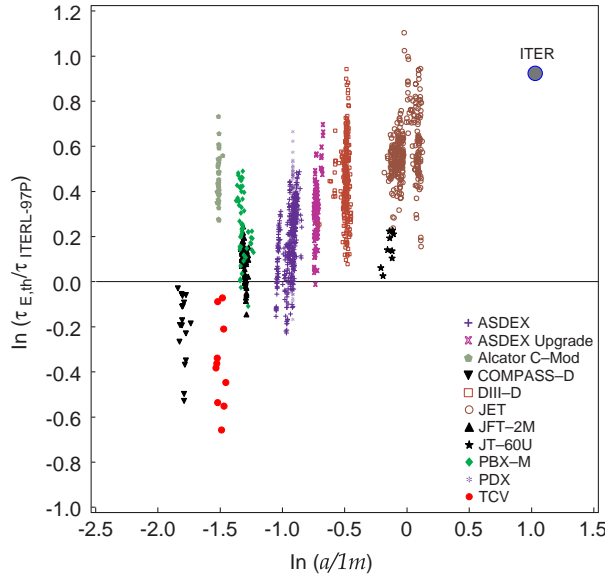(a) point prediction from log-linear scalings based on various subsets of the working dataset;

(b) regression fits to the data by log-non-linear scalings; and

(c) construction of an interval estimate for the confinement time.

The main results are presented here, while further details of a more technical nature are given in the Appendix.

As can be seen in the Appendix, the full DB3 working dataset contains several additional devices and is less homogeneous with respect to the additional heating than the DB2 standard dataset. Two influences on the point prediction for ITER, the variation due to several different subsets of the standard dataset and the impact on aspect ratio scaling as a result of using an alternative definition of κ that de-emphasizes the extreme (i.e. bean) shaping of PBX-M, are summarized in Table 5. The table contains exponents and predictions for ITER for several log-linear scalings. Scalings IPB(y) and IPB(y,1) are based on the full working dataset, IPB(y,2) is

based on the dataset DB2.8 (i.e. DB3 restricted to NBI discharges only, but including Alcator C-Mod), IPB(y,3) on DB2.5 (i.e. DB3 restricted to NBI only, and excluding Alcator C-Mod), and IPB(y,4) on DB2.8(IS) (i.e. DB2.8, restricted to its five ITER similar devices). The point predictions in Table 5 vary between 4.9 and 6 s with an average (rounded within $\pm 2\%$) of 5.5 s. Since the Kadomtsev constraint was satisfied within statistical uncertainty, the dimensionally restricted form of the scalings is presented in Table 5 for IPB(y), IPB(y,1-2) and IPB(y,4). In the case of IPB(y,3) the Kadomtsev constraint is not satisfied, and the free regression fit is shown.

Comparison of the first two cases in the table shows, for the full DB3 working dataset, the impact on aspect ratio scaling associated with redefining elongation. PBX-M has systematically high residuals with respect to usual log-linear scaling expressions, such as Eq. (18), which corresponds to the first case in Table 5. To account for this, the elongation has been defined in the remaining four cases in the table as $\kappa_a = \text{area}/\pi a^2$, which leads to a similar aspect ratio dependence as when PBX-M is dropped from the dataset. The ratio κ_a/κ is 1.3 ± 0.1 for PBX-M, and 0.9 ± 0.1 for all other tokamaks in the standard dataset, the difference being directly related to the indented shape of the PBX-M plasmas. The first two lines in the table indicate that redefining kappa in this way does not notably change the ITER prediction. On the other hand, restricting the full working dataset to its three subsets defined above gives a range in ITER confinement prediction between some 5 and 6 s, and only a small variation in the aspect ratio dependence. On average, the IPB98(y)(1–4) scalings in Table 5 lead to a 10% more conservative prediction for ITER and to a stronger inverse aspect ratio dependence than the IPB98(y) scaling.

Another topic is the variation of the predictions with respect to weighting the observations (between equal weight per observation and per tokamak). This is addressed in Appendix A and summarized in Fig. 27. In summary, this aspect increases the range of the predictions, even at a weighting exponent $\frac{1}{3}$, which is somewhat closer to equal observation than to equal tokamak weighting.

Even with these facets taken into account, the log-linear scalings do not reflect the full range of statistically 'admissible' point predictions that stem from log-non-linear scalings. While this topic is further addressed in the Appendix, we give a brief discussion here.

Table 5. Exponents of the several empirical log-linear scalings based on ITERH.DB3

Scaling	C (10^{-2})	I	B	n	P	R	$\kappa_a^{(1)}$	a/R	M	N	RMSE (%)	ITER τ_E (s)
IPB98(y)	3.65	0.97	0.08	0.41	-0.63	1.93	0.67	0.23	0.20	1398	15.8	6.0
IPB98(y,1)	5.03	0.91	0.15	0.44	-0.65	2.05	0.72	0.57	0.13	1398	15.3	5.9
IPB98(y,2)	5.62	0.93	0.15	0.41	-0.69	1.97	0.78	0.58	0.19	1310	14.5	4.9
IPB98(y,3)	5.64	0.88	0.07	0.40	-0.69	2.15	0.78	0.64	0.20	1273	14.2	5.0
IPB98(y,4)	5.87	0.85	0.29	0.39	-0.70	2.08	<u>0.76</u>	0.69	0.17	714	14.1	5.1

[1] The quantity κ_a has been defined as area/πa^2 in the scalings IPB98y(1,2,3 and 4) and as $\kappa = b/a$ in the scaling IPB98y. For IPB98y(4), the exponent κ is underlined to indicate that it imposed (as the average of IPB98y(1,2 and 3)) on the regression fit. For the ITER predictions, a cross-sectional area of 39.1 m^2 was used; see [319]. Wherever it is compatible with the data, the Kadomtsev constraint has been applied. For IPB(y,3) the free fit is presented.

Since a log-linear model corresponds to a similar scaling of the core plasma and of the edge plasma, the possibility that the global ELMy H-mode confinement is actually better described by a log-non-linear model than a log-linear model should not be dismissed lightly. To estimate its impact on the prediction for ITER, we consider a variety of alternative empirical models. One ('DK-96') is an interaction model [321], which contains a significant cross term between q_{cyl} on the one hand, and $(na^2)^{1/2}(q_{95}/q_{cyl})$ on the other. Secondly, an offset linear scaling [440] based on the (DB2) ELM free dataset is taken and multiplied with an empirical factor c_{ELMy}, found by looking at the residuals from the ELMy (DB2.5) dataset with respect to this scaling. The resulting scaling is labelled as OK-96. Finally, an ELMy offset non-linear scaling [320] based on DB2 plus JT-60U ('TT-96') is employed. These scalings and their predictions are described more fully in the Appendix, Section A1. The ensuing point estimates for the confinement time in ITER vary between some 4.4 and 7.3 s. If one wants to be pessimistic, it is possible to obtain considerably lower predictions (some 3 s or below) by optimizing non-linear models with respect to the RMSE of the fit and, simultaneously, towards a low value of ITER confinement. However, such a procedure is not considered to be statistically admissible and is not pursued any further here.

In addition to investigating the variation of the point estimates, it is interesting to look at statistical confidence intervals associated with each of the models and data subsets. This is easily done for log-linear models where, according to [312, 315], the classical statistical interval can be written as

$$\ln(\hat{\tau}_E) \pm c \sum_{j=1}^{p} \left(1 + \frac{\hat{\lambda}_{ITER,j}^2}{\hat{\lambda}_{pc,j}^2}\right)^{1/2}. \quad (26)$$

As derived in [312], this equation is based on the representation in which the data from the p explanatory variables are geometrically described by a data cloud of N observations in p dimensional space. This cloud is approximated by a family of concentric ellipses that match all first and second order moments. The projections of the data on the principal axes of the ellipses are called the principal components. In Eq. (26), $\lambda_{pc,j}$ denotes the standard deviation of the jth principal component and $\lambda_{ITER,j}$ is the distance of the centre of the database to the ITER reference operating point in the direction along the jth principal axis.

A delicate point is the proportionality factor c in this expression, which is traditionally $2\hat{\sigma}/\sqrt{N}$ for a (two sided) 95% interval, with $\hat{\sigma}$ the RMSE of the fit. In a simple approach, the total number of observations, N, is replaced by N_{eff}, representing the number of independent data points. As a first approximation, it has been assumed [320] that $N_{eff} = N/4$, where the factor 4 roughly accounts for the correlations between data points, e.g. stemming from the fact that several have been taken during the same discharge. A more thorough assessment of the proportionality constant has been developed in [321] and is summarized in the Appendix. This approach yields a 95% log-linear uncertainty interval for the confinement time of $(+25\%, -20\%)$, to be interpreted as the range of values into which 95% of a large number (say 1000) of discharges performed at the ITER stan-

dard operating point would fall. This interval, which includes the variation in point prediction from the different weightings in Fig. 27, presupposes, however, that a log-linear model is 'essentially' correct and all major influences have been taken into account. Since we know this is only approximately true, we have to consider a larger range of possibilities. This has led to several 'definitions' of a 95% interval estimate [320, 321], each definition describing a particular aspect of the uncertainty. From the discussion in the Appendix, we recall the variation due to the (point) predictions from 'admissible' non-linear models, which is about twice as large as the interval above, see Table 14. In addition, 'jackknife type' interval estimates can be considered, based on the variation of point estimates from log-linear models fitted to subsets obtained by deleting data from one tokamak in turn from the database. The statistical justification of this somewhat automatic approach is rather subtle. In fact, there are two versions of this type of estimate, which give intervals close to the above mentioned log-linear and log-non-linear intervals, respectively, see the Appendix and [321,322] for further details.

The summary interval estimate from the Appendix is graphically represented in Fig. 13. In this figure, the large interval is interpreted as a 95% log-non-linear interval, and the smaller interval as both a $\frac{2}{3}$ log-non-linear and a 95% log-linear interval. It should be noted that all log-linear and log-non-linear scalings discussed in the Appendix give point predictions for the nominal ITER parameters [323], which are within or above the smaller interval (see Table 14).

With respect to other factors that may influence the confinement time, but which are poorly accounted for in the dataset, we mention that, for practical reasons, the power lost by radiation inside the separatrix of the existing devices has been neglected when deriving the scalings. However, for ITER, such radiation is subtracted from the loss power when calculating the projected energy confinement time. This approach has been motivated by the fact that ITER, in contrast to the present day tokamaks, will have a substantial amount of bremsstrahlung and cyclotron emission from the plasma centre. The ensuing somewhat (10–15%) conservative effect on the ITER prediction is qualitatively counterbalanced by the difference in heating profile between the high-Z wall material small devices (ASDEX, JFT-2M, PDX, PBX-M) and low-Z wall material larger devices (ASDEX-Upgrade,

DIII-D, JET) in the DB2.5 (NBI only) dataset. Some aspects of the role of wall conditioning (by analyses similar to those in [324]), and of difference between closed and open divertor machines, have been dealt with in the correction factor TAUC92. However, analysis of ASDEX L-mode confinement [321] suggests that the latter influence is more complicated than is assumed in the present simplified approach. An element not present in these simple log-linear scalings is a possible reduction of the confinement time for plasmas near the H-mode existence region. Further issues are that the possible effects of plasma rotation on local transport, and, hence, global confinement, have not been addressed, nor are those from the profile shapes of the plasma current, magnetic configuration and electron density. On the one hand, such effects can lead to modifications of the present scalings, while on the other they could possibly provide additional flexibility to optimize the energy confinement in ITER over the accessible operating range.

7. Scaling studies with similar dimensionless physics parameters

7.1. Basics

Quasi-neutral plasma turbulence is believed to govern transport processes in the core of tokamak plasmas. This led Kadomtsev to observe [72] that transport in the plasma core should be fundamentally governed by three physical dimensionless plasma parameters, denoted by ρ^*, ν^* and β, as well as other geometrical and engineering parameters $\{p_i\}$ defined below, which, at least in principle, are under the control of the experimental physicist and, in present machines, can be made close to ITER values. The non-dimensionally similar approach to confinement scaling is to create, in present machines, discharges that are as similar to ITER as possible, with fundamental dimensionless parameters being the measure of similarity. These have become known as ITER demonstration discharges. For those parameters that cannot be matched, experimental scans are carried out to determine both the actual value of the energy confinement time as well as its scaling with dimensionless parameters. An analogy has often been drawn between this approach and wind-tunnel tests of aircraft designs.

Mathematically, the non-dimensionally similar approach implies that the non-dimensional energy
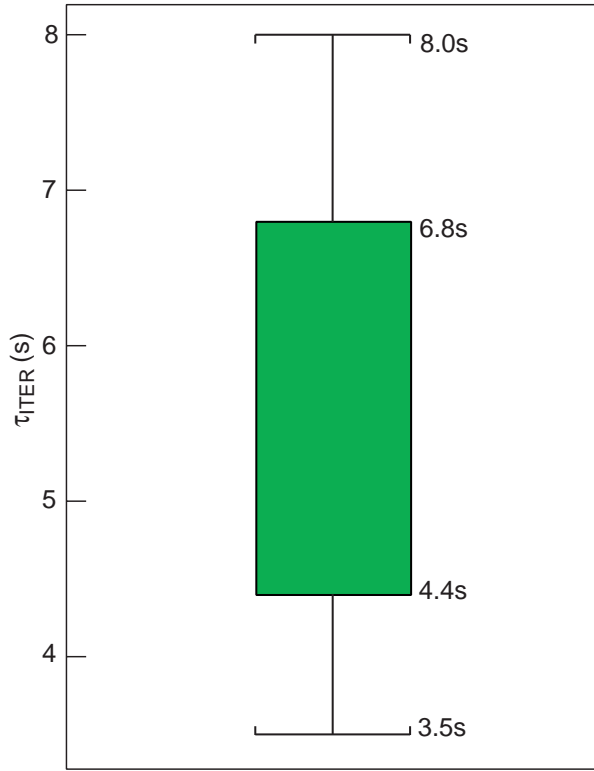
Figure 13. Interval estimation of the energy confinement time in ITER at the reference operating point. The inner box indicates a '95% log-linear' interval, whereas the region enclosed by the wiskers is an estimate of a '95% log-non-linear' interval. In this case, the inner interval corresponds roughly to a '$\frac{2}{3}$ log-non-linear' interval. The centre of the intervals approximately coincides with the average of the IPB98(y) and IPB98(y,2) scalings.

confinement time $\Omega_i \tau_E$ can be expressed as

$$\Omega_i \tau_E = F(\rho^*, \nu^*, \beta\{p_i\}). \qquad (27)$$

The list of other parameters $\{p_i\}$ is long (see Eq. (8)). Table 1 in [74] presents a list of 18 dimensionless parameters. Representative examples are q, κ, R/a, T_i/T_e, Z_{eff}, single null divertor, H-mode edge, as well as density profile shape and auxiliary power deposition profiles. Contemporary theories of flow shear stabilization suggest that the toroidal Mach number $V_\phi(T/M)^{-1/2}$ is a key dimensionless parameter, which has previously been neglected. The definitions we adopt are as defined in Eqns (13)–(17), and the degree to which these parameters can be made identical to ITER will be discussed below.

The concept of discharges with similar dimensionless parameters arises from dimensional analysis of the equations governing microinstability plasma turbulence [73], which proceeds in a five dimensional

phase space – only the fast gyration motion of particles around the field lines can be averaged over. The fundamental equation is a Boltzmann equation for a five dimensional distribution function coupled with the constraint that the divergence of the current density moment must vanish. Definitions given by Eqns (13)–(17) are motivated by the fact that when a characteristic spatial length of the ion gyroradius and a characteristic velocity – the diamagnetic drift velocity – are introduced, as well as a typical fluctuating amplitude $\tilde{n}/n \sim \rho^*$ [47, 326–328], then the dimensionless, non-linear Boltzmann equation contains coefficients of order unity, indicating that a self-consistent scaling has been obtained. A secondary expansion in collisionality, ν^*, is often made, because ITER will lie in the region where $\nu^* \ll 1$. A key step in this procedure is to assume that the turbulence is local and that its saturation level is governed by local quantities, such as T, and their gradients.

An examination of the requirements for matching dimensionless parameters shows that ITER can be matched in the ν^* and β parameters, but not in the parameter ρ^*. ITER will have ρ^* values 5–8 times less than present tokamaks. In order to match ITER ν^* and β values in present tokamaks, the discharge density and temperatures should be scaled from ITER values according to [329]

$$n \propto B^{4/3}R^{-1/3}, \qquad T \propto B^{2/3}R^{1/3}. \qquad (28)$$

Table 6 lists representative discharge conditions with the same β and ν^* values as ITER. They are compatible with standard operating regimes in the various devices, indicating that present tokamaks can be in the same physics regime as ITER.

For the remaining parameter ρ^*, the standard assumption is that the function F can be taken to be a power law in ρ^*

$$F = (\rho^*)^{-(2+\alpha)}\bar{F}(\nu^*, \beta, \{p_i\}) \qquad (29)$$

where the exponent α is expected to lie in the range $0 \le a \le 1$, the upper and lower limits corresponding to Bohm or gyroBohm scaling, respectively. The power law form is equivalent to the assumption that there is no characteristic value of ρ^*, and, hence, no characteristic length, that governs microinstability turbulence scaling apart from the particle gyroradius and plasma size a. The value of the exponent a then determines a characteristic turbulence scale size $\ell \approx \rho_i^\alpha a^{1-\alpha}$. Even though one can identify other characteristic microscopic lengths in the core plasma, for constant β and ν^* these lengths scale as ρ_i and, thus,

would not change the relation between α and ℓ. This is fortunate because it is planned to operate ITER near its β limit so that a power law assumption for β scaling is not generally valid. Instead, physics arguments suggest that the confinement should be independent of β at low β, where the turbulent transport is a consequence of electrostatic micro-instabilities and should degrade dramatically as the MHD β limit is approached. On the other hand, because $\nu^* \ll 1$, magnetically trapped particles bounce many times before detrapping occurs, so one would expect transport to be governed by collisionless physics and to be only weakly dependent on ν^*.

From Table 6 we note that the ρ^* value for ITER is 4.6 times smaller than the values achieved on JET, and that the range of ρ^* available is roughly a factor of 3. (Recognize that many of the devices in Table 6 can be operated at lower fields than indicated and, hence, at greater ρ^*.) The additional range in ρ^* represented by Alcator C-Mod and COMPASS-D would serve to reduce the uncertainty of ITER projections. Smaller values of ρ^* could be attained by 4 T operation on JET (reducing ρ^*/ρ^*_{ITER} to $\rho^*/\rho^*_{ITER} = 3.3$) if there were sufficient auxiliary heating power to attain ITER β and ν^* values.

This approach to the analysis of transport and confinement based on similar dimensionless physics parameters addresses the fact that, in principle, the gyroradius scaling of plasma turbulence could depend on β, collisionality, or any other non-dimensional parameter. For example, different scalings might arise in the collisionless ($\nu^* \ll 1$) and collisional ($\nu^* \gg 1$) regimes. Expressed in terms of Eq. (29), this implies that the exponent α could be a function of β, ν^* or density profile index α_n ($= [(a^2 - r^2)/2rn_e] \times dn_e/dr$). Indeed, experiments find that the exponent α differs for L-mode and H-mode discharges, indicating a dependence on other non-dimensional parameters. For this reason, it is important to determine the ρ^* scaling exponent at ITER relevant ν^* and β values and with ITER like flat density profiles.

While most of the scaling studies with similar dimensionless parameters have focused on the ρ^* scaling of nominal ITER discharges, it is also of interest to determine how ITER confinement will depend on other parameters under experimental control, e.g. q, β and ν^*. These studies are needed to project the response of ITER to variations in operating conditions. Scans in these parameters can be carried out at fixed ρ^*, which, while much larger than the ITER value, is nonetheless sufficiently small that one

can argue that there is a common physics governing transport. The case would be strengthened by observation of common β and ν^* scalings at several ρ^* values.

7.2. Discharges with identical dimensionless parameters

An evident question for transport scaling with similar dimensionless parameters is: do experiments support Eq. (27)? The answer lies in preparing discharges with identical dimensionless parameters, but distinctly different physical values. The value of $\Omega_i \tau_E$ should remain invariant. Such comparisons have been made for circular ohmic tokamaks [74] and for auxiliary heated, ITER like tokamaks [315, 330], albeit at β values below the planned ITER value. Good agreement was obtained. Table 7 presents the results for an ITER like JET/DIII-D comparison [330].

Further comparisons are planned for Alcator C-Mod, DIII-D and JET. In addition, an extension of this approach to the H-mode power threshold is also under consideration. For discharges with identical dimensionless parameters, the relation $P_{thresh}a^{3/4} = $ const. is predicted. One can also note that unconstrained, power law regression analyses of global confinement scaling fulfil a constraint on the exponents derived from Eq. (27). Based on present evidence, one can conclude that experiments are indeed in accord with Eq. (27) [315].

7.3. Results of experiments with similar dimensionless parameters

Scans in ρ^* with similar dimensionless parameters β and ν^* have been carried out for ELMy H-mode ITER demonstration discharges on ASDEX-Upgrade [91], Alcator C-Mod [331], DIII-D [76, 330, 332], JET [276], and JT-60U [322]. Results for L-mode scaling are available for DIII-D, ASDEX-Upgrade and JT-60U. A principal conclusion is that the confinement scaling exponent, α, depends on the confinement mode.

A successful ELMy H-mode ρ^* scan requires careful matching of β and ν^* profiles, an operating regime that attains $T_e \approx T_i$, and similar, preferably flat, density profile shapes. Figure 14, taken from [76], illustrates the excellent agreement obtained on DIII-D ρ^* scans. Similar success was achieved on JET and JT-60U ρ^* scans, as well as JET and DIII-D β and ν^* scans. Table 8, adopted from [315], presents the values of α obtained in the DIII-D and JET exper-

Table 6. Representative discharge parameters scaled from ITER at constant β, Z_{eff} and ν^*

Parameter	ITER	JET	JT-60U	ASDEX-Upgrade DIII-D	Alcator C-Mod	COMPASS-D
B (T)	5.7	2.5	1.8	2.1	5.0	2.2
R (m)	8.1	2.9	3.2	1.67	0.67	0.56
n_{20}	1.0	0.47	0.3	0.45	1.9	0.68
$T(0)$ (keV)	20.0	8.2	6.8	6.1	$8.0^{(1)}$	$4.3^{(1)}$
ρ^*/ρ^*_{ITER}	1.0	4.6	4.7	7.3	8.7	17.4

$^{(1)}$ Alcator C-Mod and COMPASS-D need additional auxiliary heating to reach this value.

Table 7. JET and DIII-D non-dimensionally identical discharges

	a (m)	B (T)	I_p (MA)	n_{19}	W (MJ)	P_{tot} (MW)	τ_{th} (s)	$B\tau_{th}$
DIII-D	0.56	2.10	1.14	7.6	0.60	6.1	0.10	0.21
JET	0.97	1.07	1.0	2.4	0.84	4.25	0.20	0.21

iments, together with a simple estimate of the 2σ uncertainty.

The errors in $\delta\tau$ are assumed to arise entirely from errors in the determination of the parameter α in the ρ^* scaling experiments. For a standard error of $\pm 15\%$ (2σ) in the stored energy, the 2σ error in the parameter α will be $\delta\alpha = \pm 0.4$ for DIII-D, and $\delta\alpha = \pm 0.3$ for JET. The reason the errors are so large is due to the fact that the range in ρ^* is very small in the experiments (DIII-D; $\rho^*_{1\,T}/\rho^*_{2\,T} = 1.6$ and JET; $\rho^*_{1\,T}/\rho^*_{2.6\,T} = 1.9$).

To reduce the errors in the prediction of confinement, it will be necessary to complete a joint ρ^* scan on at least two machines of different sizes to increase the range of ρ^*. Table 6 indicates that Alcator C-Mod and COMPASS-D ρ^* scans would be valuable additions to the database.

JT-60U [232] has also carried out an ELMy H-mode ρ^* scan at $\beta_N = 0.8$ and $q_{eff} = 4.4$. Profiles of β and ν^* were well matched. High triangularity was used to reduce the effect of ELMs on confinement. The results show $\alpha = 0.8$ and, like DIII-D, an appreciable difference between L-mode and H-mode in the ρ^* scaling of the ion heat transport. ASDEX-Upgrade [91] finds gyroBohm scaling in H-mode when local profiles are matched, but Bohm scaling in L-mode. ASDEX-Upgrade was unable to reach a density low enough to match ITER ν^* values. Initial H-mode scaling studies on Alcator C-Mod find $\alpha = 1.1 \pm 0.7$, i.e. gyroBohm scaling with appreciable uncertainties.
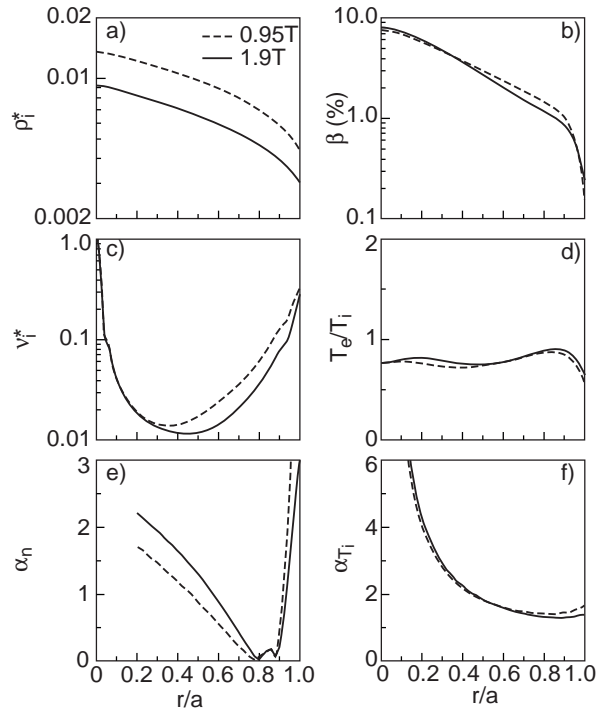

Figure 14. Radial profiles of (a) relative ion Larmor radius, (b) thermal beta, (c) ion collisionality, (d) ratio of electron to ion temperature, (e) non-dimensional density scale length, and (f) non-dimensional ion temperature scale length at 1.9 T (solid lines) and 0.95 T (dashed lines) for H-mode discharges in DIII-D [76].

Figure 15 portrays the results of JET and DIII-D ρ^* scans compared to the ITER93H-P scaling rela-

Table 8. Experimental determination of the ρ^* scaling exponent α for ELMy H-mode discharges

Tokamak	β_N	ρ^*/ρ^*_{ITER}	α	$\delta\alpha$	$\tau_{th,ITER}$ (s)	$\delta\tau(\sigma)$
DIII-D	2.1	7.7	1.1	± 0.4	28	± 18
JET	2.2	5.5	0.7	± 0.3	6.4	± 3

tion, which has $\alpha = 0.7$. It is clear that, for discharges carefully constructed to be as ITER like as possible with present devices, this value of $\alpha = 0.7$ describes the experimental situation well.
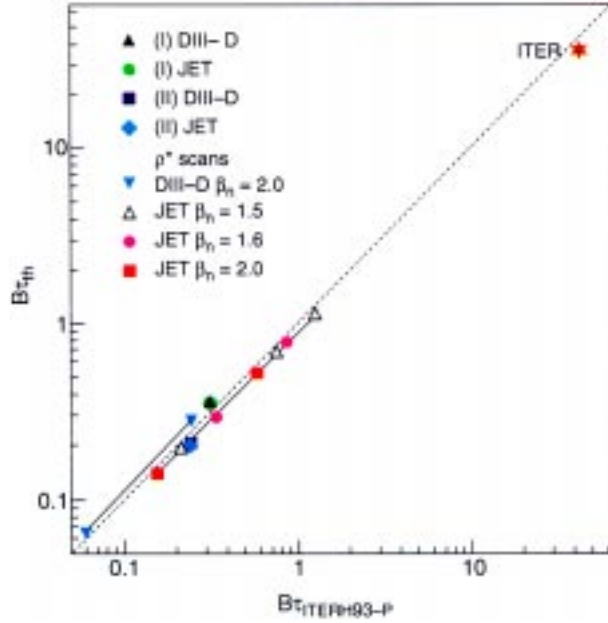
Figure 15. Comparison of $B\tau_E$ measured in ρ^* scans on JET and DIII-D with the ITER93H-P scaling relation.

JET and DIII-D have also carried out an investigation of β scaling and ν^* scaling. The results indicate that confinement is independent of β for $\beta_N < 2.0$. Moreover, the ν^* dependence is non-existent for L-modes and weak, $\Omega_i\tau_E \propto (\nu^*)^{-0.3}$, for H-modes. The DIII-D team argued that the weak ν^* scaling could be attributed to ion neoclassical physics, which would be negligible in ITER. The β scaling experiments found little dependence of confinement on β, which disagrees with global scaling relations. Collinearities in the global database are a possible explanation [334]. Alcator C-Mod reported a $1/\nu^*$ dependence on collisionality [335].

Turning to L-mode results, global L-mode ρ^* scaling experiments, carried out by TFTR, DIII-D, ASDEX-Upgrade and JT-60U, have concluded that the τ_E scaling is Bohm like, which again indicates that the scaling exponent, α, must depend on some

non-dimensional parameter that differs from L-mode to H-mode.

It is illuminating to analyse the parameters of ITER demonstration discharges locally. In a ρ^* scan, one can compute, as a function of minor radius, the ratio of thermal conductivity (or heat flux) between member discharges of a ρ^* scan. With the aid of transport analysis codes this can be done for the total heat flux or for the electron and ion channels separately. Analysis of data from JT-60U [333] and DIII-D [76] indicates that the major change between H-mode and L-mode discharges is the scaling of the ion thermal flux, which improves from worse than Bohm in L-mode to close to gyroBohm in H-mode. Interestingly, the electron channel exhibits gyroBohm scaling for both L-mode and H-mode. The overall Bohm scaling in L-mode results from the combined electron and ion channel scaling. Under the assumption of local transport, the difference between L-mode and H-mode must result from a change in some other local, non-dimensional parameter, such as the density gradient index α_n.

7.4. Limitations on transport scaling studies with similar dimensionless parameters

Conceptually, the non-dimensional approach to determining confinement scaling is simple and direct: create a discharge as close to ITER conditions as possible and then experimentally determine the scaling in the single remaining parameter, ρ^*. Limitations arise because of bias and correlations that are generated in attempting to create ITER like discharges. A discussion of some of these limitations follows.

Arguably the most important potential source of bias is toroidal rotation and rotational shear arising from the directed NBI heating commonly used on tokamaks. It is argued that this shear will suppress micro-instabilities and improve confinement. Comparison of discharges with radio frequency heating, which has effectively no source of angular momentum input, versus those with directed NBI on the same device should elucidate, and perhaps resolve, the flow shear issue. The JET facilities are well suited to this investigation.

Successful scaling experiments with similar dimensionless parameters call for appropriately scaled plasma densities and identical plasma density profile shapes; an area where experimental control is limited at best. Plasma fuelling via gas puff, NBI and inside/outside launch pellets can act to produce variations in the density profile, which could affect transport scaling properties. Because only peripheral pellet or gas puff fuelling is anticipated for ITER, very flat density profiles are likely, in accord with observations on JET. Planned upgrades to present experimental capabilities, including both highly baffled divertors with domes and efficient inside pellet fuelling, may serve to increase the degree of experimental control on the profile shape. Active control of the density profile shape would elucidate a presently poorly characterized aspect of transport and its scaling.

A continuing anomaly in tokamak transport arises from the observation, on the one hand, of gyroBohm like core confinement scaling and, on the other, the observed isotope effect wherein heavier hydrogen isotopes exhibit somewhat superior confinement. Simple gyroBohm scaling is well known to have a weak inverse isotope effect. Some additional mechanism and its associated non-dimensional parameter must, therefore, be at work. Suggestions include ELM induced confinement degradation, impurity modes and impurity concentrations, flow shear effects, non-linear ion Landau damping processes, and fast ion concentrations. In fact, the recent JET experiments on the isotope scaling have shown that the positive mass scaling comes from the pedestal [259] and not the plasma core. Although there has been a strong observational program focused on identifying that an isotope effect exists [116], the problem has not been approached from the view of validating candidate mechanisms. More fully developed theoretical models of the various proposed mechanisms are needed so that a set of predicted consequences is available for experimental tests. The goal is to achieve an intellectual framework that can support both gyroBohm scaling and a (albeit weak) positive isotope effect; as is currently employed for ITER confinement projections. One should keep in mind that isotope effects may involve more than one mechanism.

Scaling experiments with similar dimensionless parameters focus on the thermal plasma and neglect any influence from energetic ions arising from NBI or radiofrequency heating. In present devices, the ratio of total fast ion energy to thermal energy is of order ~ 0.2, while in ITER, the fast ion energy content will

be negligible because the ratio of ion slowing down time to the energy confinement time will be much less than unity. At present there is no systematic understanding of whether or how the presence of fast ions could affect transport.

Indeed, one can generalize this potential source of bias to the question: what is the appropriate definition of collisionality? The conventional choice of ν^* governs whether trapped particles can complete a full banana orbit. The quantity $\tau_E \nu_{ie}$, which measures the importance of electron–ion energy exchange and the fast particle concentration, could provide another definition. This parameter assumes importance in supershot plasmas, where the value $\tau_E \nu_{ie} \sim 1$ permits $T_i \gg T_e$, a condition known theoretically and experimentally to reduce transport. Such plasmas are not accessible for ITER, which will have $\tau_E \nu_{ie} \gg 1$. In ITER demonstration discharges, operational steps are taken to assure $T_e \approx T_i$.

A current and key issue for tokamak transport is: how 'stiff' is the transport arising from ITG modes, where the ion heat diffusivity depends on the departure of the ITG from a critical gradient. In a 'stiff' system, where the ion heat flux increases rapidly when the critical gradient is exceeded, small relative deviations from the critical gradient will be observed. This causes difficulties for non-dimensional scaling analyses and, in its extreme form, makes the core temperature directly proportional to the boundary temperature, which may not have the same physics scaling. Due to measurement inaccuracies and theoretical uncertainties in the critical gradient, it is difficult to apply dimensionless scaling to stiff systems. Some ITG theories result in a stiff system [75]. Transient L-mode transport experiments on ASDEX-Upgrade, however, suggest the system is not stiff [91].

ELMs constitute a rather uncontrolled boundary condition for heat transport. To minimize ELM effects on transport scaling, it is desirable that only a small fraction of the power outflow across the separatrix occurs as a result of ELMs. A key scaling difficulty is that present ITER demonstration discharges have a power loss through the separatrix well above the H-mode power threshold, resulting in strong type I ELMs. The difference in the scaling of the threshold and transport loss powers indicate that ITER will operate close to the H-mode power threshold, which can affect ELM activity.

Summarizing, dimensionless transport studies can benefit from experiments on present facilities, which can remove or reduce the limitations described above.

7.5. Summary

Dimensionless scaling studies are performed under the assumption that the problem of scaling transport from present experiments to ITER can be reduced to the determination of a single exponent, α, defined in Eq. (29). Experiments to determine the scaling exponent on several devices conclude that α is not a constant, but can depend on the transport regime and, thus, on the other non-dimensional variables of the discharge. Therefore, it is important the transport scaling for ITER be determined by discharges with ITER like non-dimensional parameters. For H-modes, the overall scaling in dimensionless similarity experiments is close to gyroBohm, with $\alpha = 0.9 \pm 0.3$, in accord with the concept that plasma transport is dominated by low-β, electrostatic, collisionless instabilities. L-mode discharges, on the other hand, exhibit Bohm scaling, which is further found to be a combination of gyroBohm electron transport and worse than Bohm ion transport. To a good measure, these observations are common to several tokamaks, engendering confidence in the results. Nevertheless, a local control parameter that governs the transition to gyroBohm scaling remains unidentified.

Reducing the uncertainty in α expressed in Table 8 will require experiments with a greater range in $\rho^* \propto I_p^{-2/3} R^{-1/6}$. Therefore, it would seem that the largest and smallest tokamaks – JET and COMPASS-D – can generate the greatest difference, and this emphasizes the importance of 4 T operation on JET and the beginning of ρ^* scans on COMPASS-D. JT-60U could also lower the ρ^* ratio to $\rho^*/\rho^*_{ITER} = 3.3$ at ITER like β and ν^*, if operation at $n_{20} = 0.6$ and $B = 3.0$ T were possible.

Because confinement scaling depends on the confinement mode, it becomes important to determine what dimensionless parameter(s) is the key to H-mode scaling. Two candidates are: (i) the presence of an edge transport barrier; or (ii) the magnitude of the density gradient relative to the temperature gradient. The latter parameter meshes with the concept of local turbulence, while an edge criterion that affects core transport scaling is decidedly non-local, but can be realized in a stiff transport model via sensitivity to the edge boundary condition. Observations indicate that the Bohm like or worse ion scaling in L-mode correlates with regions of strong density gradient [336]. If it is a relatively steep density gradient that is responsible for L-mode confinement with Bohm scaling, then this could imply that density gradients introduce long wavelength, trapped ion modes, which would not exhibit scale separation between the equilibrium and the turbulence and would, therefore, yield Bohm scaling for transport. Since ITER will likely have flat core density profiles because of its size, even with an L-mode edge, the influence of the density gradient on confinement scaling must be clarified, particularly in view of the fact that there are several counter examples of steep density gradients with good confinement, e.g. TFTR supershots [337] and the ERS mode [338].

From a non-dimensional scaling perspective a key question is: does ITER need an H-mode transport barrier at the edge to attain gyroBohm core transport scaling?

8. One dimensional transport models

8.1. Introduction

Calculations of the expected fusion power from ITER can be carried out at various levels. The simplest is to use a global energy balance, taking the confinement time τ_E from extrapolating empirical scaling relations, as discussed in Section 6, or employing dimensionally similar scaling studies, as in Section 7. These calculations take some account of profile effects by assuming particular forms (e.g. $T = T_0(1 - r^2/a^2)^{\alpha_T}$, treating α_T as a parameter to be chosen or explored), and specify levels of impurities in terms of a global Z_{eff} and the fraction of He ash using a lifetime τ^*_{He}. The next simplest step would be to use profiles that crudely represent known physics. Thus, one could take n and T flat within the $q = 1$ surface, or the mixing radius, to represent sawtooth effects (see Section 5.1), invoke edge pedestals to represent the H-mode transport barrier (see Section 4.2), and then use a simple, say linear, radial interpolation between; this would produce a trapezoidal shape. A more realistic step would be to use a one dimensional transport model, which contains models for heating due to fusion power and additional heating, losses due to radiation, and sources of particles and impurities, including He ash, with simple empirical forms for particle transport (see Section 9). A semi-empirical approach to such modelling of the energy transport can be employed in which one chooses forms for the radial profiles of χ_i and χ_e that are known to reproduce experimental profiles well, but one fits their overall magnitudes to ensure some particular global scaling expression for τ_E is reproduced; again, models for sawteeth and the H-mode barrier can be added. The ultimate aim of this one

dimensional modelling, however, is to have a complete transport model that predicts both the temperature profile and confinement time. (It is worth noting that profile modelling is not only relevant to energy confinement, but can potentially provide realistic profiles with which to test the MHD stability of ITER.)

Transport models can themselves be subdivided. Both energy and particle transport models can be semi-empirical, in which, while physical ideas like dimensional analysis and critical gradients are employed, the choice of the structure and the magnitude of diffusivities is guided largely by experimental comparisons. The extrapolation to ITER of results using such models is subject to reservations similar to those encountered in extrapolating global scaling laws for τ_E. On the other hand, it is also possible to derive physics based models that permit extrapolation to ITER with more confidence, since they automatically respond to differing conditions; provided that no new phenomena unanticipated by the model appear. Not only does this apply to extrapolation in size for a particular confinement mode (say ELMy H-mode) but, if the physics model is adequate, the same model could simultaneously describe other modes, such as reverse or optimized shear, which might eventually be invoked for ITER. These physics based models can be derived entirely from first principles or contain just a few fitting parameters that arise from estimates in theories that are not quite complete (e.g. turbulence saturation levels). A physics based model that is also capable of providing a good fit to data is an aim of transport modelling activity.

There is a range of transport models that have been proposed and partly tested against various tokamaks. If these are to be used for predicting the performance of ITER, a considerable extrapolation from existing devices, it is important to understand how well they represent as wide a range as possible of existing tokamaks. This has led to the development of the ITER profile database [339], which contains fully analysed profile data, specified in a standardized manner, from many tokamaks and covering a variety of confinement modes. By defining transport models in a standard form, using the same variables as defined in the profile database, and using transport codes that are also written in a standardized form and benchmarked against each other, it is possible to carry out reliable and verifiable testing of transport models. All the resulting modelled profiles are available to each modeller and various 'figures of merit' have been defined to help quantify how successfully each model performs. To avoid the need for a H-mode transport barrier model, still an active research topic, the testing employs an experimental boundary condition for temperatures at $r = 0.9a$. Results of predictive modelling of specified ITER reference cases, which prescribe the edge temperature and the mean density as parameters to be explored, are also available. Predictive codes can also be used to investigate models for the sawtooth cycle (Section 2.5.1) and its impact on confinement and profiles.

8.2. Theoretical and semi-empirical transport models

Within the framework of neoclassical collisional transport theory, it has proved possible to obtain precise expressions for transport fluxes [4, 340, 341] (Section 2). However, most tokamaks experience a level of anomalous transport that exceeds neoclassical values, although the ion neoclassical thermal diffusivity may sometimes play a significant role, particularly in enhanced confinement regimes with transport barriers (modifications to the basic theory to account for such features as the steep gradients in these cases are being developed). This anomalous transport is believed to be caused by the fine scale turbulent fluctuations that are observed in tokamaks. These, in turn, are believed to be the result of the non-linear saturation of various micro-instabilities: electron drift waves, ITG modes, pressure driven ballooning modes, etc. Many estimates (e.g. mixing length ones) of the turbulent transport coefficients associated with these fluctuations have been made over the years [17, 28, 29] (Section 2). Such models, which are inevitably gyroBohm in nature, usually contain a single overall constant available for fitting. Particular models can often capture some of the basic scalings of global confinement. For example, a number of features of ohmic confinement (Section 3.2) result from electron drift wave and ITG models. In the LOC regime, the increase of confinement (and decrease of electron temperature) with increasing density is consistent with a reduction in transport with density due to trapped electron modes [22]. The improved ohmic confinement (IOC) associated with a steeper density gradient has been modelled using ITG models; the ultimate saturation with density has been attributed to ion neoclassical transport [108]. However, these simple models are sometimes challenged by other

experimental results, such as the current scaling, and often fail to predict the correct shape of profiles [342, 343].

The Weiland–Nordman reactive drift wave model [344] is a more complete version of this approach, calculating the whole transport matrix (including impurity fluxes) according to the quasi-linear theory, using a particular mixing length rule; the validity of this approach has been supported by two dimensional fluid mode–mode coupling simulations [345]. Features of this model are the important role of a critical ITG for the excitation of ITG turbulence, and pinch terms due to toroidal geometry. As a result, this model is able to overcome some of the weaknesses above [346–348].

The multi-mode model has evolved from earlier versions [349, 350] and now brings together a version of the Weiland–Nordman model, a resistive ballooning model due to Guzdar and Drake, a kinetic ballooning mode model, and neoclassical transport [351]. The multi-mode model currently treats the κ dependence of the transport coefficients in an empirical manner, guided by global scaling laws. Full profile and global features are reproduced with the multi-mode model, partly as a result of the role played by the resistive ballooning mode contribution, which becomes important near the more resistive plasma edge [350–353]. It is interesting to note that this model, which is inherently gyroBohm, models well the Bohm like L-mode discharges. In the modelling, this is attributed primarily to variations in neutral penetration and edge temperature profiles, which give rise to non-gyroBohm behaviour near the plasma edge.

A particularly sophisticated extension of this physics based approach is the GLF23 model [354, 355], which aims to capture the anomalous transport due to the whole of so-called drift ballooning physics; the only free parameters in this model are chosen by fitting to more detailed theory, not experiment. The model captures many features of tokamak behaviour, including the formation of ITBs. An important step in the development of physics based models is the use of extensive numerical simulations of turbulence to determine the parametric dependence of transport coefficients. The IFS/PPPL model [15, 75] is a leading example of this, combining gyro-fluid simulations of ITG turbulence in a representative thin annular region of the tokamak poloidal cross-section with more complete gyro-kinetic calculation of the critical ITG for instability. The model was first successfully tested on TFTR L-mode dis-

charges. Recent advances in the stabilizing effect of radial electric field shear (see Section 4.1) have led to modifications to the IFS/PPPL model. The GLF23 and IFS/PPPL models, as opposed to the multi-mode model, have the property of being 'stiff', i.e. the thermal diffusivity (due to the ITG turbulence) becomes very large once a critical ITG is exceeded, and this inhibits departure of the ion temperature profile from this marginally stable profile. However, this feature of the GLF23 and IFS/PPPL models is an active research topic. These models are based on gyro-fluid simulations in a local annular region of the plasma cross-section; related simulations using more fundamental, but more computationally challenging, gyro-kinetic simulations predict considerably lower transport. Possible reasons for this discrepancy are: the treatments of poloidal flow damping; particle noise; non-linear wave particle resonances; and linear theory characteristics. Careful cross-checking of these codes is underway addressing these possibilities [356–359]. Results from predictive modelling efforts have indicated that features of the core plasma are well modelled using the ITG mode as a basis for transport there [15, 75, 348–356].

A somewhat different physics based model is the current diffusive ballooning mode (CDBM) model [360]. This is based on a one point renormalization of pressure driven 'resistive MHD' turbulence, but with the important difference that a self-consistent turbulent electron viscosity due to electron inertia replaces collisional resistivity in Ohm's law and sustains the turbulent transport. In this theory, the turbulence has a sub-critical nature, which is supported by direct numerical simulations [361], and the transport is not particularly dependent on the linear instability criterion. The model incorporates effects of a large Shafranov shift in the equilibrium and reflects favourable aspects of ideal MHD ballooning stability: reduced transport for low (or negative) and high magnetic shear and high pressure gradients; transport reductions due to sheared radial electric fields can also be included [362]. The theory involves one undetermined numerical coefficient, which is chosen once and for all to optimize the fit to a dataset. The model has captured satisfactorily the essential features of the ohmic, L-mode, the ITB for the high β_p mode of JT-60U [363], and current profile control by LHCD [364].

One of the challenges for theory based models is to recover the isotope effect observed in experiments (experimentally, confinement often appears to improve with increasing ion mass (Sections 3 and 6)).

Several drift wave based models are gyroBohm in nature and would be expected to predict the opposite effect (Section 2); the models can only predict the observations through some indirect effect (for example, through boundary conditions or a correlation between the density profiles and the isotope employed, which might result as a consequence of different particle fuelling characteristics). However, the stabilizing tendency of the velocity shear on turbulent transport increases with isotopic mass, and this might provide a possible explanation. The CDBM model does have an explicit isotopic dependence, which is in the same direction as that observed.

Another approach to modelling is the semi-empirical one, based on a view that we cannot yet satisfactorily calculate turbulent transport fluxes, or even fully identify the underlying cause. Thus, expressions for these are proposed that embody theoretical concepts like dimensional analysis and critical gradients, but whose particular form is partly influenced by experimental evidence. Thus the gyroBohm Rebut–Lallia–Watkins (RLW) model [365] is based conceptually on the excitation of microscopic magnetic islands when a critical electron temperature gradient is exceeded, but is tuned to describe a wide range of experimental results from JET. This has been modified by Boucher (RLWB) to contain Bohm like ion transport in the light of evidence for the Bohm like scaling in L-mode. The Culham model is influenced by ideas from collisionless skin depth [366] and pressure driven turbulence, and is constructed to represent a number of L-mode discharges from an early version of the ITER profile database. Taroni and co-workers [367] have devised the so-called mixed model, a combination of simple Bohm and gyroBohm terms suggested by drift wave driven transport, with the Bohm term containing a non-local element that responds to edge conditions. In this way, it is able to describe a diversity of steady and transient experiments on JET. This model has been modified to the mixed shear model by Romanelli and co-workers [368, 369] to embody theoretical predictions that the Bohm contribution will be reduced for low magnetic shear. The T-11 model contains a combination of ion neoclassical transport and a gyroBohm electron term suggested by experimental studies on the T-11 tokamak, but which is also close to the transport expected from fluctuations on the collisionless skin depth scale [107]. Recent extensions to include anomalous ion transport guided by dimensional analysis (uniquely, in that it allows the Debye length to enter) and experiment have led to the

semiempirical transport (SET) model [370]. Finally, we mention the canonical profiles transport model (CPTM), which contains a combination of empirical background anomalous transport and additional terms that tend to force the profiles back to so-called 'canonical' ones suggested by MHD energy minimization arguments [371].

All the models above, which are representative of models available in the fusion literature, are being actively tested against the ITER profile database at present, at least as far as energy transport is concerned (particle transport is discussed briefly below and in Section 9). It is to be anticipated they will develop further in the light of further research and it is desirable that future (and indeed other existing) models be similarly tested.

Complete modelling of a discharge requires transport equations for temperature and particles, valid across the whole plasma profile. While some models (e.g. the multi-mode model) prescribe the particle transport, a number of the above models do not; in this latter case experimental density profiles are taken. However, some general theoretical arguments for the density profile can be advanced [372]. Thus, in the presence of low frequency ionic turbulence, the electrons, particularly the trapped ones, diffuse conserving their adiabatic invariants: μ, the magnetic moment; and J, the longitudinal invariant. The implication of this is that, if particle sources are weak, the electron density takes up a 'canonical' profile that is peaked on axis: the degree of peaking depends on the relative responses of trapped and passing electrons to the turbulence. Calculations [373] show that, for an ITER like magnetic geometry, $n_e(0) \sim 1.5 n_e(ped)$, if only trapped particles respond; alternatively, using a ratio for this relative response that fits DIII-D data, one finds $n_e(0) \sim 2 n_e(ped)$ (here $n_e(ped)$ is the density at the top of the H-mode edge density transport barrier).

Since not all models attempt to model the edge region and H-mode barrier (say, $r > 0.9a$) at the moment, or the central sawtooth region (say $r < 0.2a$), testing is restricted to $0.2a < r < 0.9a$. Thus, it has been agreed to prescribe the experimental temperature at $r = 0.9a$ as a boundary condition for the models. However, some models do represent the edge region (e.g. multi-mode [350, 351]), and others contain an explicit H-mode barrier model (e.g. [367] involves a narrow neoclassical layer); the inclusion of this physics is necessary if one is to give a first principles transport model for the H-mode. Some transport models contain relatively simple sawtooth

models (e.g. periodic Kadomtsev mixing within the sawtooth region, as in the Culham model [366]), but others have proposed prescriptions for the sawtooth period based on MHD stability criteria and rules for its periodic effect on the profiles based on reconnection and relaxation ideas [290,374,375] (Section 5.1). It is interesting that including the stabilizing effect of alpha particles allows a long period for the sawtooth ($\sim$100 s), leading to 'monster' sawteeth [290].

8.3. Plasma profile database

The ITER profile database is being developed to provide a facility for testing and developing transport models against reliable, well documented data in an open and verifiable manner [339, 376]. One objective of the database is, therefore, to provide all the profile and global data required for comparing transport predictions with experimental observations in a readily accessible form. By September 1997, 141 discharges from nine tokamaks were available from the database. These discharges are not all up to the same standard: limited diagnostic capability prevented some tokamaks from providing all the necessary information; the safety factor (q) and effective charge (Z_{eff}) are notoriously difficult to provide. As a consequence, the descriptions of the discharges are still evolving with time as more information is made available.

The choice of discharges provided in the profile database results from a balance between the need to cover as wide a range in plasma parameters as possible – tokamak sizes and range of parameters within each tokamak – and the need to include discharges that emphasize a specific transport phenomena, such as cold pulse experiments, reversed central shear configurations, supershots or parameter scans. A brief summary of the discharges available in the database is given in Table 9.

8.4. Results of one dimensional modelling tests

The existence of the ITER profile database (Section 8.3) provides an opportunity to carry out extensive and verifiable testing of transport models such as those described in Section 8.2. Table 10 displays models and modellers who have placed simulations on the ITER profile database. A large variety of transport codes using various procedures – ranging from fully predictive (sources/sinks computed by the code) to fully interpretive (sources/sinks taken from the database) – have been used to test the models

against experiments. Because of the different implicit assumptions made by these codes, the model testing outputs were found to depend on the particular transport code being used. To overcome this difficulty, a standard procedure has been defined and used as a reference. This standard procedure prescribes a reference set of transport equations and standard inputs (sources and sinks) to these equations. The models themselves have been standardized by specifying exactly how each quantity entering in the model expressions is to be made consistent with the standard equations and inputs. The procedure has been implemented in three different transport codes to ensure that the tests of the models were indeed totally transport code independent.

A standard subset of discharges that are relevant to ITER operation (i.e. L-mode and ELMy H-mode) and have all necessary variables properly available in the database, has been defined. It consists of 55 discharges from four tokamaks (JET, DIII-D, TFTR, JT-60U). To check that the standard transport equations have been properly implemented, two types of benchmarking have been carried out. In the first place, the results have been compared with a set of analytic solutions to the transport equations, using an artificial model $\chi = n_e(0)/n_e$, by Mikkelsen; the maximum error is less than 0.5% from both SMC, the standard code of Boucher, and the HYPED code. Secondly, the results from separate codes (e.g. the MLT code of Waltz, the SMC code and the HYPED code) using another artificial model $\chi = 1\,\mathrm{m^2\cdot s^{-1}}$ and a special benchmark dataset have been compared. Finally, the predictions of the codes for the models discussed in Section 8.2 have been calculated for the standard dataset and placed on the ITER profile database server.

Analysis software is also available on this server to generate the various figures of merit for testing models shown in Table 11. We have chosen to concentrate on

(i) figure of merit 1 in Table 11, which represents the ability of the models to simulate the experimental energy contents W (we present comparisons for the total energies above the edge pedestal, i.e. the 'incremental' energies W^{inc}, since the pedestal energy is an input through the edge boundary condition and is particularly important for H-modes); and

(ii) figure of merit 6a in Table 11, which represents the distance between the modelled and simulated electron or ion temperatures profiles

Table 9. Database discharges

Tokamak	R/a (m)	Heating (MW)	Field (T)	Current (MA)	Phase[1]	Comments
Alcator C-MOD	0.67/0.22	ICRH 0–2.5	5.2	0.8–1.0	L, H, HSELM	High magnetic field
DIII-D	1.69/0.63	NBI 0–15	1.0–2.0	0.5–2.0	L, HSELM	Scans: temperature, density, elongation, ρ^*
JET	3.0/1.1	NBI 0–18	1.0–3.2	1.0–3.0	L, HSELM, Hot ion H	Scans: ρ^*, β, ν^*
JT-60U	3.2/0.89	NBI 5–23	2.4–4.2	1.0–3.5	L, Hot ion H	
TFTR	2.5/0.87	NBI 4–36	2.1–5.5	0.8–2.3	L, ERS, H, Supershot	Impurity injection: Xenon, krypton scans: current, ρ^*, β, ν^*, power Comparison between DD and DT discharges Cold pulses experiments.
RTP	0.72/0.16	ECH 0–0.35	2.2	0.077	Ohmic, L	Hollow T_e profile
T-10	1.5/0.32	ECH 0–1.7	2.8	0.2–0.4	Ohmic, L	
TEXTOR	1.75/0.46	NBI 2.8	2.25	0.4	L, RI-mode	Transition RI-mode to L-mode
TORE-SUPRA	2.3/0.7	ICRH 2.8	2.2	0.4	L	Enhanced performance mode

[1]L, L-mode; H, ELM free H-mode; HSELM, ELMy H-mode (small ELMs); ERS, enhanced reversed shear.

(this is taken over the 'transport region' $0.2 < \rho < 0.9$, where ρ is the normalized toroidal flux excluding the sawtooth region and the edge region, where additional transport mechanisms might need to be incorporated in some of the models).

The results are displayed in Figs 16–19. Figures 16 and 17 show the mean and the mean square deviations of the predictions for W^{inc} from each transport model, expressed as

$$\langle R_w \rangle = \frac{1}{N} \sum \left(\frac{W^{inc}_{sim}}{W^{inc}_{exp}} - 1 \right)$$

and

$$\Delta R_w = \sqrt{\frac{1}{N} \sum \left(\frac{W^{inc}_{sim}}{W^{inc}_{exp}} - 1 \right)^2}$$

where N = number of discharges modelled, displaying them separately for (i) H-modes with giant ELMs

(HGELM); (ii) H-modes with small ELMs (HSELM); and (iii) L-modes from the standard dataset. The standard dataset comprises 3 HGELM, 14 HSELM and 38 L-mode discharges. Standard code results for all of these discharges are not yet available for all models, as shown in Table 12. Each entry in the figures for a given model corresponds to an average over the results from the standard codes for each discharge and then averaged over the discharges modelled. (However, in the case of the Weiland and T-11/SET models, no standard code results were available so the modeller's own results were used. For the multi-mode model an average of standard code results and those from the authors' own modelling with the BALDUR code were employed.) Figures 18 and 19 show equivalent results for STD(T_e) and STD(T_i), respectively.

On the basis of these tests it would appear that the multi-mode and the IFS/PPPL $\boldsymbol{E} \times \boldsymbol{B}$ models

Table 10. Models and modellers

Model	Modeller	Physics
Weiland	J. Weiland (EU), D. Mikkelsen (US), R. Waltz (US)	ITG
Multi-mode	J. Kinsey (US), G. Bateman (US), D. Mikkelsen (US)	Drift waves, RBM, kinetic ballooning, neoclassical
Waltz GLF23	R. Waltz (US), J. Kinsey (US)	ITG
IFS/PPPL, no $\boldsymbol{E} \times \boldsymbol{B}$; IFS/PPPL, $\boldsymbol{E} \times \boldsymbol{B}$	M. Turner (EU), S. Attenberger (US), B. Dorland (US), D. Mikkelsen (US), R. Waltz (US), Y. Ogawa (JA), D. Boucher (JCT)	ITG
CDBM	A. Fukuyama (JA), S. Attenberger (US), D. Mikkelsen, R. Waltz (US), D. Boucher (JCT), J. Kinsey (US), Y. Ogawa (JA)	Current diffusive ballooning modes
RLWB, RLW	D. Mikkelsen (US), D. Boucher (JCT)	Semi-empirical
Culham	M. Turner (EU), S. Attenberger (US), D. Boucher (JCT)	Semi-empirical
Mixed	A. Taroni (EU)	Semi-empirical
Mixed-shear	G. Vlad/M. Marinucci (EU), D. Boucher (JCT), Y. Ogawa (JA)	Semi-empirical
T-11/SET	A. Polevoi (RF)	Semi-empirical
CPTM	Yu. Dnestrovskij (RF)	Semi-empirical

Table 11. Figures of merit

1: Ratio of incremental total stored energy:
$W_{sim}^{inc}/W_{exp}^{inc}$, where $W^{inc} = \sum \frac{3}{2}(n_e \tilde{T}_e + n_i \tilde{T}_i)dV$
and $T^f(\rho) = T(\rho) - T(0.9)$

2: $(W_{sim}^{inc}/W_{exp}^{inc})_e$ and $(W_{sim}^{inc}/W_{exp}^{inc})_i$ (separating e and i)

3: $[\{(n_{i,\rho=0.3}T_{i,\rho=0.3}W)_s\}/\{(n_{i,\rho=0.3}T_{i,\rho=0.3}W)_x\}]$

4: $\chi^2 = \sum[(T_s - T_x)^2/N\sigma^2]$, where σ is the experimental error and N the number of observations

5: $\beta_s^{*2}/\beta_x^{*2}$, where $\beta^{*2} = \sum n_i^2 T_i^2 dV$

6a: STD $= [(\sqrt{\sum(T_s - T_x)^2})/(\sqrt{\sum T_x^2})]$,

6b: OFF $= [(\sum(T_s - T_x))/(\sqrt{\sum T_x^2})]$ for electrons and ions separately.

perform the best from amongst the physics based models; both predict incremental stored energy to an accuracy of within 24% overall. (Simulations with the multi-mode model using the BALDUR code give slightly better predictions with an accuracy of within 22%.) Of these, the multi-mode model gives a better prediction for the electron temperature profiles with an average STD value of 13%, as against 25% for the IFS/PPPL $\boldsymbol{E} \times \boldsymbol{B}$ model, but both perform equally well in the prediction of ion temperature profiles with an STD value of 18% overall. However, several of the semi-empirical models are competitive with these two physics based models, particularly the mixed shear and Culham models with accuracies of 26% for the predictions of the incremental stored energy. It could be that uncertainties in experimental inputs could generate discrepancies of these magnitudes. We note that some credit might be given to a model on the grounds that it is physics based, particularly if it is able to correctly predict results in other regimes, such as reversed shear, without modifications to the model. Such a model can improve its performance

Table 12. Number of discharges from standard dataset used in testing of each model

Model	H-mode with giant ELMs	H-mode with small ELMs	L-Mode	All
Weiland	1	5	3	9
Multi-mode	3	14	25	42
GLF23	3	14	30	47
IFS/PPPL no $\boldsymbol{E} \times \boldsymbol{B}$	3	14	38	55
IFS/PPPL $\boldsymbol{E} \times \boldsymbol{B}$	2	14	34	50
CDBM	3	14	38	55
RLW	3	14	38	55
RLWB	3	14	38	55
Culham	3	14	38	55
Mixed-shear	3	14	38	55
T-11/SET	0	13	14	27

by artificially adjusting its coefficients in the thermal diffusivities. For instance, the GLF23 model achieved a reduction in the mean square deviation on a 46 discharge subset of the database from 26.9% to 19.6% using such a recalibration. The CDBM model has a single overall constant multiplier, which is to be chosen to provide the best fit to the data; a renormalization of this model could clearly improve its performance. In fact, a consequence of this modelling exercise using the ITER profile database is that some of the semi-empirical models have evolved, improving their performance in the process.

The testing procedure described above has not yet proved decisive in choosing preferred models. It was the simplest and most direct exercise that could be attempted to complement the global database activity in support of ITER. The true value of the investment in the profile database is that it will facilitate physics based investigations: specific scaling studies on ρ^*, ν^*, β, flow shear, T_e/T_i, etc., on the one hand, and comparisons with perturbative and transient experiments on the other. For example, there is a proposal on DIII-D to compare models with pulsed localized ECH experiments that will test the stiffness of models such as the IFS/PPPL one. The discharges supplied by TFTR provide a number of cases involving perturbative data for such tests.

8.5. Predictions of transport models for ITER

The use of local transport models can effectively complement the two methods detailed earlier in this chapter: global confinement scaling expressions and non-dimensionally similar discharges, by providing additional information such as temperature profiles,
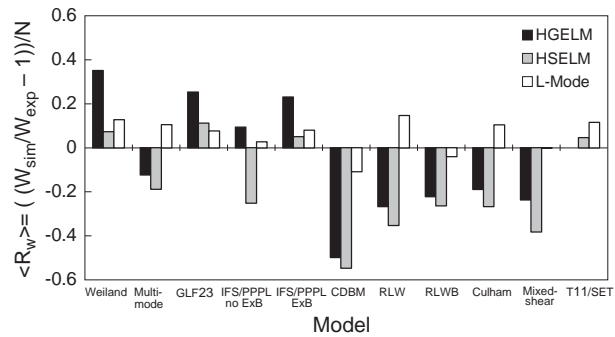
Figure 16. Ratio of simulated to experimental incremental stored energy using figure of merit 1.
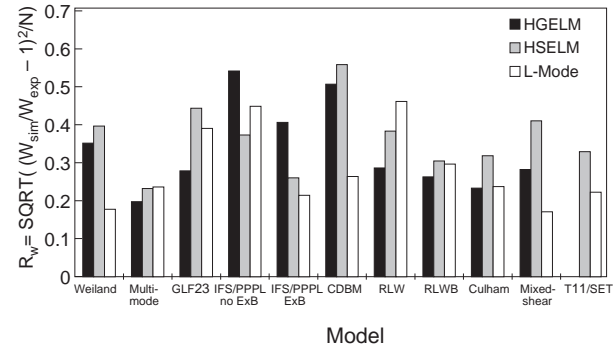
Figure 17. Mean square deviation of the ratio of simulated to experimental incremental stored energy using figure of merit 1.

the ratio between ions and electrons transport ultimately determining the ratio T_i/T_e, and the determination of the total fusion power consistently with heat and particle sources and sinks.

The transport models presented in this document, however, are still evolving or are not necessarily suitable for extrapolation to ITER. The
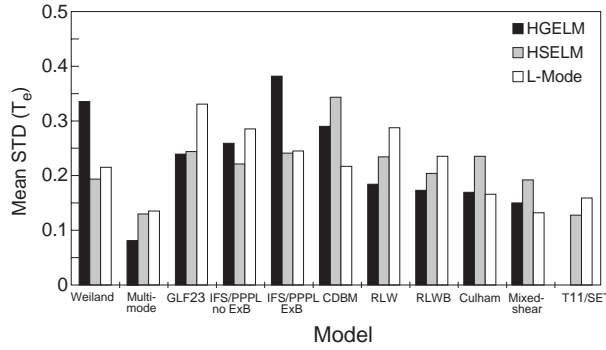
Figure 18. Distance between modelled and experimental electron temperature profiles using figure of merit 6a.
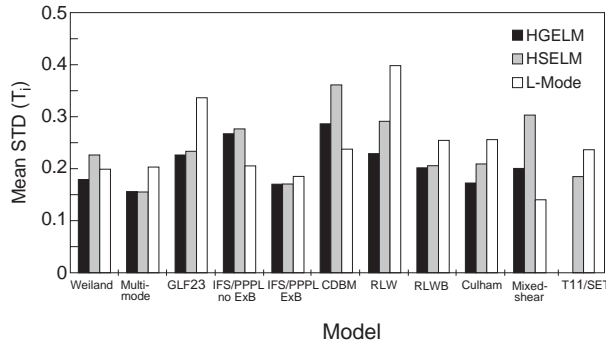

Figure 19. Distance between modelled and experimental ion temperature profiles using figure of merit 6a.

RLWB model, for instance, was essentially developed to fit L-mode discharges using a purely Bohm like ion transport, which would not be suitable for an ELMy H-mode regime that exhibits gyroBohm scaling. Other empirical models, which by definition include adjustable parameters, have not yet been fully calibrated against the experimental data – as is visible on Fig. 16 – without this necessary step, the predictions of fusion power in ITER are premature.

Extrapolations are more meaningful, however, with transport models such as the multi-mode model, which has been carefully fitted against experiments and models without adjustable parameters such as IFS/PPPL and GLF23. But in this latter case, as well as fitting against experiments, the models need to be fitted against the most accurate numerical turbulence simulations if they are to be used as valid predictors of the transport level predicted by theory. The independent work from the Cyclone group [356] indicates that this might not be the case.

Nevertheless, as a guide toward the further development of these transport models, empirical or theory based, it is instructive to study their prediction of ITER fusion power performance.

Since most of the models being tested address energy transport and not particle transport or the physics of the transport barrier in H-mode, a set of ITER target density and current profiles and boundary conditions has been prepared to allow the comparison of ITER predictions using the various models in an objective fashion and with the same input parameters. To simplify the testing procedure and facilitate the comparisons between models, the range of the scanning parameters was reduced to $\tau_{He}^*/\tau_E = 10$, $P_{aux} = 100$ MW, $\langle n_e \rangle = 1.5 n_{GW}$ where n_{GW} is the Greenwald density ($n_{GW} = 8.5 \times 10^{19}$ m^{-3} at 21 MA), and values of $T(0.9)$ were chosen to cover a wide range: from 1 keV to 5 keV. Figure 20 summarizes the range of the fusion power predicted by a representative set of models both empirical and theory based. Not surprisingly, at this early stage of model testing and calibration, the range is large: about of factor 6 between extremes. The multi-mode model prediction is very close to the reference fusion power found independently using global scaling expressions for energy confinement time. The models based on gyro-fluid numerical treatment of electrostatic turbulence occupy the lower range and predict a similar amount of fusion power. The multi-mode model, although also based on similar drift wave electrostatic turbulence and giving a better fit to experimental data, predicts about three times the fusion power. This higher level of fusion power, quite in line with other independent projections, is also found in general if one uses the more complete gyro-kinetic numerical simulation of drift wave electrostatic turbulence [356].
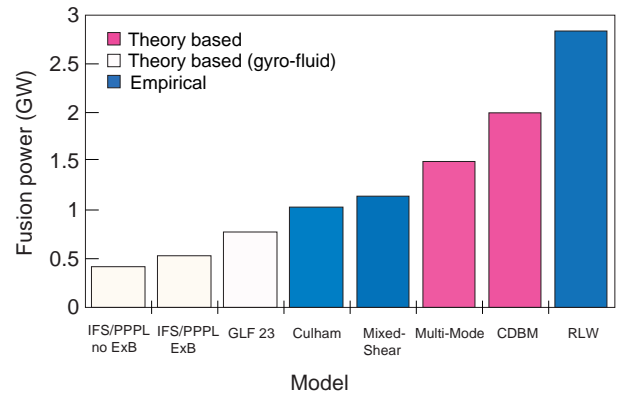

Figure 20. Fusion power predicted by various models with an edge temperature $T(0.9) = 3$ keV.

An important aspect of the fusion power predictions is their sensitivity to the assumed edge temperature. Figure 21 illustrates how the predicted fusion power – normalized for clarity independently for each

model to its value at $T(0.9) = 3$ keV – varies with the edge temperature as it is varied from 1 to 5 keV.

Combining the fusion power predictions from Fig. 20 and the edge dependence of Fig. 21, one can deduce what edge temperature would be required for each model in order to achieve a given fusion power: 1.0 or 1.5 GW. Figure 22 indicates that, despite the wide disparity between models, an edge temperature up to 4 keV would ensure at least 1.0 GW ($Q = 10$) from all models, with the exception of the original version of the IFS/PPPL model that did not take $\boldsymbol{E} \times \boldsymbol{B}$ stabilization into account. An edge temperature up to 5 keV would ensure 1.5 GW ($Q = 15$).
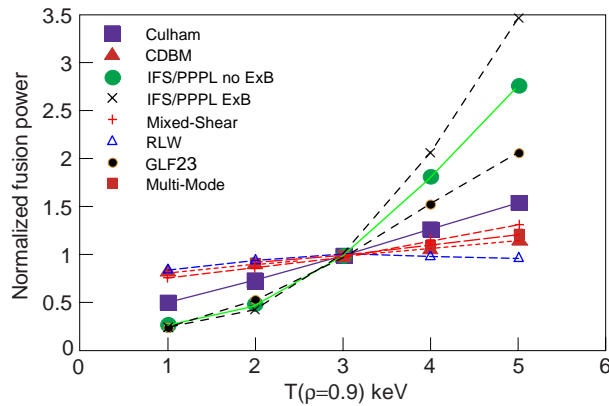

Figure 21. Relative sensitivity of the predicted fusion power to the edge temperature. The fusion power is normalized, independently for each model, to its value at $T(0.9) = 3$ keV.
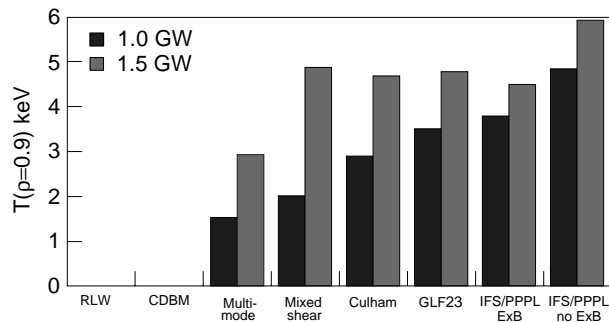

Figure 22. Edge temperature in keV at $\rho = 0.9$ required to achieved a given fusion power, 1.0 or 1.5 GW, for each transport model. RLW and CDBM would achieve the fusion power for any value of the edge temperature.

The fusion power predictions for local transport models come from a combination of dominant factors: the edge temperature, the magnitude of the transport coefficient – χ_e and χ_i – in the core, and, finally, the shape of these coefficients. To study the influence of the shapes and, therefore, the impact

on fusion performance of the temperature profiles, one can define the quantity $[T_i(\rho) - T_i(0.9)]/\langle T_i(\rho) - T_i(0.9) \rangle$, which represents the normalized ion temperature profile inside ρ of 0.9. Figure 23 plots this quantity for the various models.

Despite self-consistent calculation of sources and sinks, the normalized profiles are remarkably close, with the exceptions of the CDBM and mixed shear models, whose central peaking can be attributed to the weak shear inside the $q = 1$ surface assumed in the target safety factor profiles. Nevertheless, if one computes the fusion power that would be produced from these shapes – after imposing $T(0.9) = 3$ keV and forcing all profiles to correspond to the same 12 keV volume average temperature – it is found that it would differ by less than 10% between extremes.
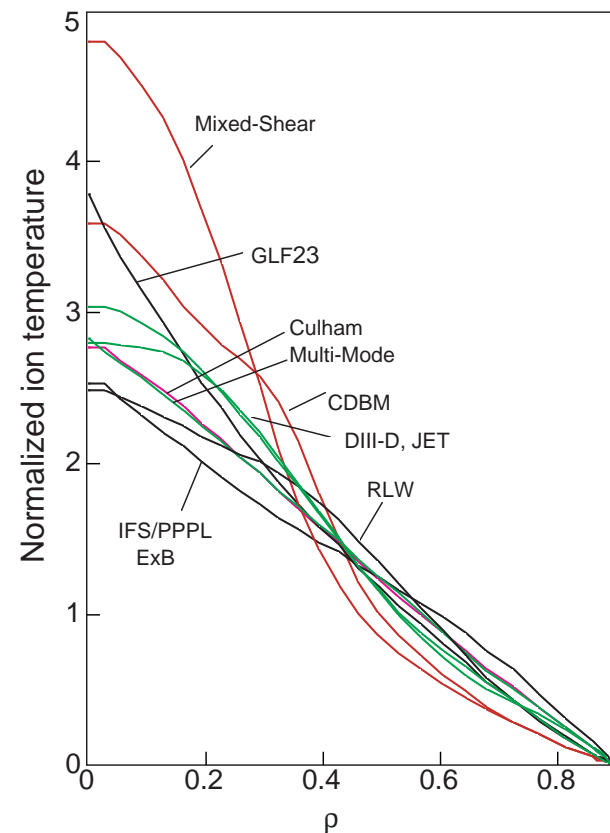

Figure 23. Normalized ion temperature profiles, $[T_i(\rho) - T_i(0.9)]/\langle T_i(\rho) - T_i(0.9) \rangle$, compared between various local transport models and for DIII-D and JET ITER demonstration discharges.

In conclusion, the incomplete nature of the calibration of the models, either against experiments for empirical models or against detailed numerical turbulence simulations for theory based models, makes the prediction of fusion power in ITER from the

models still premature. Nevertheless, a number of conclusion can be drawn: the multi-mode model, which gave the best fit to experimental data, predicts a fusion power for ITER close to that independently predicted by global scaling expressions. An edge temperature, at $\rho = 0.9$, above 4 keV is consistent with more than 1.0 GW of fusion power from all models considered, the IFS/PPPL model without $\boldsymbol{E} \times \boldsymbol{B}$ correction being about 20% lower.

'Stiff' models, such as IFS/PPPL or GLF23, are found to be very sensitive to the edge temperature, with the fusion power increasing by about a factor of 4 when the temperature is raised from 2 to 4 keV. Clearly, a reduction of both sources of uncertainties – edge temperature scaling and treatment of drift ballooning driven turbulence – are required before such model predictions can be relied upon for estimation of the fusion power in the ELMy H-mode in ITER.

9. Particle transport: hydrogen, helium, impurities

While most attention has been focused on energy transport, issues of particle transport also impact the design of the ITER device. In particular, the design and operation of the fuelling and pumping systems will depend on the anticipated transport properties of the fuel species, helium ash and impurities.

A key factor determining performance projections for ITER is the fraction of helium ash accumulation during long pulse or steady state operation. The primary effect is dilution of the fuel and reduction of the fusion power. The impact of helium ash can be quantified in terms of the simple ratio of the effective helium particle confinement time to the global energy confinement time, τ_{He}^*/τ_E, where τ_{He}^* takes into account finite recycling and helium pumping; that is

$$\tau_{He}^* = \tau_{He}/(1 - R_{eff}) \qquad (30)$$

where τ_{He} is the particle confinement time for helium nuclei, and R_{eff} is the effective recycling coefficient (<1) to the core plasma. Steady state ignited solutions exist only for values of the ratio $\eta = \tau_{He}^*/\tau_E < \eta_{crit}$, where η_{crit} is a number of order 10. A full derivation has been given by Reiter [377, 378]; here we will merely sketch the main ideas of that derivation.

The key point is that the fusion power production rate and the helium production rate are exactly proportional to each other. Therefore, we can write the power balance and helium particle balance each in terms of the usual fusion parameter $n_e\tau_E$ so that the ignition condition can be written as

$$\frac{3}{2}\frac{n_e(1 + f_i + f_z + f_{He})T}{\tau_E} = \tfrac{1}{4}n_i^2\langle\sigma\nu\rangle E_\alpha - n_e^2 R_{rad} \qquad (31)$$

where $f_i = n_i/n_e$ is the fraction of hydrogenic species, $f_{He} = n_{He}/n_e$ is the helium fraction, f_Z is the fraction of other impurities, E_α is the alpha particle energy, $\langle\sigma\nu\rangle$ is the DT fusion reaction rate, and R_{rad} is the radiation cooling rate from all species. Here we have simplified the problem by taking $n_D = n_T = n_i/2$, and by neglecting spatial profiles of n and T. Considering only a single, low-Z impurity, the charge neutrality condition becomes $1 = f_i + Zf_Z + 2f_{He}$. In the same terms, the helium particle balance becomes

$$f_{He} = n_e\tau_E(\tfrac{1}{4}\langle\sigma\nu\rangle)f_i^2\eta. \qquad (32)$$

Using the charge neutrality condition to eliminate f_i and equating the two expressions for $n_e\tau_E$, we obtain a cubic equation for f_{He} involving η, T and f_Z. On substituting back the physically relevant solutions, we obtain ignition loci in the $n_e\tau_E$–T plane, with the ratio $\eta = \tau_{He}^*/\tau_E$ as a parameter [377]. These loci exist and form closed contours only for values of η less than some number of order 10, the precise value depending on assumptions about the impurity concentration and profile effects.

From the above discussion, the important quantity is τ_{He}^*/τ_E, which depends on both the core particle transport properties and the pumping efficiency. Experimental studies with injected helium have demonstrated that satisfactory values of this ratio can be obtained in present tokamaks in L-mode [379–382], supershots [382], and in ELMy H-mode [128]. Expectations of efficient helium ash removal in supershots were confirmed with recent measurements of helium ash production and pumping in TFTR DT plasmas [383]. In the ELMy attached divertor experiments, helium was introduced into an H-mode discharge by gas puffing, and the concentration in the core measured by charge exchange recombination spectroscopy. Pumping was accomplished by means of an in vessel cryopump conditioned with argon frost. Values of τ_{He}^*/τ_E between 8 and 10 were inferred from these measurements. The shape of the helium profile remained essentially unchanged during the active pumping phase, indicating that the effective exhaust of helium from the core is limited

by the pumping speed and not by core He transport. Modelling using the MIST code [384] indicates a best fit to the data using a time dependent effective recycling coefficient for helium with a starting value $R_{He} = 0.95$ and a spatially varying diffusivity in the range $0.5 \leq D \leq 1.75 \, \mathrm{m^2 \cdot s^{-1}}$. It is reported that over a range of ELMing discharges in DIII-D the inferred value of τ_{He}^*/τ_E is in the range of 10–20. Values of τ_{He}^*/τ_E between 6 and 8 are also reported with enhanced wall pumping in high-β_p ELMy H-mode on JT-60U [385]. These results are encouraging for ITER. By contrast, experiments in ELM free H-mode discharges in TEXTOR [386] indicate ratios of $\tau_{He}^*/\tau_E \approx 70$, which would not be acceptable. This result emphasizes the importance of the confinement regime and coupling to the pumping system in determining the performance. Helium pumping has been demonstrated in completely detached H-mode experiments in ASDEX-Upgrade, in which feedback controlled neon injection was used to create a steady detached plasma with type III ELMs [387]. However, in ASDEX-Upgrade, the divertor and pumping geometry (outboard turbomolecular pumping) differs from the ITER design (pumping from the private flux region) and the core impurity concentration was unacceptably high.

Transport of intrinsic or injected impurities of higher charge is also of critical importance to ITER. Although a strongly radiating boundary would be a desirable means of distributing plasma power losses, such a boundary leads to the potential danger of excessive core radiation and fuel dilution if impurities tend to accumulate in the core. Perhaps because of the availability of spectroscopic techniques, studies of impurity transport have been carried out for a long time, and, in some respects, it is better characterized than majority transport. The workhorse technique is laser blow-off [388], which uses a high power laser pulse incident on a target material, usually in the form of a thin film, to create a population of energetic neutrals directed toward the plasma. Spectroscopic techniques are used to follow the impurities into and back out of the discharge. Codes such as MIST [384] may be employed to model the atomic physics and transport phenomena. A scaling for impurity confinement time in ohmic plasmas [389], which fits data from a number of early experiments, is

$$\tau_{imp} \, (\mathrm{s}) = 0.75 a R^{3/4} (Z_{eff}/q)(m_{bg}/Z_{bg}) \qquad (33)$$

where R (m) is the major radius, a (m) is the minor radius, q is the safety factor and m_{bg} and Z_{bg} are the mass number and charge of the background (major-

ity) species. The impurity transport appears to be independent of the impurity species, and, somewhat surprisingly, of the target density. Studies of impurity confinement in JET and Tore-Supra [390] found that Eq. (33) yields an impurity confinement time that is much too large for those devices, and proposed the alternate scaling for ohmic and L-mode plasmas

$$\tau_{imp} = 7.4 V_p^{0.70} I_p^{0.31} (P_{in}/n_e)^{-0.57} \, (\mathrm{s}) \qquad (34)$$

where V_p (m^3) is the plasma volume, I_p (MA) is the plasma current, P_{in} (MW) is the ohmic plus auxiliary heating power, and n_e (m^{-3}) is the volume averaged electron density. In H-mode and other improved energy confinement regimes, impurity confinement is also improved. These improvements are not easy to capture in global scaling relationships. Considerations of gross particle confinement time provide the coarsest representation of particle transport phenomena. For more detailed performance projections, which rely on profiles of reacting species and impurities, it is necessary to consider the local transport properties (although sawteeth and ELMs can produce more macroscopic effects, as discussed in Section 5). The simplest useful characterization of local transport in tokamak plasmas identifies the local particle flux as a combination of a diffusive term and a 'pinch' term. A simple example, using a fixed radial form for the relationship between the pinch and diffusive terms, is

$$\Gamma = -D\nabla n + nV = -D(\nabla n + C_v n 2r/a^2) \qquad (35)$$

where D and V are each supposed to be functions of local plasma parameters. Here, the velocity V is a convenient way of representing those components of the particle flux that are not driven directly by the particle gradient; this notational simplification conceals substantial physics, some aspects of which are better understood than others. The most common example of such an off-diagonal transport flux is the so-called neoclassical pinch [4], which is an (inward) particle flux driven by the parallel electric field. Other terms, more difficult to interpret, may arise in the form of particle fluxes driven by temperature gradients.

Experimentally, studies of local particle transport rely on two sorts of measurement: quasi-steady flux balance analysis and perturbative (transient) techniques. From quasi-steady profile analysis, we can, at best, determine only the (perhaps spatially varying) ratio C_v of transport coefficients in Eq. (35). Determination of both coefficients requires analysis

of the time response of the system, using perturbative techniques. These may rely on intrinsic perturbations, such as sawteeth or ELMs, or on active methods such as oscillating gas puffs, pellet injection, or, in the case of impurity transport, laser blow-off. Numerous examples [391–399] of such experiments, and associated analyses, exist in the literature.

Despite the large number of experiments, a clear description of majority species particle transport in tokamaks has not emerged; indeed, the level of consistency with respect to particle transport appears to be even less than that which typifies the energy transport problem. Nevertheless, some general observations can be made. Many experiments indicate an inward pinch in the outer region of the core that is coupled with a high diffusivity in order to reproduce the dynamics of the plasma density evolution for $r/a \geq 0.7$. However, in this region, the error bars are large because of uncertainties in the sources. The presence of ELMs further complicates edge particle transport analysis. Deeper in the core, the evidence for a particle pinch is mixed. In most larger devices, which may be more relevant to ITER, analysis of density transients indicates that the particle pinch is extremely small and not inconsistent with the neoclassical value. For example, measurement of the DT neutron generation profile in TFTR tritium injection in supershots [400] has provided a first and unique determination of the local transport properties of hydrogenic species. The results indicate a negligible anomalous pinch in the core.

Typically, but not always, D exhibits an inverse dependence on density. A strong temperature dependence of the electron particle fluxes was found in a temperature scan at constant density in TFTR L-mode plasmas [401]. Both D and V typically increase in magnitude toward the edge of the plasma. As the density limit is approached, both D and V exhibit dramatic increases, particularly in the outer region of the plasma. Pellet injection experiments [92] indicate that fuelling beyond this edge layer increases fuelling efficiency dramatically and can lead to density limits that are higher than achieved with gas injection or high recycling. However, further pellet experiments in conjunction with active divertor pumping are needed to clarify the roles of the fuel source, recycling and edge transport properties for ITER projections. The dependence of effective particle confinement on the source distribution (e.g. pellets or gas) is important for plasma density and fuel isotopic control [402].

Experiments indicate a strong correlation between local thermal and particle transport properties in the core plasma, with the particle diffusivity more closely aligned with the ion thermal diffusivity. Ratios of χ/D vary, but in DIII-D, χ_{eff}/D is reported to be typically of order unity in both L-mode and H-mode, as shown in Fig. 24 [187]. In TFTR L-modes and supershots, He diffusivities were comparable to, and correlated with, the ion thermal diffusivity [401]. The T (tritium) diffusivity was also comparable to the ion thermal conductivity in supershots [401]. In Alcator C-Mod $\chi_e/D \sim 1$–2 in L-mode [403]. In JET L-mode plasmas, the local diffusivity of impurities is strongly decreased in the core where the dimensionless shear parameter, $s = d(\ln q)/d(\ln r)$, drops below 0.5 [404]. Enhanced confinement mode operation often results in enhanced fuel and impurity confinement. Injection into ELMy H-mode discharges in Alcator C-Mod resulted in impurity particle confinement times of a few hundred ms, compared to typically 20 ms in L-mode. In ELM free H-mode discharges, impurity confinement times are even longer than in the ELMy case. While the impurity transport in L-mode is consistent with purely diffusive behaviour, with $D_{imp} \sim 0.5 \, \mathrm{m^2 \cdot s^{-1}}$, the H-mode transport is characterized by greatly reduced D_{imp}, especially in the outer portion of the plasma, and a strong inward convection; the edge particle transport coefficients are comparable to neoclassical values [405]. In PEP mode discharges in the same device, impurity accumulation consistent with neoclassical transport was observed, with inferred diffusivities $D_{imp} \approx 0.25 \, \mathrm{m^2 \cdot s^{-1}}$ (about a factor of 2 below D_e), and pinch velocity at the half radius up to $30 \, \mathrm{m \cdot s^{-1}}$, or about an order of magnitude larger than the electron velocity V_e. Neoclassical impurity transport was inferred following pellet injection on Alcator C [406]. In reverse shear plasmas [6], particle transport can also be reduced to neoclassical levels in the core.

For the purpose of modelling ITER discharges, it is recommended that a reference particle diffusivity similar to the ion thermal diffusivity $D^{an}/\chi_i^{an} \sim 1$ be used, with D^{an} independent of charge or mass for fuel, He and low-Z impurities (e.g. Be). The implications of D^{an}/χ_i^{an} as low as 0.3 should be considered for its impact on the design of the fuelling and pumping systems. However, because the relevant factor in He accumulation is D/χ_{eff}, a small value of D/χ_e may lead to deleterious accumulation of He in enhanced confinement regimes, where the ion conductivity and particle diffusivity are selectively reduced. In the edge region, $0.7 \leq r/a \leq 1.0$,
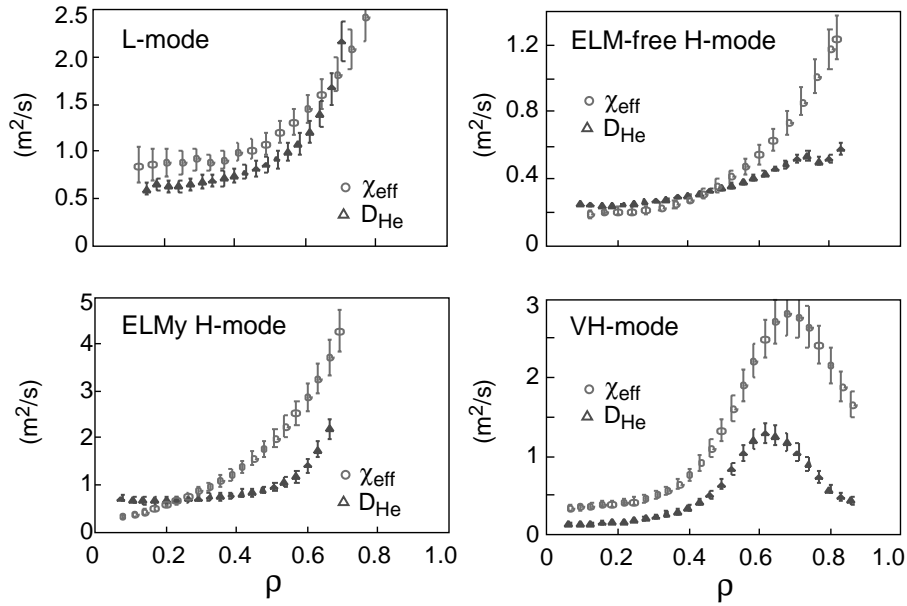
Figure 24. Comparison between D_{He} and χ_{eff} in DIII-D: (a) L-mode, (b) ELM free H-mode, (c) ELMy H-mode, and (d) VH-mode.

a particle pinch and ELM activity strongly affect the coupling between the scrape-off and core plasma. The neoclassical contributions to the particle fluxes and ion thermal conductivity must also be included because these have been shown to be important in the core under improved confinement conditions. Although models for ELMs are just now being developed and not well tested, experimental evidence supports a periodic partial expulsion of the particles from the plasma edge to the scrape-off and divertor.

10. Momentum confinement

Injection of toroidally oriented neutral beams into tokamak plasmas adds toroidal angular momentum to the plasma and results in toroidal plasma rotation. The study of the confinement of toroidal angular momentum and plasma rotation is of interest for several reasons. First, the beam induced toroidal plasma rotation can suppress the growth of the error field instability in a tokamak and improve the stabilizing effect of the resistive wall for low-n kink like modes. Second, the toroidal plasma rotation can contribute to a flow velocity shear suppression of micro-instabilities. Third, angular momentum confinement investigations provide further insight into the general problem of confinement in tokamak plasmas.

The toroidal rotation velocities attained in experiments with tangential high power neutral beam injec-

tion are rather high, i.e. $V_\phi \sim 100\text{--}400\,\text{km·s}^{-1}$, which correspond to a Mach number V_ϕ/c_s up to about 0.3, where c_s is the ion sound velocity. The observed rotation velocities are, however, very small compared to predictions based on the neoclassical transport theory [407, 408].

Measurements of the momentum confinement time τ_ϕ are based on the global angular momentum conservation equation

$$\frac{1}{\tau_\phi} \int dV\, n_i m_i V_\phi = P_b \left(\frac{2m_b}{E_b}\right)^{1/2} \left(\frac{R_{tan}}{R}\right) \quad (36)$$

where R_{tan} is the tangency for the injected neutral beam, P_b is the beam power, m_b and E_b are the mass and energy of beam particles, and $n_i m_i$ is the plasma mass density. Rotation velocities are usually measured by the Doppler shift of emission lines of hydrogen-like impurity ions resulting from charge exchange reactions of fully stripped ions with injected fast hydrogenic particles.

Many tokamaks have reported similar magnitudes for the momentum confinement time τ_ϕ and the energy confinement time τ_E [409–416]. Figure 25 shows a comparison of τ_ϕ with τ_E measured in JET during tangential neutral beam injection [416]. One can see that τ_ϕ and τ_E are approximately equal for steady state L-mode and ELMy H-mode discharges, in agreement with earlier results obtained on ASDEX [413] and Doublet III [411]. Experiments on Doublet III have shown that τ_ϕ and τ_E scale in the same

way with plasma current and neutral beam power. These results, together with the identical shapes of the beam energy and the toroidal angular momentum deposition profiles, suggest that heat and momentum transport at steady state conditions are governed by related mechanisms [22].

There are, however, experimental conditions when τ_ϕ deviates from τ_E. In the transient ELM free phase of hot ion H-mode discharges in JET, the angular momentum confinement time reaches a value of only about 0.6 times the energy confinement time (see Fig. 25). The authors explain this effect by $\boldsymbol{J} \times \boldsymbol{B}$ transfer due to particles injected into trapped orbits and producing the radial current of fast ions between the point of birth and the first orbit average [416]. In high-β_p H-mode discharges in PBX-M, the ratio τ_ϕ/τ_E was observed to increase significantly (from $\sim$1 to $\sim$3), at the same heating power and unchanged τ_E, when the direction of the neutral beam injection was changed from tangential to nearly perpendicular [414]. The authors explain the observed behaviour of τ_ϕ by a strong negative dependence of τ_ϕ on the net torque T_{net}, i.e. $\tau_\phi \propto T_{net}^{-0.8}$. Another reason for the increase in τ_ϕ is a possible change in a beam induced radial electric field E_r, which can affect the toroidal rotation velocity according to Eq. (9).

The MHD activity can strongly affect toroidal rotation. Experiments on DIII-D have shown that some discharges that never exhibit sawtooth oscillations have essentially zero rotation velocity, in spite of the input neutral beam torque [411]. In these discharges, the connection between τ_ϕ and τ_E is clearly broken, since τ_ϕ drops to zero while τ_E decreases by a factor of 2 from its value with sawteeth. Similar phenomena have been observed in ASDEX [417] and JET [418, 419]. They have been explained in terms of the growth of large, stationary magnetic islands (i.e. 'locked' modes) that are capable of transferring angular momentum through an electromagnetic interaction between the MHD mode and either the vacuum vessel or a fixed stray field. A model describing the toroidal force balance for MHD mode locking, consistent with observed toroidal momentum loss in ASDEX, is suggested in [420]. The model includes both the electromagnetic forces due to interaction with a resistive wall and error fields as well as the viscous coupling between the island structure and the bulk plasma. Other similar works appear in [421, 422]. Suppression of the growth of the locked modes by the beam induced plasma rotation is discussed in more detail in Chapter 3, Section 2.5.

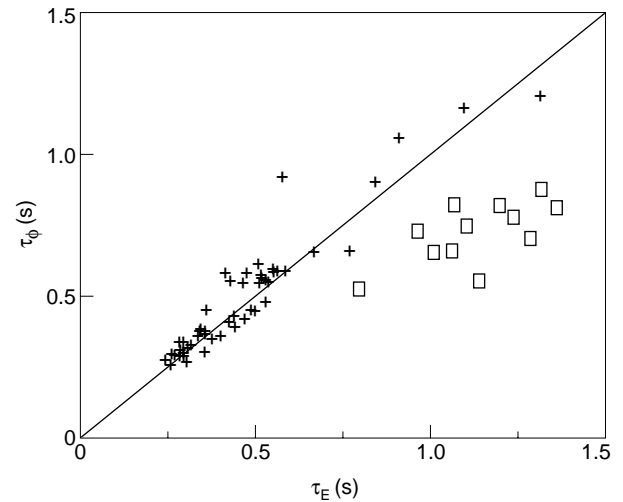In most experiments, E_r is not measured directly

Figure 25. Toroidal angular momentum confinement time of thermal particles during neutral beam injection versus simultaneously measured energy confinement time for steady state L-mode and ELMy H-mode discharges (crosses), and for transient ELM free phase of hot ion H-mode discharges (squares) in JET [415].

because of lack of appropriate techniques. It can be found, however, from Eq. (9), if other terms in the equation are known. Recently, the toroidal and poloidal rotation velocities and the densities and temperatures of the main ions (He^{2+}) and impurity ions (C^{6+} and B^{5+}) have been measured in H-mode helium plasmas in DIII-D [423]. It was shown that the values of E_r deduced from the main ion and impurity ion measurements coincided within the error bars, confirming the validity of Eq. (9). It was shown also that the toroidal rotation velocities of the main ions, $V_{\phi i}$, and impurity ions, $V_{\phi I}$, were quite similar in the plasma core, but significantly different in the edge region. The measured difference ($V_{\phi i} - V_{\phi I}$) was found to agree with the neoclassical prediction, which relates the velocities to radial gradients of densities and temperatures [408].

The radial electric field plays an important role in toroidal rotation characteristics observed in ICRF heated plasmas in the absence of direct input of toroidal momentum. Toroidal rotation velocities of Ar^{16+} impurity ions greater than 120 km·s^{-1} in the co-current direction have been observed in ICRF heated H-mode discharges in Alcator C-Mod [424]. The magnitude of the rotation velocity increases with the stored energy increase. The rotation velocity of the main (deuterium) ions is estimated to be about 1.5 times higher than that of the Ar^{16+} impurity ions and three times higher than the main ion diamag-

netic drift velocity, $\nabla p_i / e n_i B_p$, with the dominant term proportional to the radial electric field (E_r up to $300\,\text{V}\cdot\text{cm}^{-1}$ was deduced from Ar^{16+} ion rotation velocity neglecting its diamagnetic and poloidal rotation terms). The mechanism for the observed rotation is obscure. Similar results have been obtained during ICRF heated H-mode in JET [425]. The toroidal rotation velocities up to $60\,\text{km}\cdot\text{s}^{-1}$ in the co-current direction have been observed in these experiments with a good correlation of the local angular momentum density and the ion pressure. The authors conclude that the ion pressure gradient may be the major driving mechanism for toroidal rotation.

Let us now consider results of measurements of radial profiles of the toroidal momentum diffusivity $\chi_\phi(r)$. Detailed measurements of $\chi_\phi(r)$ and the electron and ion thermal diffusivities $\chi_e(r)$ and $\chi_i(r)$ have been performed on DIII-D in the hot ion L-mode and H-mode [121, 426]. The results presented in Fig. 1 show that the most dramatic improvement at the L-mode to H-mode transition is in $\chi_e(r)$ and $\chi_\phi(r)$, which improve by about a factor of 3 throughout the plasma. Outside of $\rho = 0.3$, χ_e and χ_ϕ are basically equal, within the error bars, in both L-mode and H-mode. χ_i is significantly less than χ_e and χ_ϕ in the centre of both the H-mode and L-mode plasmas, being close to the predictions of the neoclassical theory inside of $\rho = 0.3$ for the H-mode. On the other hand, similar measurements in the hot ion L-mode on TFTR have shown that χ_ϕ is close to χ_i and D_{He} (the helium diffusion coefficient) and is greater than χ_e (Fig. 26) [380]. Similar results have been reported for TFTR L-mode with $T_i \approx T_e$ [427]. The values of $\chi_\phi \approx \chi_i / Z$ have been deduced in JET experiments [428].

The above results are related to effective values of χ_ϕ. Transient toroidal momentum transport has been examined in JT-60U [429] by using a momentum source modulation technique. Assuming that the toroidal momentum flux consists of diffusive and convective terms, it has been found that there is a non-diffusive inward flux of the toroidal momentum, similar to the pinch term in particle transport (Section 9), comparable in absolute value with the diffusive flux.

Experimental values of χ_ϕ discussed above are significantly higher than neoclassical toroidal viscosity, which is $\chi_\phi = \frac{6}{5}\nu_{ii}\rho_i^2$ in the Pfirsch–Schlüter regime [407], or $\chi_\phi = 0.1\nu_{ii}\rho_i^2 q^2$ in the banana regime [430, 431]. Turbulence based theoretical models for χ_ϕ include that due to ITG turbulence:

$\chi_\phi = 1.3(\rho_s^2 c_s / L_s)(1 + \eta_i)/\tau$, where L_s is a magnetic shear length, $\tau = T_e/T_i$ and $\rho_s = c_s/\Omega_i$ [432]. This gyroBohm theory leads to $\chi_i = \chi_\phi$, which is observed in some experiments. Another model based on small scale turbulence leads to very low values of $\tau_\phi = \tau_E m_e / m_i \beta_e$ [433] that contradict experiments.
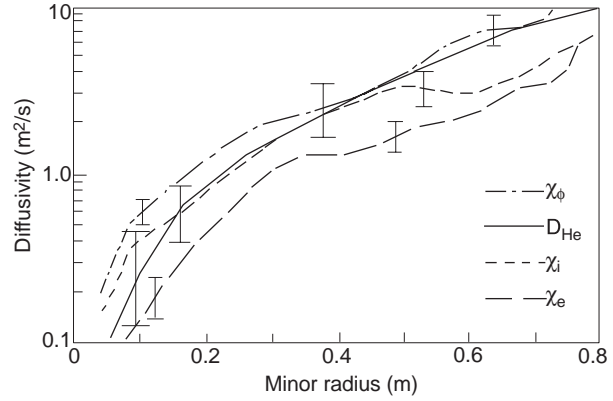

Figure 26. Similarity of the toroidal momentum diffusivity χ_ϕ, helium diffusion coefficient, D_{He}, and ion and electron thermal diffusivities, χ_i and χ_e, in a hot ion L-mode discharge in TFTR [379].

The toroidal plasma rotation frequency in a reactor at a moderate injection power of $\sim 50\,\text{MW}$ and at $E_b \sim 1\,\text{MeV}$ is expected to be significantly lower than in present day experiments, i.e. $f_{\phi,NBI} \sim 1\,\text{kHz}$ for the ITER basic parameters, as follows from Eq. (36) assuming $\tau_\phi = \tau_E$. In practical units this relation can be written as

$$f_{\phi,NBI} \approx (1200\,\text{Hz})\left(\frac{P_b}{50\,\text{MW}}\right)\left(\frac{\tau_\phi}{6\,\text{s}}\right)\left(\frac{2000\,\text{m}^3}{\text{Volume}}\right)$$
$$\times \left(\frac{10^{20}\,\text{m}^{-3}}{n_i}\right)\left(\frac{1\,\text{MeV}}{E_b}\right)^{1/2}\left(\frac{m_b}{m_i}\right)$$
$$\times \left(\frac{m_D}{m_b}\right)^{1/2}\left(\frac{R_{tan}}{6.5\,\text{m}}\right)\left(\frac{8\,\text{m}}{R}\right)^2. \qquad (37)$$

Results of one dimensional modelling of toroidal plasma rotation in ITER for various plasma densities and beam energies at $\chi_\phi = \chi_i$ are given in [434]. The natural diamagnetic frequency [435], which is considered as a measure of the toroidal rotation frequency in the absence of direct toroidal momentum input, is given by

$$f_{\phi,dia} \approx \frac{\rho_{ip}}{2\pi R r}\nu_{ti} \approx (100\,\text{Hz})\left(\frac{\langle T_i\rangle}{10\,\text{keV}}\right)\left(\frac{21\,\text{MA}}{I}\right). \qquad (38)$$

It should be noted, however, that estimates based on Eqns (37) and (38) can be inaccurate in reactor

conditions, where $P_b \ll P_a$ and alpha particles can strongly contribute to the radial electric field.

A more precise prediction of the toroidal plasma rotation needs the creation of a toroidal momentum confinement database and the development of a theoretical model for momentum transport validated against the database.

11. Summary

The basic theory of the transport of heat and particles in a tokamak by both classical and non-classical turbulent processes is becoming mature, although unresolved characteristics of turbulent transport still remain. Qualitative models describing most of the observed phenomena in tokamaks, such as the transport in the plasma core, the L–H transition, sawteeth, and ELMs are available. However, at the present time, we do not have a reliable model describing the transport across the entire plasma profile that could be used in ITER extrapolations. Good progress has been made in testing theoretical transport models in the plasma core region (Section 8) and some of the models give a reasonable fit to the data. This is encouraging and suggests that with further theoretical development, especially for the edge region (e.g. the pedestal temperature), it may be possible to produce a model that gives a good enough fit to the data to be reliably used in ITER predictions.

At the present time, the main approach used in predicting the performance of ITER in its main regime of operation, the steady ELMy H-mode, is the global confinement time scaling approach described in Section 6. In the last two years the global confinement steady state ELMy H-mode database has been considerably expanded with the inclusion of data from five new machines and new data from existing devices. This has reduced the uncertainty in the ITER prediction. Based on the log-linear models applied to various subsets of the data in Section 6.4, the interval estimate is 4.4–6.8 s. This comes close to a classical statistical interval estimate based on the fit for the standard working dataset from Section 6.3, allowing for a multiplication factor (roughly accounting for some of the modelling imperfections). Allowing for non-linear models, and some additional considerations as presented in Section 6.4, the 95% interval estimate is 3.5–8 s. In the latter case, the smaller interval 4.4–6.8 s corresponds, roughly, to a 66% interval estimate.

ITER is projected to ignite throughout the narrow confidence interval although steps might have to be taken such as operation above the Greenwald density, n_{GW}, using pellet injection, or operation at higher plasma current, to preserve ignition at the very lower end of this confinement interval 4.4–4.8 s. With the wider interval, the lowest confinement range 3.5–4.4 s would require driven operation. The performance in driven mode depends on accessibility of densities above n_{GW}, the amount of available heating power and/or higher plasma current. Nevertheless, under nominal conditions ($n/n_{GW} < 1$, $P_{aux} = 100$ MW, $I = 21$ MA) the minimum Q in this range would be above 6.

To reduce the confidence interval, an understanding of the reasons for the systematic differences between the confinement in different devices must be obtained. The identity experiments on different machines used to verify the dimensionless scaling approach will be particularly useful in this respect.

The non-dimensional similarity approach of Section 7 is closely related to the global confinement scaling approach, in that the data themselves are used to determine the performance of ITER. The 95% interval estimate of the dimensionless parameter scaling approach is still larger than that of the global scaling approach. To reduce it, a multi-machine database of these types of pulses will need to be constructed, ensuring similarity of toroidal rotation, and the range of operation of the largest device, JET, be extended to 4 T with 40 MW of heating.

The comforting aspect of these three approaches is that the confidence intervals are overlapping and there is a program to narrow these intervals.

Our knowledge of particle transport is rather weaker than that of energy transport; however, the recommendation of Section 9 that the best procedure is to take $D \sim \chi_i$ means that there will be adequate transport of the helium ash for helium poisoning and the consequent reduction in the fusion power not to be a problem.

The MHD events, such as sawteeth, described in Section 5 will undoubtedly reduce the fusion performance of ITER, but are not thought to have a dominant effect on the confinement projections and may have a beneficial effect on removing the helium ash from the plasma central region. On the other hand, the ELMs that are beneficial in controlling density and impurities also control the height of the edge pedestal, and do, clearly, have an effect on confinement, the type III ELMs leading to lower confinement than those of type I. Although at the present time we do not have good model for this edge region,

both model development and testing are proceeding very rapidly.

Turning to the H-mode threshold, we also find that although there is a reproducible phenomenology of the L → H transition, we do not have a tested quantitative theory. The scaling studies of Section 4 give a rather large range for the required power for an H-mode in ITER. Further effort to understand the reasons for the large scatter in the data and a quantification of the influence of the plasma geometry, edge parameters and neutrals on the H-mode threshold are needed.

Thus, in summary, a qualitative understanding of the energy confinement process taking place in a tokamak is now available, and fairly firm confidence intervals have been given for the ITER predictions; the challenge in the next few years is to narrow these intervals. A further positive feature is that new operational regimes with improved confinement, such as those with reversed shear described in Section 3, continue to be developed, and the use of these regimes will further improve the existing ignition margins of ITER.

Appendix A

A ITER energy confinement projection

A1. Point and interval estimation based on log-linear and log-non-linear scaling expressions

As noted in Section 6.2, the working dataset of DB3, consisting of data from 11 tokamaks, leads to an ELMy log-linear scaling (Eq. (18)) that is similar to ITERH-92P(y), the ELMy log-linear scaling derived from DB2 [305]. Restricting attention to the statistically significant differences only, this new ELMy scaling is proportional to $n^{0.11}M^{-0.2}\kappa^{0.13}$ times ITERH-92P(y), or $n^{0.24}M^{-0.21}B^{-0.24}\varepsilon^{0.34}$ times ITERH-93P. The predictions for the ITER engineering design activity (EDA) standard operating point are approximately the same (assuming 15% confinement degradation due to ELMs in ITER).

It is important to realize that such log-linear scalings only provide a first order approximation to the true regression surface by a linear regression plane on a logarithmic scale. In fact, several types of empirical log-non-linear scalings have been developed, from which one can get some insight into the

accuracy of this approximation. In one approach [180,305,324], interaction models are considered that express, on a logarithmic scale, the confinement time as a sum of not only (first order) linear but also (second order) cross-product terms with respect to the basic plasma parameters, while in another approach [136, 436–438], offset linear type scalings have been derived, which describe the thermal plasma energy as the sum of two power law scalings. Offset linear scalings have been studied for many years [436] and posses a practical physical and empirical motivation. However, actual fitting of such scalings to the data is a fairly high dimensional non-linear problem.

In Section A1, we discuss in somewhat more detail than in Section 6.4, the variation of point predictions from several log-linear scalings (based on various subsets of the working dataset), as well as fits to the data by log-non-linear scalings. In Section A2, we provide statistical background and address some practical aspects of interval estimation for the confinement time in ITER.

The ELMy H-mode confinement scalings based on DB3 in this appendix are based on the working datasets characterized in Section 6.4. An equivalent alternative description is as follows. There are, in fact, several intermediate steps in the transition between DB2 and DB3. In roughly increasing order of heterogeneity with respect to an overall log-linear scaling: DB2.2 (DB2+ASDEX-Upgrade), DB2.5 (DB2.2+JT-60U), DB2.8 (DB2.5+Alcator C-Mod), DB3 (DB2.8+TCV+COMPASS-D). In each step, the tokamak has been added that is most in agreement with the log-linear scaling based on the dataset under consideration. Finally, we consider the restricted subset DB3r(IS) consisting of the large to medium size tokamaks that are similar in shape to ITER (JET, ASDEX-Upgrade, DIII-D, JFT-2M, Alcator C-Mod).

There are several issues, related to the coherence of the dataset, which, for simplicity, are not addressed in the present discussion:

(i) the question of how closed the Alcator C-Mod divertor is with respect to the other machines and the difference between the two divertor types at JET;

(ii) the inclusion of a part of the ELM free JFT-2M dataset that exhibits small ELMs in the D_α signal [439];

(iii) the influence of different heating methods on the observed confinement times;

(iv) the effect of systematic inconsistencies between various (diamagnetic, equilibrium and kinetic) measurements of the plasma stored energy.

With respect to point (iii), it can be stated, qualitatively, that inclusion of the ohmic and ECH discharges from the smaller machines (TCV, COMPASS-D, albeit not for Alcator C-Mod) tends to lead to higher predictions for ITER, whereas inclusion of the JET ICRH discharges tends to produce somewhat lower predictions for ITER than those from the dataset with only NBI heating.

It should also be acknowledged that the present ELMy dataset constitutes a mixture of type I and type III and possibly other types of ELMs. To some extent, the type of ELMs is controlled by the engineering plasma parameters, including the proximity to operational limits. (This is one of the reasons that the difference between ELM free and ELMy scalings is more complicated than a simple multiplication factor, and compatible with the fact that the regression surface of the ELMy confinement time seems to be better described by a simple power law, i.e. to be less curved on a logarithmic scale, than that of the ELM free confinement time [320,438].) Insofar as the type of ELMs is controlled by the engineering plasma parameters, the effect of the change in ELM type on confinement is, in part, reflected by the scalings.

Table 14 describes how well a number of scalings predict the observed confinement times in two of the working datasets and what their prediction is for ITER (at the standard operating point). The first two scalings are log-linear scalings based on DB2. The next scaling, IPB98(y), is based on DB3 and uses $\kappa = b/a$. The following four scalings are based on each of the four working datasets, respectively, and use $\kappa_a = \mathrm{area}/\pi a^2$. The last four scalings in the table are log-non-linear scalings. The most notable difference between the log-linear scalings using $\kappa = b/a$ and the other ones is the aspect ratio dependence.

As is shown in Table 14, the standard log-linear fits to the above restricted versions of the standard dataset give ITER predictions of 4.8 s (DB2.8, i.e. with Alcator C-MOD) and 4.9 s (DB2.5, i.e. without Alcator C-Mod), respectively. According to the subset DB3r(IS) of the 'ITER similar' tokamaks, the log-linear point prediction is 5.6 s. Compared with the 6 s standard estimate of DB2 [180, 305, 320], about $\frac{1}{3}$ of the slightly more than 1 s reduction in confinement time in the first two cases is due to a change in the ITER operating point (i.e. n_e from 13.0 to 9.7×10^{19} m^{-3}, P from 192 to 180 MW) and about

$\frac{2}{3}$ is due to the data from the additional machines. If the ohmic and ECRH H-mode data from COMPASS-D and TCV as well as the JET ICRH discharges are added to DB2.8, then the predictions for the new operating point increase to 5.6 s (IPB98(y,1) with $\kappa_a = 1.53$) and 6 s (IPB98(y) with $\kappa = 1.73$), respectively.

The number of data points contributed by each of the tokamaks varies considerably over the database. This raises a question about how one should weight the data points in the regression. Figure 27 displays the sensitivity of the ITER predictions with respect to weighting the observations from tokamak j by $N_{tok,j}^{-a}$ for $0 < a < 1$, where $N_{tok,j}^{-a}$ stands for the number of observations (i.e. time slices) contributed by tokamak j. (For $a = 0$ all observations and for $a = 1$ all tokamaks are weighted equally.) One can see that the dissimilarity between the ITER predictions tends to become larger when a increases. The correct value of a would be 0 provided all systematic differences between the tokamaks affecting the confinement have been accounted for. Since we know this is only approximately true, there exists no hard statistical rule for the choice of a. Practical experience with analysing the present dataset data may suggest that a moderate value of a ($\frac{1}{3}$ or $\frac{1}{2}$) could lead to somewhat improved estimates with respect to the choice $a = 0$ used in the standard analysis.

As a preamble to a more detailed discussion of several log-non-linear models, a study performed in [437, 438] is illustrated: two models of the offset linear type were fitted to the ELM free DB2 dataset, while using, extensively, the principle of (non-linear) least squares minimization. Since the full offset linear model contains eight geometrical parameters and only six devices were available in DB2, the aspect ratio exponents in both the linear and the offset term in [438] were not fitted to the data, but left as free parameters. A sensitivity study of the change in the other regression exponents with respect to these two unknown aspect ratio exponents over a certain range, led to the compact class of two term power law scalings of the form $W_{th} = W_0 + \tau_{inc}P$ for ELM free H-mode plasma energy content, with the exponents in both terms represented graphically in Fig. 28. These scalings are based on DB2 and, since the ELM free dataset has not been extended very much, essentially also on DB3. For ELMy confinement, an offset non-linear scaling, based on the DB2 dataset extended with confinement data from JT-60U, has been proposed in [439].

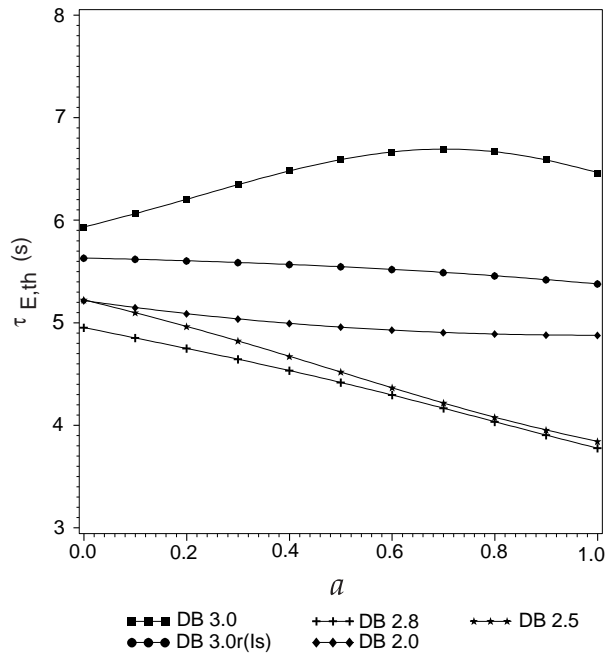We consider in this section three non-linear scal-

Figure 27. Sensitivity of the ITER confinement time prediction with respect to weighting the data from tokamak j proportional to $N_{tok,j}^{-a}$, $0 < a < 1$ (where $N_{tok,j}^{-a}$ stands for the number of time slices included from tokamak j) for log-linear regressions based on each of the four subsets of ITERH.DB3. For $a = 0$ all time slices and for $a = 1$ all tokamaks are weighed equally in the regression fits.

ings (on a logarithmic scale). First, as one of the models that tend to give a rather low confinement prediction for ITER, Dorland and Kotschenreuther have investigated the influence of the interaction between the engineering safety factor $q_{cyl} \propto a^2 B\kappa/IR$ and the ratio of the square root of a dimensionless, normalized pressure gradient, $\alpha \equiv -2\mu_0(q^2R/B^2)dp/dr$, to the normalized Larmor radius, $\rho^* = \rho_i/a$. In engineering variables, this leads to a term

$$\log g_2 \equiv a_{int} \log q_{cyl} \log \frac{\sqrt{na^2 q_{95}^2 h(\varepsilon,\kappa)}}{q_{cyl}} \qquad (39)$$

added to a log-linear model, where h is a shape factor. For the ELM free dataset, the interaction coefficient a_{int} is significant, 0.3 ± 0.04, and this has the interpretation that for large machines, and at higher density, the exponent of q_{cyl} becomes larger. This leads to a lower ITER prediction, about 4 s for 0.85 times ELM free confinement, based on DB2, because the value of q_{cyl} for ITER is below that of the average of the database. (Alternatively, it can be interpreted as a decrease with q_{cyl} of the beneficial effect of the

$(na^2)^{1/2}$ factor on the confinement time.) A breakdown of this interaction term into its constituents has been analysed in [321]. From this, it appears that $\ln(q_{95}/q_{cyl})$, related to the plasma shape, exhibits an empirical influence on confinement, in addition to the usual engineering variables. It should be noted that for the ELM free dataset, additional, statistically significant, interactions are present [313, 440]. This is also apparent from the large difference between the corresponding exponents of the offset and linear term of the offset linear scaling (see Fig. 28). Including these additional interactions increases the prediction for ITER again, to some 5.0 s or above. For the DB2.5 ELMy dataset, the interaction described above is less pronounced, $a_{int} = 0.18 \pm 0.04$, and leads to an ITER prediction of 5.4 s. With Alcator C-Mod included, an additional interaction between current density and power per surface area is present, which suggests a more favourable power dependence at higher current density (which is higher for Alcator C-Mod than for ITER). Including these two interactions leads to an ITER prediction of 5.0 s.
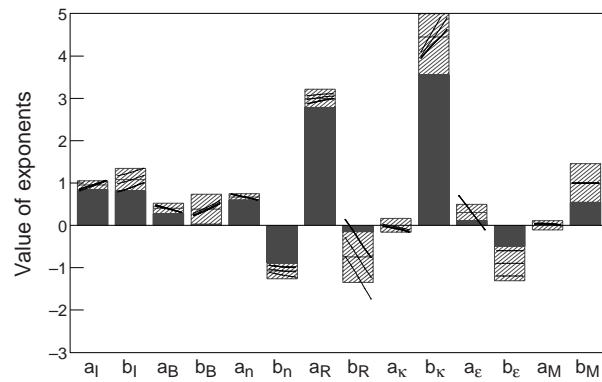

Figure 28. Estimated exponents (± 2 standard deviations shown as shaded parts) in both terms of an ELM free offset linear scaling (OL-95), together with their sensitivity with respect to a variation of the two aspect ratio exponents. The exponents a_ε and b_ε (which correspond to the inverse aspect ratio exponents of the linear and the offset part, respectively) have been varied independently over a range, as simultaneously indicated by their three sensitivity lines. This induces a change in the least squares estimates of the other exponents, as shown by the other sensitivity lines.

We consider next a prediction for ITER based on an ELM free offset linear scaling while making corrections for the presence of ELMs. In the absence of an ELM characterization, we use for ELMy confinement the OL-95 (ELM free) scaling [441] times a multiplier c_{ELMy}, which has been

found from DB2.5 empirically to be proportional to $q_{cyl}^{-0.5} I^{-0.1} (n_{19}/j)^{0.3} \kappa^{-0.2} \varepsilon^{0.4}$, where j denotes the toroidal plasma current density. The first two factors indicate a difference in current and magnetic field dependence, the third factor a tendency of ELMy and ELM free confinement to merge somewhat near the Hugill–Greenwald limit, and the last factor a favourable influence of a small aspect ratio on ELMy versus ELM free confinement. The multiplier c_{ELMy} is an indication to consider any fixed multiplier, e.g. $c_{ELMy} = 0.85$, as merely a zeroth order approximation to the true ELMy scaling. Furthermore, the ELMy data show a different dependence on the net absorbed power (approximated by $P_{L'} = P_L - P_{CX} - P_{OL}$ in [180]) for some of the tokamaks, the effective exponent being 0.3 higher for ASDEX, 0.3 lower for PDX and DIII-D, and 0.15 lower for JET (with mixed divertor data) than that predicted by OL-95 ELM free. The reasons for such differences (divertor type, neutrals, ELM type) are a subject for further investigation. The ELM free OL-95 scaling leads to a prediction of 6.9 s for ITER if one assumes that ELMs lead to 15% confinement degradation in ITER, and 7.3 s if one uses the more complicated multiplier c_{ELMy}, described above.

Finally, we consider the offset non-linear scaling derived in [439], based on the standard ELMy DB2 dataset minus PBX-M plus JT-60U. This scaling accommodates well the Alcator C-Mod data. When deriving this scaling, it has been assumed (in accordance with the discussion above) that PBX-M can be considered as an outlying machine with especially good confinement. The formula is

$$W = 0.082 IBaR\kappa(BR^{1.25})^{-0.1}$$
$$+ 0.043(In_{19}P_L)^{0.6}aR^{1.3}(BR^{1.25})^{-0.15} \quad (40)$$

which gives a relatively low prediction for ITER. The scaling has been derived without correcting the ASDEX and PDX data to account for their 'closed' divertor. This leads to some 10% prediction bias in Table 14. (It is noted that the correction factor TAUC92, motivated in [305], had a somewhat conservative influence on the ITER predictions of the ITERH-92P(y) and ITERPBH-98P(y) scalings.)

The goodness of fit of the various scalings based on the several alternative datasets, and their confinement predictions for ITER, are given in Table 14. The goodness of fit (expressed in 'bias' and 'standard deviation') indicates how well each scaling expression agrees with the observations from two different datasets, DB2.5 and DB3.0. With respect to the pre-

dictions for ITER, in this table no allowance is made for a confinement reduction close to an operational limit (notably density and H-mode threshold).

For reference, Table 13 gives the number of observations from each of the tokamaks in the datasets DB2, DB2.8 and DB3. (DB2.5 is just DB2.8 minus Alcator C-Mod.) In addition, Table 13 shows, approximately, the fraction of 'essentially different' timeslices per tokamak. These fractions are, in Section A2, employed to estimate the proportionality factor c in the expression for the log-linear interval estimate (Eq. (26)).

The three non-linear scalings discussed here, which give quite similar confinement time predictions for the data in the database, complement the existing log-linear models. While being based on different considerations and a varied empirical basis, they give an impression of the way in which the estimate of the energy confinement time in ITER is liable to deviate from the (standard) log-linear ones because of a different functional form of the scaling.

It is noted that two of the three log-non-linear scalings lead to lower confinement time predictions for ITER than the log-linear ones. Because the projection from the present devices corresponds primarily to a change in ρ^*, an important difference between a log-linear and a log-non-linear model is that the first implies a simple power law in ρ^* with a fixed exponent, while the second contains an exponent that depends on the other variables in the model. This could have the character of a critical value of ρ^* at which there is a change in the ρ^* dependence of confinement, as discussed in Section 7.1.

A2. Framework for interval estimation

Based on [320], in this appendix some of the basic concepts of interval estimation are described and applied to the ITERH.DB3 dataset. When making predictions of the energy confinement time that will be achieved by ITER, one has to be aware of the fact that there exist different scalings for the energy confinement time that are all compatible with large and relatively high quality datasets, reasonably in accordance with the available (additional) experimental evidence, and not in direct contradiction with basic principles of plasma theory. This ambiguity is evidently related to the fact that the basic transport mechanism(s) in reactor relevant plasmas is/are not sufficiently well understood, while at the same time a number of competing energy loss processes (their relative strength depending on the plasma parameters)

Table 13. Distribution of the number of data points in the standard working datasets of DB2, DB2.5 and DB3 over various tokamaks

Tokamak	DB2	DB2.5	DB3	N_{eff}/N
ASDEX	298	431	431	0.48
ASDEX-Upgrade	—	102	102	0.45
Alcator C-Mod	—	—	37	0.54
COMPASS-D	—	—	17	0.82
DIII-D	168	270	270	0.71
JET	88	246	306	0.73
JFT-2M	59	59	59	0.32
JT-60U	—	9	9	0.89
PBX-M	59	59	59	0.78
PDX	97	97	97	0.89
TCV	—	—	11	0.64
ALL	769	1273	1398	867/1398

Note: DB2.5 consists of additionally heated discharges by NBI only; DB2.8 equals DB2.5 plus the discharges from Alcator C-Mod. The last column denotes approximately the fraction of 'essentially different' time slices in DB3 (i.e. of which the mutual distance, in all variables, is at least three estimated standard errors of the experimental accuracy).

are playing a role in different parts of the plasma. This makes the global confinement time a multifactorial quantity from which the separate influences are difficult to disentangle. Nevertheless, predictions of energy confinement time in ITER have to be made, in the face of uncertainty, based (as always) on incomplete information, and using the available evidence. During the ITER CDA phase, it was sufficient to concentrate mainly on an accepted scaling of a simple and quite robust type (so-called log-linear scaling or simple power law) and its point prediction for ITER to provide an initial orientation [136]. However, since any point prediction will be different from the value that will actually be achieved, the ITER EDA requires some type of interval estimation. We focus in this section on a 95% interval estimate for ITER. As described in [320], the intuitive meaning of such an interval has been well characterized by T. Takizuka during the ITER CDA phase. However, in order to obtain an operationally useful interval estimate, it is necessary to be precise about the scientific interpretation, and, related to that, about the way such an interval is constructed. We restrict attention to an interval estimate of the average confinement time of a large number (say 1000) of ITER discharges all performed at the same operating point. Two definitions are given, each of which covers a (complementary) part of the complicated real situation and has to be incorporated in some form into an estimate of the prediction margin of ITER.

(i) According to classical frequentist statistical theory, a 95% confidence interval for τ_E is a random interval that covers the 'true' (i.e. average) confinement time with 95% probability under the hypothesis that (a) a specific type of model, e.g. a simple power law scaling, is correct; (b) all essential regression variables are included; and (c) the residual data variation can be, for practical purposes, modelled as independent realizations of haphazard ('random') events. For log-linear models, such a type of interval is routinely calculated by basic statistical software packages (such as SAS, S-PLUS and JMP) [442, 443]. As explained in [321], it is based on error propagation from the centre of gravity of the data to the ITER operating point. A geometrical interpretation yielding formula (26), based on a simple summation of projections in principal axes, was derived in [312], and a linearized projection formula around a standard operating point in [320].

We know, however, that the stated hypothesis is not well satisfied in our situation, and that the classical intervals are too narrow to be physically realistic. To cope with this problem, one can increase the traditional scale factor $c = 2\hat{\sigma}\sqrt{N}$ in the standard error propagation formula to provide some – albeit a general and, hence, imperfect – safety margin. In addition, one can make some assessment about the quality of the approximate character of the fitted

Table 14. Goodness-of-fit of various empirical confinement time scalings for the DB2.5 and DB3.0 standard ELMy datasets and their prediction for ITER

Scaling	Type	Based on	Prediction of DB2.5 (N = 1273)		Prediction of DB3.0 (N = 1398)		ITER (ref.)
			Bias (%)	Std dev. (%)	Bias (%)	Std dev. (%)	τ_E (s)
ITERH-P92y	ll	DB2 (ELMy)	2.9	15.1	2.0	17.5	5.7
ITERH-P93	ll	DB2 (ELM free)[1]	0.7	18.5	0.8	19.3	6.1
IPB98(y)	ll	DB3 (ELMy)[2]	−0.8	15.2	−0.6	15.8	6.0
IPB98(y,1)	ll	DB3 (ELMy)	0.4	14.7	0.6	15.3	5.9
IPB98(y,2)	ll	DB2.8 (ELMy)	0.6	14.5	1.2	15.6	4.9
IPB98(y,3)	ll	DB2.5 (ELMy)	−0.6	14.2	−1.0	16.1	5.0
IPB98(y,4)	ll	DB3r(IS) (ELMy)[3]	5.8	16.7	6.3	17.3	5.1
DK96(y)	ia	DB2.5 (ELMy)	1.1	14.4	0.3	16.5	5.4
DK96(y)	ia	DB2.8 (ELMy)[4]	−0.8	14.6	−0.4	15.3	5.0
OK96(y)	ol	DB2 (ELM free)[5]	—	16.8	2.0	18.7	7.3
TT96(y)	onl	DB2 (ELMy)[6]	10.4	20.1	10.6	22.8	4.4
		[7]	12.8	19.4	12.5	19.3	—

[1] Multiplied by 0.85 to account for ELMs.

[2] Eq. (18); (negligible) bias due to rounding and to satisfying the high beta constraint.

[3] Zero bias and 13.5% standard deviation for the dataset DB3r(IS).

[4] Including a second interaction between current density and input power per surface area, which is not in a favourable direction for ITER.

[5] Adjusted to DB2.8 (ELMy), see text; ITER prediction is 6.9 s for 0.85 times OK-95 ELM free confinement; the values are 9.3 and 8.0 s, respectively, for the ITER IDR parameters (192 MW, 1.3×10^{20} m^{-3}).

[6] Plus JT-60U (ELMy); scaling based on analysis that does not include a correction for ASDEX and PDX with respect to the closeness of their divertor in comparison to the other tokamaks.

[7] The same scaling fitted to DB2.5 and 2.8, respectively, without PBX-M.

Bias means the predicted minus the observed confinement time (on a natural logarithmic scale), averaged over the dataset. Extension (y) indicates that a scaling pertains to ELMy energy confinement. DB3 is the working dataset from Section 6.3; DB2.8 excludes ohmic H-mode and additional heating other than NBI (except for Alcator C-Mod). DB2.5 equals DB2.8 minus Alcator C-Mod.

Abbreviations: ll, log-linear; ia, interaction; ol, offset linear; onl, offset non-linear.

log-linear models. The last element involves (besides graphical residual analysis) issues related to the functional form of the regression surface and to the systematic influence of factors not accounted for in the regression model (usually called 'hidden variables'). The issue of the functional form leads to the following interval definition (even if idealized and departing from classical statistics):

(ii) A 95% interval is formed by 95% (i.e. almost all) 'admissible' non-linear fits (on a logarithmic scale) to the dataset. In this context, the word 'admissible' means that the RMSE decreases significantly with respect to the best fitting log-linear model (simple power law), and that the model selection has been based on 'proper' considerations, i.e. on relatively plausible physical arguments and/or simple model extensions of existing first-order (log-linear)

scalings, rather than on 'artificially construed' mathematical functions, directed towards especially high or especially low ITER confinement.

There are a number of related concepts (see [321]) that try to capture other interesting aspects. However, they are either rather difficult to carry out in practice, or operational prescriptions, rather than intrinsic definitions:

(a) the discharges from a large number of 'identical' machines yield a distribution of confinement times, of which 95% should be situated within the interval;

(b) exchanging the two or three thermal energy measurements available per machine (based on W_{dia}, W_{mhd}, W_{kin}), yields a large number of different predictions from which one can delete

the 5% of extreme ones to obtain an interval estimate;

(c) one can construct jackknife type interval estimates by deleting one machine at a time from the database and looking at the variation in the ITER prediction.

Alternatively, one can perform some cross validation by comparing the predicted confinement times of the tokamak deleted with the values actually observed.

For practical application we return to approach (i). Following the argumentation in [321], we will base the evaluation of the log-linear interval estimate on the multiplication factor

$$c = c_\alpha \hat{\sigma} / \sqrt{N_{eff} H},$$

with

$$c_\alpha = u_\alpha \sqrt[4]{N_{eff} H / 64},$$

instead of on the classical value $c = 2\hat{\sigma}/\sqrt{N}$. Here, N_{eff} denotes the 'effective number' of data points, which means that multiple observations in all variables (within measurement error) are excluded. (As usual, u_α is defined by the property that the probability of a standard normal random variable to exceed u_α equals α). The quantity

$$N_{eff} H = - \sum_{j=1}^{N_{tok}} N_{eff,j} \, \mathrm{lb}(N_{eff,j}/N_{eff})$$

where N_{tok} is the number of tokamaks, lb denotes the binary logarithm, and H is the Shannon uncertainty measure [444,445] reflecting the degree of non-uniformity of the distribution of the data points over the tokamaks. For two tokamaks, each with 32 effective data points, c is equal to the familiar $2\hat{\sigma}/\sqrt{N}$ corresponding to a classical (two sided) 95% interval. For other values of N_{tok} and $N_{eff,1}, \ldots, N_{eff,N_{tok}}$, a normalization to this situation has been made. This approach provides at least some safeguard against remaining moderate systematic influences that are almost always present, but are not reduced as the square root of the sample size increases. (The absolute value of this calibration depends somewhat on a practical judgment of the specific situation.) The estimated values of $N_{eff,1}, \ldots, N_{eff,N_{tok}}$ can be found in Table 13. In our case, for the DB3 ELMy dataset, $N_{eff} = 867$, $H/H_{max} = 0.785$, $H_{max} = \mathrm{lb}(11) = 3.46$, which makes $c_\alpha = 4.8$ and $c = 1.5\%$ instead of the classical value $c = 0.8\%$. The scaling of the ELM free data, multiplied by a factor 0.85 to account for a roughly estimated confinement loss due to ELMs

in ITER, supports, in general, the prediction based on the ELMy dataset. Hence, this prediction is based on more information than the ELMy dataset alone. In fact, for the total (ELMy and ELM free) DB3 dataset, we have $N = 2529$, $N_{eff} = 1600$, $H/H_{max} = 0.795$, $H_{max} = 3.46$, $c_\alpha = 5.6$ and $c = 1.27\%$. Along this line of thought, the additional information from the ELM free data reduces the width of the log-linear interval from the ELMy dataset by some 15% to about 1.6 times the width according to the classical formulation.

From the second approach, a 95% confidence interval for ITER confinement should include the interval 4–7.5 s according to the three types of non-linear scalings analysed in Section 2.6.4. Although, obviously, not all possible non-linear models have been investigated, the non-linear scalings discussed stem from a range of analyses by different investigators and by using different approaches. By applying automatic optimization procedures towards high and low predictions for ITER, which disregards the 'admissibility' criterion above, it is possible to arrive at more extreme predictions. We will not pursue this approach any further here, but set the interval to 3.5–8 s.

Originated by Tukey [446], it has become a popular method to apply jackknife type estimators for the variance of the estimator of an unknown parameter of interest, partly in view of the ease with which they can be (electronically) calculated. Nevertheless, the statistical basis of jackknife type arguments ('leaving out one tokamak in turn') is quite intricate. In [321] it was found (by error propagation analysis) that these lead to some type of cross validated interval estimates

$$c = c_\alpha \hat{\sigma}_{cr,eff} / \sqrt{N_{eff} H}$$

that are roughly a factor 2 larger than those using

$$c = c_\alpha \hat{\sigma} / \sqrt{N_{eff} H}$$

if the assumption of a log-linear model is not abandoned. In [322] it was argued that by applying the simple variance formula (coined 'shotgun' estimator in Efron's fundamental paper [447]) applied to the DB3 working dataset, the width of the interval estimate increases by an additional factor of 2, which amounts to about six times the classical width. As explained in more detail in [321], these two approaches relax, in different degrees, the full classical log-linear model assumptions, albeit without accurately specifying the class of alternative regression models assumed. The accuracy of the latter

approach depends, notably, on the number of tokamaks (rather than on the effective number of timeslices) being sufficiently large to yield reasonable asymptotic approximations.

A further complication arises from the large variation in scaling exponents from different tokamak operating periods, even with respect to the present non-linear scalings. When modelled by a, somewhat artificial, log-linear random coefficient model [321], these lead to a different type of error propagation than a constant times the classical error. One of the basic problems seems to be that the shape of the true regression surface is not yet sufficiently well known, and the statistical methodology for fitting 'catastrophic type' response functions [320] is still in an initial stage of its development. As discussed in Section 6.4, there are various additional issues associated with practical physical modelling of plasma transport and with the question of hidden variables that may have additional influence on confinement. Further work in this area is being pursued.

As described in [320], on the basis of considerations of the type outlined here, while utilizing the information at the Naka-95 expert group meeting, a 95% (log-non-linear) interval estimate for ITER, based on DB2, was set at 3.5–9 s, and a 95% (log-linear) interval estimate at 4.2–7.8 s, centred around the point estimate of 6.0 s. (The latter interval corresponds, numerically, to roughly a 66% log-non-linear interval.) The present analysis, based on the various subsets of the extended database DB3, suggests a 95% log-non-linear interval estimate of 3.5–8 s, and a $\frac{2}{3}$ log-non-linear (95% log-linear) interval of 4.4–6.8 s, centred around the point estimate 5.5 s. This result is graphically displayed in Fig. 13. The shift with respect to the previous interval is partly due to the new data and additional analysis and partly to the change (from the IDR to the DDR values) of the reference operating point. The dependence of the log-linear interval width on the actual operating point (in the neighbourhood of a reference operating point) has been expressed analytically by a simple linearized formula in [321]. For constructing the corresponding log-non-linear interval estimate, a more computer (and human intervention) intensive approach is still required, except for the simple situation in which the actual operating point does not deviate very much from the reference operating point.

References

[1] Artsimovich, L.A., et al., in Nuclear Fusion Special Supplement 1969 (Conf. Proc., English translation of the Russian reports, Novosibirsk, 1968) IAEA, Vienna (1969) 17.

[2] Galeev, A.A., Sagdeev, R.Z., Sov. Phys. JETP **26** (1968) 233.

[3] Galeev, A.A., Sagdeev, R.Z., Furth, H.P., Rosenbluth, M.N., Phys. Rev. Lett. **22** (1969) 511.

[4] Hinton, F.L., Hazeltine, R.D., Rev. Mod. Phys. **48** (1976) 239.

[5] Hirshman, S.P., Sigmar, D.J., Nucl. Fusion **21** (1981) 1079.

[6] Levinton, F.M., et al., Phys. Rev. Lett. **75** (1995) 4417.

[7] Lazarus, E.A., et al., Phys. Rev. Lett. **77** (1996) 2714.

[8] Koide, Y., Phys. Plasmas **4** (1996) 1623.

[9] Braginskii, S.I., Transport Processes in a Plasma, in Reviews of Plasma Physics, Vol. 1 (ed. M.A. Leontovich) Consultants Bureau, New York (1965) 205.

[10] Bickerton, R.J., Connor, J.W., Taylor, J.B., Nat. Phys. Sci. **239** (1971) 110.

[11] Zarnstorff, M.C., Prager, S.C., Phys. Rev. Lett. **53** (1984) 454.

[12] Kikuchi, M., Azumi, M., Plasma Phys. Control. Fusion **37** (1995) 1215.

[13] Itoh, K., Itoh, S.I., Plasma Phys. Control. Fusion **38** (1996) 1.

[14] Biglari, H., Diamond, P.H., Terry, P.W., Phys. Fluids B **2** (1990) 1.

[15] Kotschenreuther, M., Dorland, W., Beer, M.A., Hammett, G.W., Phys. Plasmas **2** (1995) 2381.

[16] Dnestrovskii, Y.N., Kostomarov, D.P., Numerical Simulation of Plasmas, Springer series in Computational Physics, Springer-Verlag, New York (1985) 304.

[17] Liewer, P.C., Nucl. Fusion **25** (1985) 543.

[18] Robinson, D.C., Confinement and Electrostatic and Electromagnetic Fluctuations, in Turbulence and Anomalous Transport in Magnetized Plasmas (ed. D. Gresillon, M. Dubois) Ecole Polytechnique, Palaiseau (1986) 21.

[19] Surko, C.M., Density Fluctuations in a Tokamak – After a Decade of Research what We Can Say?, in Turbulence and Anomalous Transport in Magnetized Plasmas, (ed. D. Gresillon, M. Dubois) Ecole Polytechnique, Palaiseau (1986) 93.

[20] Callen, J.D., Phys. Fluids B **2** (1990) 2869.

[21] Callen, J.D., Phys. Fluids B **4** (1992) 2142.

[22] Wagner, F., Stroth, U., Plasma Phys. Control. Nucl. Fusion **35** (1993) 1321.

[23] Connor, J.W., Plasma Phys. Control. Fusion **37** (1995) A119.

[24] Wootton, A.J., et al., Phys. Fluids B **2** (1990) 2879.

[25] Frisch, U., Turbulence, the Legacy of A.N. Kolmogorov, Cambridge University Press, Cambridge (1995) 296.

[26] Kadomtsev, B.B., Pogutse, O.P., Turbulence in Toroidal Systems, in Reviews of Plasma Physics, Vol. 5 (ed. M.A. Leontovich) Consultants Bureau, New York (1970) 249.

[27] Tang, W., Nucl. Fusion **18** (1978) 1089.

[28] Horton, W., Phys. Rep. **192** (1990) 1.

[29] Connor, J.W., Wilson, H.R., Plasma Phys. Control. Fusion **36** (1994) 719.

[30] Itoh, K., Yagi, M., Itoh, S.-I., Fuluyama, A., Azumi, M., Plasma Phys. Control. Fusion **35** (1993) 543.

[31] Connor, J.W., Chen, L., Phys. Fluids **28** (1985) 2201.

[32] Callen, J.D., Shaing, K.C., Phys. Fluids **28** (1985) 1845.

[33] Carrera, R., Hazeltine, R.D., Kotschenreuther, M., Phys. Fluids **29** (1986) 899.

[34] Ware, A.A., et al., Phys. Fluids B **4** (1992) 877.

[35] Rogister, A.L.M., Li, D., Nucl. Fusion **33** (1993) 1799.

[36] Rogister, A.L.M., Li, D., Nucl. Fusion **33** (1993) 1817.

[37] Ross, D.W., Phys. Plasmas **1** (1994) 2630.

[38] Dupree, T.H., Phys. Fluids **9** (1966) 1773.

[39] Dupree, T.H., Tetreault, D.J., Phys. Fluids **21** (1978) 425.

[40] Kadomtsev, B.B., Plasma Turbulence, Academic Press, New York (1965).

[41] Hasegawa, A., Mima, K., Phys. Rev. Lett. **39** (1977) 205.

[42] Terry, P., Horton, W., Phys. Fluids **25** (1982) 491–501.

[43] Wakatani, M., Hasegawa, A., Phys. Fluids **27** (1984) 611.

[44] Carreras, B.A., Garcia, L., Diamond, P.H., Phys. Fluids **30** (1987) 1388.

[45] Lee, G.S., Diamond, P.H., Phys. Fluids **29** (1986) 3291.

[46] Connor, J.W., Taylor, J.B., in Plasma Physics and Controlled Nuclear Fusion Research 1984 (Proc. 9th Int. Conf. London, 1984), Vol. 2, IAEA, Vienna (1985) 13.

[47] Connor, J.W., Plasma Phys. Control. Fusion **30** (1988) 619.

[48] Barenblatt, G.I., Scaling, Selfsimilarity, and Intermediate Asymptotics, in Cambridge Texts in Applied Mathematics (ed. D.G. Crighton) Cambridge University Press, Cambridge (1996) 386.

[49] Goldenfeld, N., Martin, O., Oono, Y., J. Scient. Comput. **4** (1989) 355.

[50] Mannheimer, W.M., Chu, K.R., Ott, E., Boris, J.P., Phys. Rev. Lett. **37** (1976) 286.

[51] Connor, J.W., Taylor, J.B., Turner, M.F., Nucl. Fusion **24** (1984) 642.

[52] Furth, H.P., Plasma Phys. Control. Fusion **28** (1986) 1305.

[53] Rogister, A., Hasselberg, G., Phys. Fluids **26** (1983) 1467.

[54] Rogister, A., Hasselberg, G., Waelboeck, F.G., Weiland, J., Nucl. Fusion **28** (1988) 1053.

[55] Gang, F.Y., Diamond, P.H., Rosenbluth, M.N., Phys. Fluids B **3** (1991) 68.

[56] Hammett, G.W., Perkins, F.W., Phys. Rev. Lett. **64** (1990) 3019.

[57] Jarmen, A., Andersson, P., Weiland, J., Nucl. Fusion **27** (1987) 941.

[58] Dawson, J.M., Phys. Plasmas **2** (1995) 2189.

[59] Sydora, R.D., Hahm, T.S., Lee, W.W., Dawson, J., Phys. Rev. Lett. **64** (1990) 2015.

[60] Cohen, B.I., et al., Comput. Phys. Commun. **87** (1995) 1.

[61] Fonck, R.J., et al., Phys. Rev. Lett. **70** (1993) 3736.

[62] Rhodes, T.L., et al., Rev. Sci. Instrum. **63** (1992) 4599.

[63] Nazikian, R., Mazzucato, E., Rev. Sci. Instrum. **66** (1995) 392.

[64] Laviron, C., Donné, A.J.H., Manso, M.E., Sanchez, J., Plasma Phys. Control. Fusion **38** (1996) 905.

[65] Cima, G., Rev. Sci. Instrum. **63** (1992) 4630.

[66] Sattler, S., Hartfuss, H.J., Plasma Phys. Control. Fusion **35** (1993) 1285.

[67] Hickock, R.L., Jobes, F.C., Heavy Ion Beam Probe System for Plasma Diagnostics, Rep. AFOSR-70-2354 TR, FR-5, Mobil Research and Development Corporation (1970).

[68] Fonck, R.J., et al., in Plasma Physics and Controlled Nuclear Fusion Research 1994 (Proc. 15th Int. Conf. Seville, 1994), Vol. 2, IAEA, Vienna (1995) 53.

[69] Zou, X.L., Paume, M., Chareau, J.M., Laurent, L., Gresillon, D., in Controlled Fusion and Plasma Physics (Proc. 20th Eur. Conf. Lisbon, 1993), Vol. 17C, Part III, European Physical Society, Geneva (1993) 1091.

[70] Connor, J.W., Plasma Phys. Control. Fusion **35** (1993) B293.

[71] MOYER, R.A., et al., Phys. Plasmas **2** (1995) 2397.

[72] Kadomtsev, B.B., Sov. J. Plasma Phys. **1** (1975) 295.

[73] Connor, J.W., Taylor, J.B., Nucl. Fusion **17** (1977) 1047.

[74] Perkins, F.W., et al., Phys. Fluids B **5** (1993) 477.

[75] Kotschenreuther, M., et al., in Fusion Energy 1996 (Proc 16th Int. Conf. Montréal, 1996), Vol. 2, IAEA, Vienna (1997) 371.

[76] Petty, C.C., et al., Phys. Plasmas **2** (1995) 2342.

[77] JET Team (presented by M. Keilhacker), in

Plasma Physics and Controlled Nuclear Fusion Research 1992 (Proc. 14th Int. Conf. Würzburg, 1992), Vol. 1, IAEA, Vienna (1993) 15.

[78] Shirai, H., et al., in Plasma Physics and Controlled Nuclear Fusion Research 1994 (Proc. 15th Int. Conf. Seville, 1994), Vol. 1, IAEA, Vienna (1995) 355.

[79] Petty, C.C., Luce, T.C., Balet, B., Christiansen, J.P., Cordey, J.G., in Controlled Fusion and Plasma Physics (Proc. 23rd Eur. Conf. Kiev, 1996), Vol. 20C, Part I, European Physical Society, Geneva (1996) 211.

[80] Connor, J.W., Taylor, J.B., Wilson, H.R., Phys. Rev. Lett. **70** (1993) 1803.

[81] Romanelli, F., Zonca, F., Phys. Fluids B **5** (1993) 4081.

[82] Kim, J.Y., Wakatani, M., Phys. Rev. Lett. **73** (1994) 2200.

[83] Artun, M., Tang, W.M., Rewoldt, G., Phys. Plasmas **2** (1995) 3384.

[84] Garbet, X., Waltz, R.E., Phys. Plasmas **3** (1996) 1898.

[85] Bak, P., Tang, C., Weisenfeld, K., Phys. Rev. Lett. **59** (1987) 381.

[86] Newman, D.E., Carreras, B.A., Diamond, P.H., Hahm, T.S., Phys. Plasmas **3** (1996) 1858.

[87] Hegna, C.C., et al., Plasma Phys. Control. Fusion **35** (1993) 987.

[88] Newman, D.E., Carreras, B.A., Diamond, P.H., Phys. Lett. A **218** (1996) 58.

[89] Bessenrodt-Weberpals, M., Wagner, F., ASDEX Team, Nucl. Fusion **33** (1993) 1205.

[90] Cardozo, N.J.L., Plasma Phys. Control. Fusion **37** (1995) 799.

[91] Ryter, F, et al., in Fusion Energy 1996 (Proc. 16th Int. Conf. Montréal, 1996), Vol. 1, IAEA, Vienna (1997) 625.

[92] Milora, S.L., Houlberg, W.A., Lengyel, L.L., Mertens, V., Nucl. Fusion **35** (1995) 657.

[93] Neudatchin, S.V., Cordey, J.G., Muir, D.G., in Controlled Fusion and Plasma Physics (Proc. 20th Eur. Conf. Lisbon, 1993), Vol. 17C, Part I, European Physical Society, Geneva (1993) 83.

[94] Cordey, J.G., et al., Nucl. Fusion **35** (1995) 505.

[95] Gentle, K.W., et al., Phys. Plasmas **2** (1995) 2292.

[96] Kissick, M.W., et al., Nucl. Fusion **34** (1994) 349.

[97] Ogawa, Y., et al., Nucl. Fusion **29** (1989) 1873.

[98] Sabot, R., Dubois, M.A., in Plasma Physics and Control. Fusion (Proc. 22nd Eur. Conf. Bournemouth, 1995), Vol. 19C, Part IV, European Physical Society, Geneva (1995) 249.

[99] Kadomtsev, B.B., Sov. J. Plasma Phys. **13** (1987) 443.

[100] Dnestrovskij, Yu.N., Berezovskij, E.L., Lysenko, S.E., Pivinskij, A.A., Tarasyan, K.N., Nucl. Fusion **31** (1991) 1877.

[101] Goldston, R.J., Plasma Phys. Control. Fusion **26** (1984) 87.

[102] Shimomura, Y., Suzuki, N., Empirical Scalings of Energy Confinement Time of L-mode and Optimized Mode and Some Consideration of Reactor Core Plasma in Tokamak, Rep. JAERI-M 87-080, Japan Atomic Energy Research Institute (1987).

[103] Tibone, F., et al., Nucl. Fusion **33** (1993) 1319.

[104] Barnes, C.W., et al., Phys. Plasmas **3** (1996) 4521.

[105] Gaudreau, M., et al., Phys. Rev. Lett. **39** (1977) 1266.

[106] Murakami, M., et al., in Plasma Physics and Controlled Nuclear Fusion Research 1978 (Proc. 7th Int. Conf. Innsbruck, 1978), Vol. 1, IAEA, Vienna (1979) 269.

[107] Merezhkin, V., Mukhovatov, V., Polevoi, A., Sov. J. Plasma Phys. **14** (1988) 69.

[108] Greenwald, M., et al., Phys. Rev. Lett. **53** (1984) 352.

[109] Soldner, F.X., et al., Phys. Rev. Lett. **61** (1988) 1105.

[110] Alikaev, V., et al., Sov. J. Plasma Phys. **13** (1987) 1.

[111] Hoang, G., et al., Nucl. Fusion **34** (1994) 75.

[112] Kaye, S.M., et al., Nucl. Fusion **37** (1997) 1303.

[113] Kaye, S.M., Phys. Fluids **28** (1985) 2327.

[114] Kaye, S.M., et al., Phys. Fluids B **2** (1990) 2926.

[115] Scott, S.D., et al., Phys. Plasmas **2** (1995) 2299.

[116] Scott, S.D., et al., in Fusion Energy 1996 (Proc. 16th Int. Conf. Montréal, 1996), Vol. 1, IAEA, Vienna (1997) 573.

[117] Zarnstorff, M.C., et al., in Plasma Physics and Controlled Nuclear Fusion Research 1990 (Proc. 13th Int. Conf. Washington, 1990), Vol. I, IAEA, Vienna (1991) 109.

[118] Challis, C.D., et al., Nucl. Fusion **32** (1992) 2217.

[119] Paul, S.F., et al., Phys. Fluids B **4** (1992) 2922.

[120] Wagner, F., et al., Phys. Rev. Lett. **49** (1982) 1408.

[121] Burrell, K., et al., in Plasma Physics and Controlled Nuclear Fusion Research 1990 (Proc. 13th Int. Conf. Washington, 1990), Vol. 1, IAEA, Vienna (1991) 123.

[122] Strachan, J., et al., Phys. Rev. Lett. **58** (1987) 1004.

[123] Ongena, J., et al., Nucl. Fusion **33** (1993) 283.

[124] Ongena, J., et al., in Plasma Physics and Controlled Nuclear Fusion Research 1992 (Proc. 14th Int. Conf. Würzburg, 1992), Vol. 1, IAEA, Vienna (1993) 725.

[125] Lazarus, E., et al., Nucl. Fusion **25** (1985) 135.

[126] Gehre, O., et al., Phys. Rev. Lett. **60** (1988) 1502.

[127] JET Team (presented by D. Stork), in Plasma Physics and Controlled Nuclear Fusion Research 1994 (Proc. 15th Int. Conf. Seviile, 1994), Vol. 1, IAEA, Vienna (1995) 51.

[128] Wade, M., et al., Phys. Rev. Lett. **74** (1995) 2702.

[129] Naito, O., The JT-60 Team, Plasma Phys. Control. Fusion **35** (1993) B215.

[130] Strait, E., et al., Phys. Rev. Lett. **75** (1995) 4421.

[131] JET Team (presented by C. Gormezano), in Fusion Energy 1996 (Proc. 16th Int. Conf. Montréal, 1996), Vol. 1, IAEA, Vienna (1997) 487.

[132] Tubbing, B.J.D., et al., Nucl. Fusion **31** (1991) 839.

[133] Fujita, T., et al., in Fusion Energy 1996 (Proc. 16th Int. Conf. Montréal, 1996), Vol. 1, IAEA, Vienna (1997) 227.

[134] Strait, E.J., et al., in Controlled Fusion and Plasma Physics (Proc. 23rd Eur. Conf. Kiev, 1996), Vol. 20C, Part III, European Physical Society, Geneva (1996) 1493.

[135] Shirai, H., The JT-60 Team, Phys. Plasmas **5** (1998) 1712.

[136] Yushmanov, P.N., et al., Nucl. Fusion **30** (1990) 1999.

[137] Synakowski, E., et al., Phys. Rev. Lett. **78** (1997) 2972.

[138] Levinton, F., et al., in Fusion Energy 1996 (Proc. 16th Int. Conf. Montréal, 1996), Vol. 1, IAEA, Vienna (1997) 211.

[139] Mazzucato, E., et al., Phys. Rev. Lett. **77** (1996) 3145.

[140] Bell, M., et al., Phys. Plasmas **5** (1997) 1714.

[141] Rice, B., et al., Phys. Plasmas **3** (1996) 1983.

[142] Lao, L., et al., Phys. Plasmas **3** (1996) 1951.

[143] Schissel, D., et al., in Fusion Energy 1996 (Proc. 16th Int. Conf. Montréal, 1996), Vol. 1, IAEA, Vienna (1997) 463.

[144] Turnbull, A., et al., in Fusion Energy 1996 (Proc. 16th Int. Conf. Montréal, 1996), Vol. 2, IAEA, Vienna (1997) 509.

[145] Fujita, T., et al., Phys. Rev. Lett. **78** (1997) 2377.

[146] Ushigusa, K., et al., in Radio Frequency Power in Plasmas (Proc. 12th Topical Conf. Savannah, 1997) AIP Conference Proceedings 403, American Institute of Physics, New York (1997) 111.

[147] Sips, A.C.C., et al., in Controlled Fusion and Plasma Physics (Proc. 24th Eur. Conf. Berchtesgaden, 1997), Vol. 21A, Part I, European Physical Society, Geneva (1997) 97.

[148] JET Team (presented by F.X. Söldner), Plasma Phys. Control. Fusion **39** (1997) B353.

[149] Hugon, M., et al., Nucl. Fusion **32** (1992) 33.

[150] Kishimoto, Y., et al., in Fusion Energy 1996 (Proc. 16th Int. Conf. Montréal, 1996), Vol. 2, IAEA, Vienna (1997) 581.

[151] Fukuyama, A., Yagi, M., Itoh, S.-I., Itoh, K., in Fusion Energy 1996 (Proc. 16th Int. Conf. Montréal, 1996), Vol. 2, IAEA, Vienna (1997) 593.

[152] Burrell, K., Phys. Plasmas **4** (1997) 1499.

[153] Beer, M., et al., Phys. Plasmas **4** (1997) 1792.

[154] Synakowski, E., et al., Phys. Plasmas **4** (1997) 1736.

[155] Hahm, T.-S., Burrell, K., Phys. Plasmas **2** (1995) 1648.

[156] Bell, R.E., Levinton, F.M., Batha, S.H., Synakowski, E.J., Zarnstorff, M.C., Plasma Phys. Control. Fusion **40** (1998) 609.

[157] Jackson, G., et al., Phys. Rev. Lett. **67** (1991) 3098.

[158] La Haye, R., et al., Nucl. Fusion **35** (1995) 988.

[159] Equipe TORE-SUPRA, in Fusion Energy 1996 (Proc. 16th Int. Conf. Montréal, 1996), Vol. 1, IAEA, Vienna (1997) 141.

[160] Equipe TORE-SUPRA, Plasma Phys. Control. Fusion **38** (1996) A251.

[161] Sabbagh, S., et al., in Fusion Energy 1996 (Proc. 16th Int. Conf. Montréal, 1996), Vol. 1, IAEA, Vienna (1997) 921.

[162] Ishida, S., et al., in Plasma Physics and Controlled Nuclear Fusion Research 1990 (Proc. 13th Int. Conf. Washington, 1990), Vol. 1, IAEA, Vienna (1991) 195.

[163] Ishida, S., et al., in Plasma Physics and Controlled Nuclear Fusion Research 1992 (Proc. 14th Int. Conf. Würzburg, 1992), Vol. 1, IAEA, Vienna (1993) 219.

[164] Koide, Y., et al., in Plasma Physics and Controlled Nuclear Fusion Research 1994 (Proc. 15th Int. Conf. Seville, 1994), Vol. 1, IAEA, Vienna (1995) 199.

[165] Mori, M., et al., Nucl. Fusion **34** (1994) 1045.

[166] Kamada, Y. et al., in Fusion Energy 1996 (Proc. 16th Int. Conf. Montréal, 1996), Vol. 1, IAEA, Vienna (1997) 247.

[167] Miura, Y., et al., in Plasma Physics and Controlled Nuclear Fusion Research 1990 (Proc. 13th Int. Conf. Washington, 1990), Vol. 1, IAEA, Vienna (1991) 325.

[168] JET Team (presented by G.L. Schmidt), in Plasma Physics and Controlled Nuclear Fusion Research 1988 (Proc. 12th Int. Conf. Nice, 1988), Vol. 1, IAEA, Vienna (1989) 215.

[169] Kaufmann, M., et al., in Plasma Physics and Controlled Nuclear Fusion Research 1988 (Proc. 12th Int. Conf. Nice, 1988), Vol. 1, IAEA, Vienna (1989) 229.

[170] Terry, J., et al., in Plasma Physics and Controlled Nuclear Fusion Research 1990 (Proc. 13th Int. Conf. Washington DC, 1990), Vol. 1, IAEA, Vienna (1991) 393.

[171] Ryter, F., et al., Plasma Phys. Control. Fusion **36** (1994) A99.

[172] Ongena, J., et al., in Controlled Fusion and Plasma Physics (Proc. 20th Eur. Conf. Lisbon, 1993), Vol. 17C, Part I, European Physical Society (1993) 127.

[173] Messiaen, A., et al., Phys. Rev. Lett. **77** (1996) 2487.

[174] Messiaen, A., et al., Phys. Plasmas **4** (1997) 1690.

[175] Neuhauser, J., et al., Plasma Phys. Control. Fusion **37** (1995) A37.

[176] Staebler, G., et al., in Controlled Fusion and Plasma Physics (Proc. 24th Eur. Conf. Berchtesgaden, 1997), Vol. 21A, Part III, European Physical Society, Geneva (1997) 1093.

[177] Jackson, G.L, et al., in Controlled Fusion and Plasma Physics (Proc. 25th Eur. Conf., Prague, 1998), Vol. 22C, European Physical Society, CD ROM Edition, `http://www.ipp.cas.cz/conference/98icpp` (1998) 810.

[178] Jackson, G.L., et al., J. Nucl. Mat. **266**–**269** (1999) 380.

[179] Wade, M.R., et al., J. Nucl. Mat. **266**–**269** (1999) 44.

[180] H-Mode Database Working Group (presented by D.P. Schissel), in Controlled Fusion and Plasma Physics (Proc. 20th Eur. Conf. Lisbon, 1993), Vol. 17C, Part 1, European Physical Society, Geneva (1993) 103.

[181] Hobirk, J., in Controlled Fusion and Plasma Physics (Proc. 24th Eur. Conf. Berchtesgaden, 1997), Vol. 21A, Part IV, European Physical Society, Geneva (1997) 1861.

[182] Ongena, J., et al., in Controlled Fusion and Plasma Physics (Proc. 24th Eur. Conf. Berchtesgaden, 1997), Vol. 21A, Part IV, European Physical Society, Geneva (1997) 1693.

[183] Ongena, J., et al., in Proc. of the 7th Eur. Fusion Theory Conf. (Jülich, 1997) Institut für Plasmaphysik (ed. A. Rogister) Jülich (1998) 91.

[184] Ongena, J., et al., Plasma Phys. Control. Fusion (to be published).

[185] Schissel, D.P., et al., Nucl. Fusion **31** (1991) 73.

[186] Lazarus, E.A., et al., Phys. Fluids B **4** (1992) 3644.

[187] Wade, M.R., et al., Phys. Plasmas **2** (1995) 2357.

[188] Matsumoto, H., et al., in Controlled Fusion and Plasma Physics (Proc. 14th Eur. Conf. Madrid, 1987), Vol. 11D, Part I, European Physical Society, Geneva (1987) 5.

[189] Toi, K, et al., Phys. Rev. Lett. **64** (1990) 1895.

[190] Burrell, K.H., et al., Plasma Phys. Control. Fusion **31** (1989) 1649.

[191] Bush, C.E., et al., Phys. Rev. Lett. **65** (1990) 424.

[192] Bretz, N., Nazikian, R., Bush, C.E., Riedel, K., Sidorenko, A., Plasma Phys. Control. Fusion **36** (1994) A141.

[193] Erckmann, V., et al., in Plasma Physics and Controlled Nuclear Fusion Research 1992 (Proc. 14th Int. Conf. Würzburg, 1992), Vol. 2, IAEA, Vienna (1993) 469.

[194] Erckmann, V., et al., Phys. Rev. Lett. **70** (1993) 2086.

[195] Wagner, F., et al., Plasma Phys. Control. Fusion **36** (1994) A61.

[196] Toi, K, et al., in Plasma Physics and Controlled Nuclear Fusion Research 1992 (Proc. 14th Int. Conf. Würzburg, 1992), Vol. 2, IAEA, Vienna (1993) 461.

[197] Toi, K., et al., Plasma Phys. Control. Fusion **36** (1994) A117.

[198] Sakai, O., Yasaka, Y., Itatani, R., Phys. Rev. Lett. **26** (1993) 4071.

[199] Lohr, J., et al., Phys. Rev. Lett. **60** (1988) 2630.

[200] Hoshino, K., et al., Phys. Rev. Lett. **63** (1989) 770.

[201] Steinmetz, K., et al., Phys. Rev. Lett. **58** (1987) 124.

[202] Tsuji, S., et al., Phys. Rev. Lett. **64** (1990) 1023.

[203] Osborne, T.H., et al., Nucl. Fusion **30** (1990) 2023.

[204] Ashkinazi, L.G., Golant, V.E., Lebedev, S.V., Rozhanski, V.A., Tendler, M., Nucl. Fusion **32** (1992) 271.

[205] Kaufmann, M., et al., Plasma Phys. Control. Fusion **35** (1993) B205.

[206] Carolan, P.G., et al., Plasma Phys. Control. Fusion **36** (1994) A111.

[207] Taylor, R.J., et al., Phys. Rev. Lett. **63** (1989) 2365.

[208] Weynants, R.R., et al., in Plasma Physics and Controlled Nuclear Fusion Research 1990 (Proc. 13th Int. Conf. Washington, 1990), Vol. 1, IAEA, Vienna (1991) 473.

[209] Wagner, F., et al., Phys. Rev. Lett. **53** (1984) 1453

[210] Lehecka, T., et al., in Controlled Fusion and Plasma Physics (Proc.16th Eur. Conf. Venice, 1989), Vol. 13B, Part I, European Physical Society, Geneva (1989) 123.

[211] Holzhauer, E., Dodel, G., ASDEX Team, Rev. Sci. Instrum. **61** (1990) 2817.

[212] Manso, M.E., et al., in Controlled Fusion and Plasma Physics (Proc. 18th Eur. Conf. Berlin, 1991), Vol. 15C, Part I, European Physical Society, Geneva (1991) 393.

[213] Toi, K., Gernhardt, J., Kluber, O., Kornherr, M., Phys. Rev. Lett. **62** (1989) 430.

[214] Von Goeler, S., Kluber, O., Fussmann, G., Gernhardt, J., Kornherr, M., Nucl. Fusion **30** (1990) 395.

[215] Groebner, R.J., Burrell, K.H., Seraydarian, R.P., Phys. Rev. Lett. **64** (1990) 3015.

[216] Groebner, R.J., Burrell, K.H., Gohil, P., Seraydarian, R.P., Rev. Sci. Instrum. **61** (1990) 2920.

[217] Groebner, R.J., et al., in Plasma Physics and Controlled Nuclear Fusion Research 1990 (Proc. 13th Int. Conf. Washington, 1990), Vol. 1, IAEA, Vienna (1991) 453.

[218] Ida, K., Phys. Rev. Lett. **65** (1990) 1364.

[219] Ida, K., et al., Phys. Fluids B **4** (1992) 2552.

[220] Burrell, K.H., et al., Plasma Phys. Control. Fusion **34** (1992) 1859.

[221] Groebner, R.J., Phys. Fluids B **5** (1993) 2343.

[222] Shaing, K.C., Crume Jr, E.C., Phys. Rev. Lett. **63** (1989) 2369.

[223] Shaing, K.C., Crume Jr, E.C., Houlberg, W.A., Phys. Fluids B **2** (1990) 1492.

[224] Diamond, P.H., et al., in Plasma Physics and Controlled Nuclear Fusion Research 1992 (Proc. 14th Int. Conf. Würzburg, 1992), Vol. 2, IAEA, Vienna (1993) 97.

[225] Sidikman, K.C., Carreras, B.A., Diamond, P.H., Garcia, L., Phys. Plasmas **1** (1994) 1142.

[226] Ritz, Ch.P., Lin, H., Rhodes, T.L., Wootton, A.J., Phys. Rev. Lett. **65** (1990) 2543.

[227] Ohdachi, S., et al., Plasma Phys. Control. Fusion **36** (1994) A201.

[228] Thompson, J., J. Atmos. Sci. **27** (1970) 1107.

[229] Kuo, H.L., Phys. Fluids **6** (1963) 195.

[230] Rozhansky, V., Tendler, M., Phys. Fluids B **4** (1992) 1877.

[231] Hinton, F.L., Kim, Y.-B., Nucl. Fusion **34** (1994) 899.

[232] Yushmanov, P.N., Dong, J.Q., Horton, W., Su, X.N., Krasheninnikov, S.I., Phys. Plasmas **1** (1994) 1583.

[233] Rozhansky, V., Tendler, M., Voskoboinikov, S., Plasma Phys. Control. Fusion **38** (1996) 1327.

[234] Itoh, S.-I., Itoh, K., Nucl. Fusion **29** (1989) 1031.

[235] Tendler, M., Daybelge, U., Rozhansky, V., in Plasma Physics and Controlled Nuclear Fusion Research 1992 (Proc. 14th Int. Conf, Würzburg, 1992), Vol. 2, IAEA, Vienna (1993) 243.

[236] Shaing, K.C., Hsu, C.T., Phys. Plasmas **2** (1995) 1801.

[237] Toda, S., Itoh, S-I, Yagi, M., Miura, Y., Plasma Phys. Control. Fusion **39** (1997) 301.

[238] Hassam, A.B., Antonsen Jr, T.M., Drake, J.F., Liu, C.S., Phys. Rev. Lett. **66** (1991) 309.

[239] McCarthy, D.R., Drake, J.F., Gudzar, P.N., Hassam, A.B., Phys. Fluids B **5** (1993) 1181.

[240] Gudzar, P.N., Hassam, A.B., Phys. Plasmas **3** (1996) 3701.

[241] Hinton, F.L., Staebler, G.M., Phys. Fluids B **5** (1993) 1281.

[242] Staebler, G.M., et al., Phys. Plasmas **1** (1994) 909.

[243] Waltz, R.E., Staebler, G.M., Konings, J.A., in Fusion Energy 1996 (Proc. 16th Int. Conf. Montréal, 1996), Vol. 2, IAEA, Vienna (1997) 385.

[244] Rozhansky, V., Tendler, M., in Controlled Fusion and Plasma Physics (Proc. 21st Eur. Conf. Montpellier, 1994), Vol. 18B, Part II, European Physical Society, Geneva (1994) 302.

[245] Itoh, S.-I., et al., Plasma Phys. Control. Fusion **36** (1994) A261.

[246] Diamond, P.H., Kim, Y-B., Phys. Fluids B **3** (1991) 1626.

[247] Carreras, B.A., Newman, D., Diamond, P.H., Liang, Y.-M., Phys. Plasmas **1** (1994) 4014.

[248] Diamond, P.H., Liang, Y.-M., Carreras, B.A., Terry, P.W., Phys. Rev. Lett. **72** (1994) 2565.

[249] Sugama, H., Horton, W., Plasma Phys. Control. Fusion **37** (1995) 345.

[250] Pogutse, O., Kerner, W., Gribkov, V., Bazdenkov, S., Osipenko, M., Plasma Phys. Control. Fusion **36** (1994) 1963.

[251] Carreras, B.A., Diamond, P.H., Vetoulis, G., Phys. Plasmas **3** (1996) 4106.

[252] Osborne, T.H., et al., in Controlled Fusion and Plasma Physics (Proc. 24th Eur. Conf. Berchtesgaden, 1997), Vol. 21A, Part III, European Physical Society, Geneva (1997) 1101.

[253] Hubbard, A.E., et al., in Fusion Energy 1996 (Proc. 16th Int. Conf. Montréal, 1996), Vol. 1, IAEA, Vienna (1997) 875.

[254] H-Mode Database Working Group (presented by D.P. Schissel), in Controlled Fusion and Plasma Physics (Proc. 20th Eur. Conf. Lisbon, 1993), Vol. 17C, Part 1, European Physical Society, Geneva (1993) 103.

[255] Gohil, P., et al., Phys. Rev. Lett. **61** (1988) 1603.

[256] Hatae, T., et al., Plasma Phys. Control. Fusion **40** (1998) 1073.

[257] Gauthier, E., et al., in Controlled Fusion and Plasma Physics (Proc. 24th Eur. Conf. Berchtesgaden, 1997), Vol. 21A, Part I, European Physical Society, Geneva (1997) 61.

[258] Breger, P., et al., in Controlled Fusion and Plasma Physics (Proc. 24th Eur. Conf. Berchtesgaden, 1997), Vol. 21A, Part I, European Physical Society, Geneva (1997) 69.

[259] JET Team (presented by G.J. Cordey), Paper IAEA-F1-CN-69/EX7/1, presented at H-Mode Power Threshold and Confinement in JET H, D, DT and T Plasmas, 17th IAEA Fusion Energy Conf. Yokohama, Japan, 1998.

[260] ASDEX Team, Nucl. Fusion **29** (1989) 1959.

[261] JFT-2M Group (presented by Y. Miura), in Contributions to the 3rd Workshop on H-mode Physics (Proc. of Int. Workshop Abingdon, 1991), Vol. 1, JET Joint Undertaking (1991) 141.

[262] Nardone, C., et al., in Controlled Fusion and Plasma Physics (Proc. 18th Eur. Conf. Berlin, 1991), Vol. 15C, Part I, European Physical Society, Geneva (1991) 377.

[263] Mori, M., JT-60 Team and JFT-2M Team, Plasma Phys. Control. Fusion **36** (1994) A39.

[264] Fielding, et al., Plasma Phys. Control. Fusion **38** (1996) 1091.

[265] Cordey, J.G., et al., Plasma Phys. Control. Fusion **38** (1996) 1237.

[266] Snipes, J.A., et al., Plasma Phys. Control. Fusion **38** (1996) 1127.

[267] Weisen, H., et al., Plasma Phys. Control. Fusion **38** (1996) 1137.

[268] Carlstrom, T., Groebner, R., Phys. Plasmas **3** (1996) 1867.

[269] Ryter, F., H Mode Database Working Group, Nucl. Fusion **36** (1996) 1217.

[270] ITER H-Mode Threshold Database Working Group (presented by F. Ryter), Plasma Phys. Control. Fusion **38** (1996) 1279.

[271] ITER Confinement Database and Modelling Expert Group (presented by T. Takizuka), in Fusion Energy 1996 (Proc. 16th Int. Conf. Montréal, 1996), Vol. 2, IAEA, Vienna (1997) 795.

[272] ITER H-Mode Threshold Database Working Group (presented by J.A. Snipes), in Controlled Fusion and Plasma Physics (Proc. 24th Eur Conf. Berchtesgaden, 1997), Vol. 21A, Part III, European Physical Society, Geneva (1997) 961.

[273] ITER H-Mode Threshold Database Working Group (presented by E. Righi), Plasma Phys. Control. Fusion **40** (1998) 857.

[274] Mertens, V., et al., in Fusion Energy 1996 (Proc. 16th Int. Conf. Montréal, 1996), Vol. 1, IAEA, Vienna (1997) 413.

[275] Righi, E., et al., Plasma Phys. Control. Fusion **40** (1998) 721.

[276] JET Team (presented by J.G. Cordey), in Fusion Energy 1996 (Proc. 16th Int. Conf. Montréal, 1996), Vol. 1, IAEA, Vienna (1997) 603.

[277] Zohm, H., et al., in Fusion Energy 1996 (Proc. 16th Int. Conf. Montréal, 1996), Vol. 1, IAEA, Vienna (1997) 439.

[278] Chang, Z., Callen, J.D., Nucl. Fusion **30** (1990) 219.

[279] Chang, Z., et al., Nucl. Fusion **34** (1994) 1309.

[280] Campbell, D.J., et al., Nucl. Fusion **26** (1986) 1085.

[281] Schissel, D.F., et al., Nucl. Fusion **32** (1992) 107.

[282] Lazzaro, E., et al., Nucl. Fusion **30** (1990) 2157.

[283] Kamada, Y., et al., in Plasma Physics and Controlled Nuclear Fusion Research 1992 (Proc. 14th Int. Conf. Würzburg, 1992), Vol. 1, IAEA, Vienna (1993) 507.

[284] Kamada, Y., Takizuka, T., Kikuchi, M., Ninomiya, H., Nucl. Fusion **33** (1993) 225.

[285] Kim, S.K., et al., in Plasma Physics and Controlled Nuclear Fusion Research (Proc. 12th Int. Conf. Nice, 1988), Vol. 1, IAEA, Vienna (1989) 281.

[286] Ödblom, A., Anderson, D., Eriksson, L.-G., Lisak, M., Phys. Plasmas **3** (1996) 956.

[287] Dux, R., et al., in Plasma Physics and Controlled Fusion (Proc. 23rd Eur. Conf. Kiev, 1996), Vol. 20C, Part I, European Physical Society, Geneva (1996) 95.

[288] Soltwisch, H., Stodieck, W., Manickam, J., Schlüter, J., in Plasma Physics and Controlled Nuclear Fusion Research 1986 (Proc. 11th Int. Conf. Kyoto, 1986), Vol. 1, IAEA, Vienna (1987) 263.

[289] Kadomtsev, B.B., Sov. J. Plasma Phys. **1** (1975) 389 (Fiz. Plazmy **1** (1975) 710).

[290] Porcelli, F., Boucher, D., Rosenbluth, M.N., Plasma Phys. Control. Fusion **38** (1996) 2163.

[291] Kolesnichenko, Ya.I., Lutsenko, V.V., Yakovenko, Yu.V., Nucl. Fusion **34** (1994) 1619.

[292] Jarvis, O.N., et al., in Controlled Fusion and Plasma Physics (Proc. 22nd Eur. Conf. Bournemouth, 1995), Vol. 19C, Part III, European Physical Society, Geneva (1995) 57.

[293] Zweben, S.J., et al., Plasma Phys. Control. Fusion **39** (1997) A275.

[294] Campbell, D.J., et al., Phys. Rev. Lett. **60** (1988) 2148.

[295] JET Team (presented by D.J. Campbell), in Plasma Physics and Controlled Nuclear Fusion Research 1990 (Proc. 13th Int. Conf. Washington DC, 1990), Vol. 1, IAEA, Vienna (1991) 437.

[296] Phillips, C.K., et al., Phys. Fluids B **4** (1992) 2155.

[297] McClements, K.G., Dendy, R.O., Hastie, R.J., Martin, T.J., Phys. Plasmas **3** (1996) 2994.

[298] Zohm, H., Plasma Phys. Control. Fusion **38** (1996) 105.

[299] Connor, J.W., Plasma Phys. Control. Fusion **40** (1998) 531.

[300] Colton, A., Porte, I., in Controlled Fusion and Plasma Physics (Proc. 20th Eur. Conf. Lisbon, 1992), Vol. 17C, Part I, European Physical Society, Geneva (1993) 11.

[301] Suttrop, W., Büchl, K., de Blank, H.J., Schwinger, J., Zohm, H., Plasma Phys. Control. Fusion **38** (1996) 1407.

[302] Hill, D.N., et al., J. Nucl. Mater. **196**–**198** (1992) 204.

[303] Suttrop, W., et al., Plasma Phys. Control. Fusion **40** (1998) 771.

[304] Schissel, D.P., Osborne, T.H., Carlstrom, T.N., Zohm, H., in Controlled Fusion and Plasma Physics (Proc. 19th Eur. Conf. Innsbruck, 1992), Vol. 16C, Part I, European Physical Society, Geneva (1992) 235.

[305] H-Mode Database Working Group (presented by O. Kardaun), in Plasma Physics and Controlled Nuclear Fusion Research 1992 (Proc. 14th Int. Conf. Würzburg, 1992), Vol. III, IAEA, Vienna (1993) 251.

[306] KAMADA. Y., et al., Plasma Phys. Control. Fusion **36** (1994) A123.

[307] Zohm, H., et al., in Tokamak Concept Improvement (Proc. of Int. Workshop, Varenna, 1994) (ed. S. Bernabei, N. Sauthoff, F. Sindoni), Editrice Compositori, Bologna (1994) 149.

[308] Zohm, H., Plasma Phys. Control. Fusion **38** (1996) 1213.

[309] Buttery, R.J., et al., in Controlled Fusion and Plasma Physics (Proc. 22nd Eur. Conf.

Bournemouth, 1995), Vol. 19C, Part III, European Physical Society, Geneva (1995) 273.

[310] Fielding, S.J., et al., J. Nucl. Mater. **241**–**243** (1997) 902.

[311] Lackner, K., et al., Plasma Phys. Control. Fusion **36** (1994) B79.

[312] Christiansen, J.P., et al., Nucl. Fusion **32** (1992) 291.

[313] ITER H Mode Database Working Group, Nucl. Fusion **34** (1994) 131.

[314] Miura, Y., et al., Nucl. Fusion **32** (1992) 1473.

[315] ITER Confinement Database And Modeling Working Group (presented by J.G. Cordey), Plasma Phys. Control. Fusion **39** (1997) B115.

[316] Christiansen, J.P., Cordey, J.G., Kardaun, O.J.W.F., Thomsen, K., Nucl. Fusion **31** (1991) 2117.

[317] Mahdavi, M.A., et al., in Fusion Energy 1996 (Proc. 16th Int. Conf. Montréal, 1996), Vol. 1, IAEA, Vienna (1997) 397.

[318] Blackwell, D., Girshik, M.A., Theory of Games and Statistical Decisions, Dover Publications, New York (1979).

[319] McCarthy, P.J., Morabito, F.C., in Diagnostics for Experimental Thermonuclear Fusion Reactors 2 (Proc. Int. Workshop Varenna, 1997) (ed. P.E. Stott, G. Gorini, P. Prandoni, E. Sindoni), Plenum Press, New York (1998) 541–544.

[320] Kardaun, O., Plasma Phys. Control. Fusion **41** (1999) 429.

[321] Kardaun, O., Kus, A., Basic Probability and Statistics for Experimental Plasma Physics, Rep. IPP 5/68, Max-Planck-Institut für Plasmaphysik (September 1996).

[322] Hammett, G., Dorland, W., Kotschenreuther, M., 'On cross-validation for confinement prediction' (in preparation).

[323] Technical Basis for the ITER Final Design Report, Cost Review and Safety Analysis (FDR), ITER EDA Documentation Series No. 16, IAEA, Vienna (1998).

[324] Kardaun, O., Thomsen, K., Cordey, J., Wagner, F., in Controlled Fusion and Plasma Heating (Proc. 17th Eur. Conf. Amsterdam, 1990), Vol. 14B, Part I, European Physical Society, Geneva (1990) 110.

[325] Kotschenreuther, M., et al., The Effect of Sheared Rotation on Confinement, Rep. ITER/US/97/PH-01-3, US ITER Home Team (1997).

[326] Connor, J.W., Taylor, J.B., Phys. Fluids **27** (1984) 2676.

[327] Hagan, W.K., Frieman, E.A., Phys. Fluids **29** (1986) 3635.

[328] Frieman, E. A., Chen Liu, Phys. Fluids **25** (1982) 502.

[329] Waltz, R. E., DeBoo, J. C., Rosenbluth, M. N., Phys. Rev. Lett. **65** (1990) 2390.

[330] Luce, T.C., Petty, C.C., Balet, B., Cordey, J.G., in Fusion Energy 1996 (Proc. 16th Int. Conf. Montréal, 1996), Vol. 1, IAEA, Vienna (1997) 611.

[331] Schachter, J., Local Transport Analysis for the Alcator C-Mod Tokamak, Rep. PSFC/RR-97-12, Plasma Fusion Center, Massachusetts Institute of Technology (1997).

[332] Petty, C.C., Luce, T.C., in Controlled Fusion and Plasma Physics (Proc. 24th Eur. Conf. Berchtesgaden, 1997), Vol. 21A, Part III, European Physical Society, Geneva (1997) 1085.

[333] Shirai, H., Takizuka, T., Kamada, Y., Fukuda, T., Koide, Y., Nondimensional transport study on ELMy H-mode plasmas in JT-60U, in Review of JT-60U Experimental Results from February to November 1996, Rep. JAERI-Research 97-047, Japan Atomic Energy Institute (1997).

[334] Christiansen, J.P., et al., in Controlled Fusion and Plasma Physics (Proc. 24th Eur. Conf. Berchtesgaden, 1997), Vol. 21A, Part I, European Physical Society, Geneva (1997) 89.

[335] Greenwald, M., et al., Plasma Phys. Control. Fusion **40** (1998) 789.

[336] Luce, T.C., Petty, C.C., in Controlled Fusion and Plasma Physics (Proc. 22th Eur. Conf. Bournemouth, 1995), Vol. 19C, Part III, European Physical Society, Geneva (1995) 25.

[337] Meade, D.M., et al., in Plasma Physics and Controlled Nuclear Fusion Research 1990 (Proc. 13th Int. Conf. Washington, 1990), Vol. 1, IAEA, Vienna (1991) 9.

[338] Levinton, F.M., et al., in Fusion Energy 1996 (Proc. 16th Int. Conf. Montréal, 1996), Vol. 1, IAEA, Vienna (1997) 211.

[339] Connor, J.W., et al., in Fusion Energy 1996 (Proc. 16th Int. Conf. Montréal, 1996), Vol. 2, IAEA, Vienna (1997) 935.

[340] Hirshman, S.P., Sigmar, D.J., Clarke, J.F., Phys. Fluids **19** (1976) 656.

[341] Chang, C.S., Hinton, F.L., Phys. Fluids **29** (1986) 3314.

[342] Connor, J.W., et al., Plasma Phys. Control. Fusion **35** (1993) 319.

[343] Tibone, F., Connor, J.W., Stringer, T.E., Wilson, H.R., Plasma Phys. Control. Fusion **36** (1994) 473.

[344] Weiland, J., Jarman, A., Nordman, H., Nucl. Fusion **29** (1989) 1810.

[345] Nordman, H., Weiland, J., Jarmen, A., Nucl. Fusion **30** (1990) 983.

[346] Weiland, J., Nordman, H., Nucl. Fusion **31** (1991) 390.

[347] Nordman, H., Weiland, J., Nucl. Fusion **32** (1992) 1653.

[348] Nordman, H., Strand, P., Weiland, J,, Christiansen, J.P., Nucl. Fusion **37** (1997) 413.

[349] Kinsey, J., Singer, C., Djemil, T., Cox, D., Bateman, G., Phys. Plasmas **2** (1995) 811.

[350] Kinsey, J., Bateman, G., Kritz, A., Redd, A., Phys. Plasmas **3** (1996) 561.

[351] Kinsey, J., Bateman, G., Phys. Plasmas **3** (1996) 3344.

[352] Bateman, G., Kinsey, J., Kritz, A.H., Redd, A., Weiland, J., in Fusion Energy 1996 (Proc. 16th Int. Conf. Montréal, 1996), Vol. 2, IAEA, Vienna (1997) 559.

[353] Kritz, A.H., Kinsey, J.E., Bateman, G., Weiland, J., Redd, A.J., in Controlled Fusion and Plasma Physics (Proc. 23rd Eur. Conf. Kiev, 1996), Vol. 20C, Part I, European Physical Society, Geneva (1996) 311.

[354] Waltz, R.E., Staebler, G.M., Hammett, G.W., Konings, J.A., in Fusion Energy 1996 (Proc. 16th Int. Conf. Montréal, 1996), Vol. 2, IAEA, Vienna (1997) 385.

[355] Waltz, R.E., Staebler, G.M., Dorland, W., Hammett, G.W., Kotschenreuther, M., Konings, J.A., Phys. Plasmas **4** (1997) 2482.

[356] Dorland, W., Progress Report from the Cyclone Project, presented at the Combined Workshop of the Confinement and Transport and Confinement Modelling and Database Expert Group, Garching, Germany (29 September 1997).

[357] Beer, M.A., Hammett, G.W., in Theory of Fusion Plasmas (Proc. Joint Varenna–Lausanne Int. Workshop, Varenna, 1998) (ed. J.W. Connor, E. Sindoni, J. Vaclavik), Editrice Compositori, Bologna (1999) 19.

[358] Dimits, A.M., Cohen, B.I., Mattor, N., Nevins, W.M., Shumaker, D.E., Paper IAEA-F1-CN-69/TH1/1 presented at Fusion Energy 1998 (Proc. 17th Int. Conf. Yokohama, 1998), IAEA, Vienna.

[359] Lin, Z., et al., Paper IAEA-F1-CN-69/THP2/28 presented at Fusion Energy 1998 (Proc. 17th Int. Conf. Yokohama, 1998), IAEA, Vienna.

[360] Itoh, K., Itoh, S.-I., Fukuyama, A., Yagi, M., Azumi, M., Plasma Phys. Control. Fusion **36** (1994) 279.

[361] Yagi, M., Itoh, S.-I., Itoh, K., Fukuyama, A., Azumi, M., Phys. Plasmas **2** (1995) 4140.

[362] Itoh, S.-I., Itoh, K., Fukuyama, A., Yagi, M., Phys. Rev. Lett. **72** (1994) 1200.

[363] Fukuyama, A., Itoh, K., Itoh, S.-I., Yagi, M., Azumi, M., Plasma Phys. Control. Fusion **36** (1994) 1385.

[364] Fukuyama, A., Itoh, K., Itoh, S.-I., Yagi, M., Azumi, M., Plasma Phys. Control. Fusion **37** (1995) 611.

[365] Boucher, D., Rebut, P.-H., in Proceedings of IAEA Technical Committee Meeting on Advances in Simulations of Modelling of Thermonuclear Plasmas 1992, IAEA, Vienna (1993) 142.

[366] Connor, J.W., Cox, M., Fitzpatrick, R., Hastie, R.J., Hender, T.C., Hugill, J., Maddison, G.P., Robinson, D.C., Todd, T.N., Turner, M.F., IGNITOR Modelling by the Culham Group, Rep. AEA FUS 57, AEA Technology (1990).

[367] Cherubini, A., Erba, M., Parail, V., Springmann, E., Taroni, A., Plasma Phys. Control. Fusion **38** (1996) 1421.

[368] Zanca, P., Frigione, D., Marinucci, M., Zanza, V., Romanelli, F., in Theory of Fusion Plasmas (Proc. Joint Varenna–Lausanne Int. Workshop Varenna, 1996) (ed. J.W. Connor, E. Sindoni, J. Vaclavik), Editrice Compositori, Bologna (1997) 399.

[369] Vlad, G., et al., Nucl. Fusion **38** (1998) 557.

[370] Gott, Yu.V., Yurchenko, E.I., Plasma Phys. Rep. **22** (1996) 13.

[371] Dnestrovskij, Yu.N., Lysenko, S.E., Tarasyan, K.N., Nucl. Fusion **35** (1995) 1047.

[372] Isichenko, M.B., Gruzinov, A.B., Diamond, P.H., Phys. Rev. Lett. **74** (1995) 4436.

[373] Rosenbluth, M.N., Baker, D., Tokamak Density Profiles with Low Frequency Turbulence, Material presented at the Combined Workshop of the Confinement and Transport and Confinement Modelling and Database Expert Group, San Diego, USA (1997), Vol. 1.

[374] Roach, C.M., Gimblett, C.G., Hastie, R.J., in Theory of Fusion Plasma (Proc. Joint Varenna–Lausanne Int. Workshop, Varenna, 1996) (ed. J.W. Connor, E. Sindoni, J. Vaclavik), Editrice Compositori, Bologna (1997) 393.

[375] Kolesnichenko, Y.I., Lutsenko, V.V., Yakovlenko, Y.V., Fusion Technol. **25** (1993) 302.

[376] Mikkelsen, D., et al., Paper IAEA-CN-69-ITERP1/08 presented at Fusion Energy 1998 (Proc. 17th Int. Conf. Yokohama, 1998).

[377] Reiter, D., Wolf, G.H., Kever, H., Nucl. Fusion **30** (1990) 2141.

[378] Reiter, D., Wolf, G.H., Kever, H., J. Nucl. Mater. **176**–**177** (1990) 756.

[379] Hillis, D.L., et al., Phys. Rev. Lett. **65** (1990) 2382.

[380] Synakowski, E.J., et al., Phys. Rev. Lett. **65** (1990) 2255.

[381] Nakamura, H., et al., Phys. Rev. Lett. **67** (1991) 2658.

[382] Synakowski, E.J., et al., Phys. Fluids B **5** (1993) 2215.

[383] Synakowski, E.J., et al., Phys. Rev. Lett. **75** (1995) 3689.

[384] Hulse, R.A., Nucl. Technol. Fusion **3** (1983) 259.

[385] Sakasai, A., et al., in Plasma Physics and Controlled Nuclear Fusion Research 1994 (Proc. 15th Int. Conf. Seville, 1994), Vol. 2, IAEA, Vienna (1994) 95.

[386] Hillis, D.L., et al., J. Nucl. Mater. **196**–**198** (1992) 35.

[387] Bosch, H.-S., et al., J. Nucl. Mater. **241**–**243** (1997) 82.

[388] Cohen, S.A., Cecchi, J.L., Marmar, E.S., Phys. Rev. Lett. **35** (1975) 1507.

[389] Marmar, E.S., Rice, J.E., Terry, J.L., Seguin, F.H., Nucl. Fusion **22** (1982) 1567.

[390] Mattioli, M., et al., Nucl. Fusion **35** (1995) 1115.

[391] Bagdasarov, A.A., et al., in Plasma Physics and Controlled Nuclear Fusion Research 1984 (Proc. 10th Int. Conf. London, 1984), Vol. 1, IAEA, Vienna (1984) 181.

[392] Efthimion, P.C., et al., in Plasma Physics and Controlled Nuclear Fusion Research 1988 (Proc. 12th Int. Conf. Nice, 1988), Vol. 1, IAEA, Vienna (1989) 307.

[393] Gentle, K.W., Richards, B., Waelbroeck, F., Plasma Phys. Control. Fusion **29** (1987) 1077.

[394] Marinak, M.M., Nucl. Fusion **35** (1995) 399.

[395] Gentle, K.W., Gehre, O., Krieger, K., Nucl. Fusion **32** (1992) 217.

[396] Richards, B., Austin, M.E., Bravenec, R.V., Nucl. Fusion **32** (1992) 567.

[397] Moret, J.-M., Equipe TORE-SUPRA, Nucl. Fusion **32** (1992) 1241.

[398] Gentle, K.W., Phys. Fluids **31** (1988) 1105.

[399] De Haas, J.C.M., O'Rourke, J., Sips, A.C.C., Cardozo, N.J.L., Nucl. Fusion **31** (1991) 1261.

[400] Efthimion, P.C., et al., in Plasma Physics and Controlled Nuclear Fusion Research 1994 (Proc. 15th Int. Conf. Seville, 1994), Vol. 1, IAEA, Vienna (1995) 289.

[401] Efthimion, P.C., et al., Phys. Rev. Lett. **66** (1991) 421.

[402] Houlberg, W.A., Attenberger, S.E., Fusion Technol. **26** (1994) 316.

[403] Greenwald, M., et al., Phys. Plasmas **2** (1995) 2308.

[404] Giannella, R., et al., Nucl. Fusion **34** (1994) 1185.

[405] Rice, J.E., et al., Phys. Plasmas **4** (1997) 1605.

[406] Petrasso, R.D., et al., Phys. Rev. Lett. **57** (1986) 707.

[407] Connor, J.W., Cowley, S.C., Hastie, R.J., Pan, L.R., Plasma Phys. Control. Fusion **29** (1987) 919.

[408] Kim, Y.B., Diamond, P.H., Groebner, R.J., Phys. Fluids B **3** (1991) 2050.

[409] Suckewer, S., et al., Nucl. Fusion **21** (1981) 1301.

[410] Isler, R.C., et al., Nucl. Fusion **26** (1986) 391.

[411] Burrell, K.H., Groebner, R.J., John, H.St., Seraydarian, R.P., Nucl. Fusion **28** (1988) 3.

[412] Scott, S.D., et al., Phys. Rev. Lett. **64** (1990) 531.

[413] Kallenbach, A., et al., Plasma Phys. Control. Fusion **33** (1991) 595.

[414] Asakura, N., et al., Nucl. Fusion **33** (1993) 1165.

[415] Zastrow, K.-D., DeHaas, J.C.M., Von Hellermann, M., Howman, A.C., König, R.W.T., in Controlled Fusion and Plasma Physics (Proc. 22nd Eur. Conf. Bournemouth, 1995), Vol. 19C, Part II, European Physical Society, Geneva (1995) 453.

[416] Zastrow, K.-D., et al., Nucl. Fusion **38** (1998) 257.

[417] Kallenbach, A., et al., Nucl. Fusion **30** (1990) 645.

[418] Weisen, H., et al., Nucl. Fusion **29** (1989) 2187.

[419] Snipes, J.A., Campbell, D.J., Hender, T.C., Von Hellermann, M., Weisen, H., Nucl. Fusion **30** (1990) 205.

[420] Zohm, H., Kallenbach, A., Bruhns, H., Fussmann, G., KlÜber, O., Europhys. Lett. **11** (1990) 745.

[421] Nave, M.F.F., Wesson, J.A., Nucl. Fusion **30** (1990) 2575.

[422] Fitzpatrik, R., Hender, T.C., Phys. Fluids B **3** (1991) 644.

[423] Kim, J., et al., Phys. Rev. Lett. **72** (1994) 2199.

[424] Rice, J.E., et al., Nucl. Fusion **38** (1998) 75.

[425] Eriksson, L.-G., Righi, E., Zastrow, K.-D., Plasma Phys. Control. Fusion **39** (1997) 27.

[426] Burrell, K.H., et al., in Controlled Fusion and Plasma Heating (Proc. 17th Eur. Conf. Amsterdam, 1990), Vol. 14B, Part I, European Physical Society, Geneva (1990) 271.

[427] Scott, S.D., et al., Phys. Fluids B **2** (1990) 1300.

[428] De Esch, H.P.L., Strok, D., Weisen, H., in Controlled Fusion and Plasma Heating (Proc. 17th Eur. Conf. Amsterdam, 1990), Vol. 14B, Part I, European Physical Society, Geneva (1990) 90.

[429] Nagashima, K., Koide, Y., Shirai, H., Nucl. Fusion **34** (1994) 449.

[430] Rosenbluth, M.N., Rutherford, P.H., Taylor, J.B., Frieman, E.A., Kovrizhnykh, L.M., in Plasma Physics and Controlled Nuclear Fusion 1970 (Proc. 4th Int. Conf. Madison, 1970), Vol. 1, IAEA, Vienna (1971) 495.

[431] Hinton, F.L., Wong, S.K., Phys. Fluids **28** (1985) 3082.

[432] Mattor, N., Diamond, P.H., Phys. Fluids **31** (1988) 1180.

[433] Morozov, D.Kh., Pogutse, O.P., in Plasma Physics and Controlled Nuclear Fusion Research 1986 (Proc. 11th Int. Conf. Kyoto, 1986), Vol. 3, IAEA, Vienna (1987) 435.

[434] De Esch, H.P.L., Routes to Ignition on ITER by Means of Neutral Beams, Rep. JET-R(97)16, JET Joint Undertaking (December 1997).

[435] Hazeltine, R.D., Meiss, J.D., Plasma Confinement, Addison-Wesley Publishing Company, Redwood City (1992) 365.

[436] Rebut, P.H., Lallia, P.P., Watkins, M.L., in Plasma Physics and Controlled Nuclear Fusion Research 1988 (Proc. 12th Int. Conf. Nice, 1988), Vol. 2, IAEA, Vienna (1989) 191.

[437] Odajima, K., Shimomura, Y., Energy Confinement Scaling Based on Offset Linear Characteristics, Rep. JAERI-M 88-068, Japan Atomic Energy

Research Institute (1988).

[438] H-Mode Database Working Group (presented by O. Kardaun), in Controlled Fusion and Plasma Physics (Proc. 21st Eur. Conf. Montpellier, 1994), Vol. 18B, Part I, European Physical Society, Geneva (1994) 90.

[439] Takizuka, T., Plasma Phys. Control. Fusion **40** (1998) 852.

[440] Kardaun, O., Itoh, S.-I., Itoh, K., Kardaun, J., Discriminant Analysis to Predict the Occurrence of ELMs, Rep. NIFS 242, Japan National Institute for Fusion Studies (1993).

[441] Kardaun, O., Kus, A., H-Mode Database Working Group, Global Energy Confinement Analysis, Internet Rep. IPP-IR 96/5 2.1, Max-Planck-Institute für Plasmaphysik (1996). Webpage `http://www.ipp.mpg.de/ipp/netreports`.

[442] SAS Institute Inc., SAS/STAT User's Guide, Version 6, 4th edn, Vol. I, II, Cary (1989).

[443] Statistical Sciences, S-PLUS Guide to Statistical and Mathematical Analysis, Version 3.2, MathSoft Inc. (1993).

[444] Shannon, C.E., The Bell System Technical Journal **27** (1948) 379, 623.

[445] Kinchin, A.I., The Mathematical Foundations of Information Theory, Dover Publications, New York (1957).

[446] Tukey, J.W., Ann. Math. Stat. **29** (1958) 614.

[447] Efron, B., Ann. Statist. **7** (1979) 1–26. Reprinted in Breakthroughs in Statistics (ed. S. Kotz, N.L. Johnson), Vol. II, Springer-Verlag, New York (1992) 569–593.